Coupled micro electrochemistry and optics for imagery and study of chemical surface reactions

Sorin Munteanu

THESE DE DOCTORAT DE
L'UNIVERSITE PIERRE ET MARIE CURIE

Spécialité

Electrochimie

(Chimie Physique et Chimie Analytique de Paris Centre, ED 388)

Présentée par

Sorin Munteanu

Pour obtenir le grade de

DOCTEUR de l'UNIVERSITÉ PIERRE ET MARIE CURIE

Sujet de la thèse :

Micro électrochimie et optique couplées pour l'imagerie et l'étude de réactions chimiques de surface

Soutenue le 15 octobre 2012

devant le jury composé de :

Mme. Jeanine TORTAJADA	Directeur de recherche CNRS	Rapporteur
M. Neso SOJIC	Professeur Université Bordeaux 1	Rapporteur
M. Emmanuel MAISONHAUTE	Professeur UPMC	Examinateur
Mme Nicole JAFFREZIC	Directeur de recherche CNRS	Examinateur
M. Jean-Paul Roger	Maitre de conférences ESPCI	Invité
Mme. Catherine COMBELLAS	Directeur de recherche CNRS	Directeur de thèse
M. Frédéric KANOUFI	Directeur de recherche CNRS	Codirecteur de thèse

THESE DE DOCTORAT DE
L'UNIVERSITE PIERRE ET MARIE CURIE

Spécialité

Electrochimie

(Chimie Physique et Chimie Analytique de Paris Centre, ED 388)

Présentée par

Sorin Munteanu

Pour obtenir le grade de

DOCTEUR de l'UNIVERSITÉ PIERRE ET MARIE CURIE

Sujet de la thèse :

Micro électrochimie et optique couplées pour l'imagerie et l'étude de réactions chimiques de surface

Soutenue le 15 octobre 2012

devant le jury composé de :

Mme. Jeanine TORTAJADA	Directeur de recherche CNRS	Rapporteur
M. Neso SOJIC	Professeur Université Bordeaux 1	Rapporteur
M. Emmanuel MAISONHAUTE	Professeur UPMC	Examinateur
Mme Nicole JAFFREZIC	Directeur de recherche CNRS	Examinateur
M. Jean-Paul Roger	Maitre de conférences ESPCI	Invité
Mme. Catherine COMBELLAS	Directeur de recherche CNRS	Directeur de thèse
M. Frederic KANOUFI	Directeur de recherche CNRS	Codirecteur de thèse

Table of contents

Introduction

The objective was to develop methods to monitor and quantify the chemical reactivity of surfaces at the micrometric scale.

Indeed, the description of the phenomena appearing on a surface as a result of its local or total modification during chemical reactions is of main interest. Fast and selective detection of molecular interactions at an interface is an important issue for many areas. One of the largest applications refers to the detection of specific interactions in analytical biosensors. The principle is to monitor the interaction between a target analyte and a complementary receptor immobilized on a substrate. This specific interaction generates the modification of one or several physico-chemical properties which are received directly by the transducer via (electronic) signal generally proportional in intensity or frequency with the concentration of the analyte. The optimization of the sensor response depends on various factors such as the surface architecture, chemical functionalization of the surface, as well as the selected detection mode for the transducer. The reliability of the sensor response requires a highly specific and selective recognition, which can be obtained by the choice of target receptor pairs, and / or by the use of a coupled detection mode allowing for information redundancy.

Electrochemistry is a relevant technique for addressing the reactivity of various conducting, semiconducting or insulating surfaces and interfaces. In fact, by applying an electric potential to an electrode or to an interface, a redox species can be generated, which will subsequently activate electrochemically the interface. Simultaneously, the current flowing through the electrode or interface can be measured, accessing in this way information related to its reactivity. This technique has been widely used to characterize the electrochemical or redox reactivity of various interfaces. An electrode may also function as a source of a chemical reagent, and electrochemistry allows also activating and / or characterizing the chemical reactivity of various interfaces.

Electrochemical techniques are well suited for the study of large surfaces, but when going to micrometer scale, or when apprehending the local reactivity of an interface,

it is necessary to use local electrochemical probes. This has been possible thanks to the development of microelectrodes and particularly to the evolution of electrochemical microscopy (SECM for Scanning Electro Chemical Microscopy). This technique allows determining the reactivity of an interface, or modifying it, at the micrometer scale, by scanning a local probe, a microelectrode, above the surface of interest. Although SECM is the only technique that allows measuring locally the surface chemical reactivity, its main limitations are related to the size of the local probe. The reaching of sub micrometer size is not yet an easy task. Furthermore, as in the case of any local probe technique, the mapping of surface reactivity requires a long duration due to the lateral displacement of the probe.

In parallel with the scanning probe techniques, complementary approaches using a full-field instantaneous measurement have been developed to examine the reactivity of surfaces. A snapshot of a surface during the chemical transformation can be obtained by an optical technique. Many optical microscopy techniques are used to image and characterize surface changes under a chemical modification. They describe different optical properties (interference, absorption, reflection, fluorescence, surface plasmon ...) across the full spectrum of radiation (X, UV, visible, infrared ...). New optical imaging techniques were developed owing to the advancement of CCD or CMOS cameras, that are used to map the analyzed surfaces and obtain in this way information on their reactivity.

It is in this context that this PhD was carried out. It consisted of addressing different issues as: chemical structuration and reactivity of surface, reactivity imagery, coupling detection modes and analytical platforms. Our goal was to build simple and effective experimental devices capable of imaging and studying *in situ* and in real time the chemical transformation of surfaces. These devices should be particularly applied to analytical platforms such as micromechanical cantilevers. The principle of our approach is based on the coupling between imaging techniques, optical microscopies, and micro-electrochemical techniques to study and map in real time and *in situ* interfacial (electro-) chemical processes. This approach should be promising to provide mechanistic insights on electrochemical processes and also for the development of important analytical concepts in the field of sensors.

In a first chapter, I will discuss the benefits of combining an optical detection mode with the electrochemical actuation or transformation of a surface. I will present a bibliographic review of some optical methods used for sensing and detection, with their advantages and limitations. A particular interest will be shown for SPR (surface plasmon resonance) derived technique, which is currently the most sensitive optical technique for surface chemical transformation follow-up.

Our goal was then to develop simple and efficient opto-electrochemical setups able to compete with SPR-electrochemical systems. The research on this topic was only recently started in the group when I arrived. We proposed, in collaboration with two researchers, Jean-Paul Roger and Gilles Tessier, from 'Institut Langevin' at ESPCI ParisTech, to use the simplest but robust optical imagery techniques to obtain an electro-optical microscope. First, we have focused on the measurement of the local change in refractive index associated to molecular interactions with a reflecting surface. The simplest technique able to detect such change consists of measuring the intensity change of light reflected by the reflecting surface when it is submitted to such chemical stimulus. The second chapter will then be related to the introduction of light reflectivity microscopy for the study of surface chemical reactivity. I will focus on the optical property chosen for our experiments with the fundamental theoretical aspects of the measurement, which emerges from the Snell's law, and also on the choice of the best suited material as the substrate to be analyzed. The potentiality of the technique will be illustrated in the description of a model system – the electrografting of diazonium salts. The validation of the setup will be followed by the study of the electrografting of diazonium salts on surfaces of various dimensions and natures. We will detail and analyze the kinetic information that can be gathered during the growth of an organic layer on a gold (Au) electrode surface. The application of such electro-optical microscope will be extended to the monitoring of a biological reaction by developing different formats of immunoassays on Au surface.

In the third chapter, we will detail the imaging capabilities of the proposed light reflectivity microscope. We will use our electro-optical microscope to describe the local chemical and electrochemical reactivity of different substrates. It will start with the detection and characterization, in air, of different chemical structurations of surfaces patterned by μCP(micro contact printing) or UV photolithography. It will

continue with the study of the local (electro-)chemical reactivity at microelectrodes and then at patterned substrates. This study reveals the possibility to spatially resolve the flux of generated radicals. Then, this strategy will be used to engage such flux of reactive species with different chemical species (molecules, biomolecules) locally imprinted on a substrate. This allows inspecting indirectly the chemical reactivity of immobilized species towards electrogenerated radicals. It will be extended to biochemical probes and we particularly inspected how biochemical molecules irradiated with electrogenerated radicals retain their biochemical activity.

In the fourth chapter, a new optical setup will be presented that consists of a home-made ellipsometric microscope. The coupling of the very sensitive imaging ellipsometric microscopy with electrochemistry, allows for the first time observing an *in situ* and real time surface modification. The capability of this new approach will be illustrated for the characterization in air of *ex situ* modified surfaces, along with the *in situ* observation of the electrografting of a diazonium salt on a large gold substrate. The real-time study of the local reactivity will also be performed on micropatterned surfaces obtained through photolithographic techniques.

Our objective when building such experimental setup is to propose a new detection platform for microcantilever-based sensors. Even though we have validated the principle of imaging processes occurring at microcantilevers under electrochemical activation, we could not use it in a relevant sensing application. However, the fifth chapter will explore an alternative mode of detection in microcantilever platforms. It will present the recently published results on the use of the SECM as a monitoring tool in microcantilever platforms. The aim of this work is to propose an alternative to the classical optical mode of detection of microcantilever movements induced by variations in surface stress. Our approach using the SECM will be illustrated for the detection of microcantilevers deflections during the electrochemically-assisted adsorption of Br onto gold coated cantilevers. After the validation of the proposed principle, the cantilever deflection properties will be detected in the case of the adsorption of an antibody in a heterogeneous immunoassay at an allergen-coated microcantilever platform.

Chapter 1 :Bibliographic review

The rapid, selective and sensitive detection of surface phenomena is a subject of interest for a wide area of applications in various scientific domains. The well expanded technique for detection of specific reactions on different substrates (chemical, physical-chemical) is by far represented by biosensors. Their principle consists of a specific binding of the analyte of interest to the complementary bio-recognition element immobilized on a suitable support medium. The specific interaction results in a change in one or more physico-chemical properties measured directly by the transducer. The produced electronic signal is proportional in magnitude or frequency to the concentration of the sensed analyte. To optimize and interpret the sensor response, the surface architecture, surface functionalisation and the chosen sensor transducer must be considered. It is also advantageous to use complementary characterization tools [1]. The optical microscopy has been known for long as a simple tool to characterize modified surfaces. Optical microscopy is largely used because visible light allows direct observation by the human eye. For some applications the optical detection can be a powerful instrument to confirm the biosensing of a target analyte [2]. Because of possible sample degradation and contamination, it is interesting to develop small, lightweight and portable devices. The continuous development of microfabrication technologies in the area of miniaturized transducers has increased the feasibility of portable biosensors. During recent years, the progress in the field of lasers and light emitting diodes (LEDs) allowed the fabrication of light sources with wider range of wavelengths at lower prices and with a lighter weight.

The main advantages of optical detector are: i) the detection is quick, ii) the electrical contact with the surface is not required, iii) it is possible to get valuable information from multi-analyte detection at different wavelengths, and iv) the surface response may be mapped via 2D imaging techniques[3].

The optical sensing of a target can be detected directly or indirectly through optically labeled probes. Consequently, the optical transducers are able to detect changes in absorbance, fluorescence/phosphorescence, reflectance, light scattering or refractive index[4]. This explains the increased use of optical transduction over the popular

electrochemical methods of detection. The most used optical biosensors proceed via: fluorescence-based detection and label-free detection.

I. *Different optical methods of sensing and detection*

I. 1. *Fluorescence microscopy*

Fluorescence is an optical method widely used for sensing due to its selectivity and sensitivity. A fluorescence-based device monitors the frequency change of electromagnetic radiation emission stimulated by previous absorption of radiation and followed by generation of an excited state with a short time of life.

Three methods for fluorescence detection can be distinguished: i) direct sensing, when a specific molecule is detected before and after a reaction or change; ii) indirect sensing – when a dye is added to optically transduce the presence of a target molecule; iii) FRET – fluorescence energy transfer, which correspond to a non-radiative energy transfer from an excited molecular fluorophore (a *donor*) to another fluorophore (*an acceptor*) through intermolecular long-range dipole-dipole interactions. FRET can be used to visualize and quantify the position and concentration of interacting fluorophores[5, 6]. Even if this type of detection is extremely sensitive reaching the detections limit of a single molecule[7], this technique also have some drawbacks. In some cases, the labeling of molecules is impossible to realize, or this step is too long, or may to interfere with the function of the biomolecule. Quantitative analysis is difficult, due to the fluorescence signal bias, as the exact number of fluorophores on each molecule cannot be controlled[8]. Due to previously enumerated factors, it is obviously why the label-free detections are preferred. The label-free detection is a relatively easy and cheap to realize, allowing quantitative and kinetic measurements of molecular interactions. A large family of label-free techniques is based on measure of change of refractive index generated by molecular interaction, which is dependent on target concentration or surface density. It should be mentioned that this approach is interesting, when ultrasmall detection volume is used, compared to the fluorescence type of detection, for which the signal is depending on the total number of analytes in the analyzed volume or detection surface.

I. 2. *Detection based on interferometric measurements*

A simple alternative for high-throughput label-free biomolecular interactions was presented by the group of *M. Selim Ünlü et al.[9]*. This technique is based on the monitoring of the optical phase difference (OPD), which appears due to accumulation of biomolecules. The variations of the optical phase difference are accessed with a high sensitivity and resolution from interferometric measurements. Thus, the proposed platform SRIB (spectral reflectance imaging biosensor) uses spectroscopy to evaluate the interference signature of light reflected from a layered structure, giving the possibility of an accurate determination of the optical thickness of a specific transparent film (Fig.1.1).

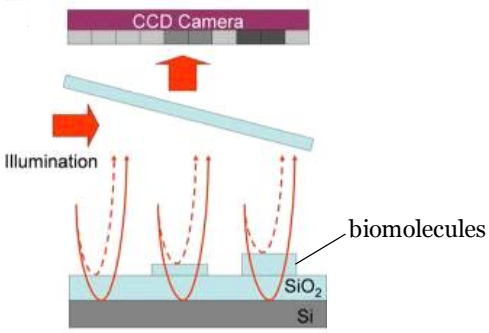

Figure 1.1 Basic principle of SRIB (spectral reflectance imaging biosensor)

The layered substrate is made of a silicon wafer with a top layer of thermally grown silicon dioxide (SiO_2), which serves as the solid support for an additional material such as biomolecular probes. The quantity of the total reflected light at a specific wavelength depends on the OPD between the top surface of the transparent film and the bare reference surface at the SiO_2-Si interface. When species bind to the surface, the OPD will increase accordingly, resulting in a characteristic shift of spectral reflectivity.

Compared to gold and glass surfaces, the chemical composition of the SiO2 surface is perfectly established, which allows obtaining repeatable surface functionalization. This is important, as the sensitivities of all detection methods are strongly dependent on the functional probe density and surface uniformity.

A polished, thermally grown oxide layer as reflecting substrate is preferred instead of a conventional glass substrate, due to a better uniformity and smoothness of these substrates. The SRIB is similar to SPR, as it is not influenced by the changes in concentration away from the surface. Then, the SRIB signal response is independent of temperature and refractive index changes in bulk solution. It is also independent of the specific conformation of molecules on the surface. If compared to other label-free detection methods, particularly the SPR (surface plasmon resonance) which is a leading technique in this domain, some advantages can be indicated. First, the techniques which use broadband light sources and spectrometers are single-point detection methods. Then to obtain the image, it is necessary to scan the substrate with additional illumination and collection optics. Therefore, this method is applicable only in the case of low-throughput samples with limited dynamics, due to the decrease of the imaging rate with the sample size increase. The performance of this label-free technique was showed for the multiplexed and dynamic detection of protein-protein interactions over hundred of spots simultaneously with a high sensitivity (≈19 ng/ml). More recently, using the same technique dynamic imaging of antibody-antigen and DNA-DNA interactions, as well the detection of antibody-whole virus binding was demonstrated[10].

I. 3. *Refractive index change detection techniques*

I. 3. 1. Surface Plasmon Resonance

The performance of surface plasmon resonance (SPR) for biosensing was evidenced in 1983 by Liedberg et al.[11]. It is a very powerful label-free tool to study the interactions between a target and a molecule that allows biorecognition. SPR is sensitive to local refractive index changes at or near the metal surface and can be used to study the specificity, affinity and kinetics of biomolecular interactions and measure the concentration of analytes in complex samples. The SPR changes induced by the binding of target molecules to the sensing area can be detected by monitoring the resonant angle[12], resonant wavelength[13] or resonant intensity[14]. Four basic methods to excite the SPR can be mentioned, as shown in Fig. 1.2: prism coupling (A) [15], waveguide coupling (B) [16], fiber optic coupling (C,D) [17] and grating coupling (E) [18, 19].

In the case of prism coupling configuration (A), a light of a certain wavelength approaches a glass substrate, the amount of light that is reflected off the substrate increases with the angle of incidence until the critical angle θ_c is reached, where the light is totally reflected back. The total internal reflection occurs for all angles greater than or equal to the critical angle. When the opposite surface of the substrate is coated with a thin metallic layer, another angle greater than θ_c is obtained, and the light instead of being totally internally reflected back is 'coupled' into the metallic film, producing a minimum in the reflected light intensity. This phenomenon results from oscillations of mobile surface electrons that propagate along the boundary of the metal film (gold or silver) and the dielectric substrate close to it, causing the surface plasmon wave. The angle for which this minimum occurs is called the SPR angle - θ_{spr}.

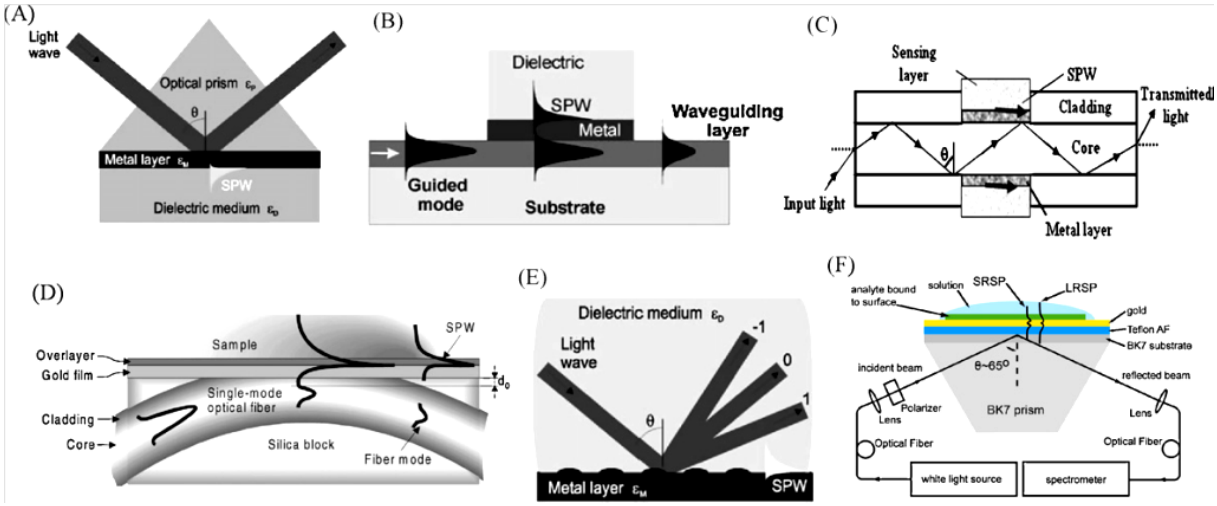

Figure 1.2 Various SPR sensor configurations (A) Prism coupling, (B) waveguide coupling, (C) optical fiber configuration , (D) side-polished fiber coupling, (E) grating coupling, (F) long-range and short range surface plasmon (LSPR SRSP)

At θ_{spr} the light provides the quanta of energy that the metal layer can absorb. The evanescent field of the resonance travels into the adjacent dielectric medium a few hundred nanometers from the metal surface and decays exponentially with the distance from the surface. The frequency of the plasmon wave and θ_{spr} are critically dependant not only on the physical nature of the metal boundary layer, but also on the dielectric properties of the adjacent medium in contact with the metal film.

The prism coupling is the most convenient SPR configuration with the best detection limit, about 1-100 ng/ml (Fig. 1.2 (A))[20]. However, the prism is bulky, and sometimes is difficult to integrate.

The wave-guide coupling is an alternative to the prism coupling configuration. Then, the light propagates in a waveguide through total internal reflection and generates an evanescent field at the waveguide-metal interface which excites the SPW (surface plasmon wave) in the same way as for the prism configuration (Fig. 1.2(B)). Optical fibers are two-dimensional waveguides, used to excite the surface plasmon wave in different configurations.

In another configuration, a small portion of the fiber is removed and coated with a layer of a metal film (Fig. 1.2(C)). Several optical fiber SPR biosensor configurations have been developed based on side-polished single mode fiber (Fig. 1.2(D)).

Additionally, the SPW can be excited by grating coupling (Fig. 1.2 (E)), which can be a good alternative for low cost mass production. If a metal-dielectric interface is periodically distorted, the incident optical wave is diffracted forming a series of beams directed away from the surface at different angles. The component of the momentum of these diffracted beams along the interface differs from that of the incident wave by multiples of the grating wave vector. If the total component of the momentum along the interface of a diffracted order is equal to that of the surface plasmon wave, the optical wave may couple to the surface plasmon wave.

All the presented SPR configurations have low detection limits to detect one analyte. Nevertheless, two drawbacks should be mentioned, which can limit the SPR biosesing in some fields:

- the evanescent field can penetrate into surrounding medium only for about 100-200 nm, which can be a potential issue to detect large molecules of interest as cells and bacteria.
- there is only one SPW to detect the change in refractive index, making impossible the distinction between the surface refractive index change and the bulk solution, which can perturb the sensing performance, for sensing in blood samples for example.

To overcome these limitations, a new optical structure has been developed, as illustrated in Fig. 1.2(F). The metal layer is inserted between two dielectric layers with a similar refractive index [21-23]. Two new surface plasmon modes called long surface plasmon resonance (LSPR) and short range surface plasmon (SRSP) are formed, at both metal-dielectric interfaces. For dual mode configuration of the LRSP and SRSP, the sensor is now then able to differentiate the change of refractive index in the background from that due to binding at the surface. In this configuration, LSPR has a longer penetration length in the surrounding medium, making it suitable for cell and bacteria detection with a low detection limit.

As the SPR is recognized for its high sensitivity, but is limited to the detection of only one analyte, the next step in the progress of the technique is to develop SPR configurations capable of multi-analyte detection.

I. 3. 2. Interferometers

Another very high sensitive technique to detect refractive index changes consists of using an interferometric set—up, such as the Mach-Zehnder interferometer.

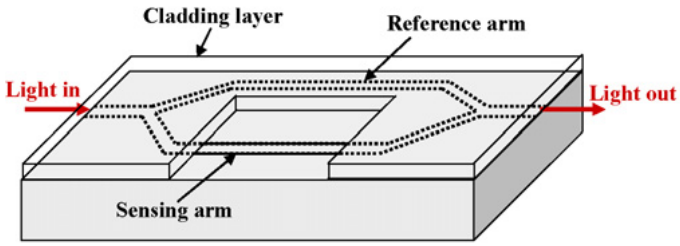

Figure 1.3 Mach-Zehnder interferometer sensor

In the Mach-Zehnder interferometer, a coherent, single frequency, single polarization light from a laser enters a single-mode input waveguide and is split equally at an Y-junction into two arms, for respectively, the reference and the sample. The sample arm is uncovered allowing the evanescent field of that branch to interact with the sample while the reference branch is protected from the sample by a cladding layer. (Fig.1.3). The two arms recombine at the output, resulting in interferences whose

intensity is measured by a photodetector. A change of refractive index at the surface of the sensing arm modifies the optical phase resulting in a change in the light intensity measured at the photodetector. In an interesting application of this type of interferometer, microfluidics and optics were integrated in a biosensor [24].

The principle of the Young interferometer is almost the same, but instead of recombining the sample and reference arms, the optical output of the two arms combines to form interference fringes on a detector screen. To evaluate the position shift in the interference pattern, a Fourier transformation method is applied[25].

I. 3. 3. Resonant mirrors

Resonant mirrors are another configuration of a biosensor with an optical detection based on the creation of an evanescent field [26, 27]. A resonant mirror is made of several layers: a sensing surface, a high refractive index dielectric resonant layer (waveguide made of, for example, titania), a low index spacer layer (silica) and the prism, which is a substrate with a high refractive index, as in Fig. 1.4.

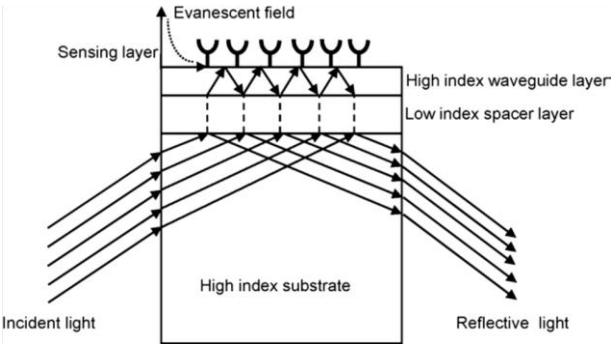

Figure 1.4 Resonant mirror structure

The light passes through the prism to the low-index medium. The low index coupling layer transfer the light to high refractive index substrate by waveguiding where the light couples and the evanescent field will appear and will travel into analyzing medium, before coupling back into the prism. Transferring the light into and out the resonant structure is depending of initial angle of the incident light. This configuration allows to measure thickness and refractive index changes in the sensing layer with a high resolution (~ 0.1 Å for the thickness and ~10^{-4} in refractive index).

I. 3. 4. Optical ring resonators

Another interesting configuration of biosensors, which is highly sensitive is the optical ring resonator[28-30]. This system detects a chemical or biological analyte by converting the signals from light – analyte interaction into a measurable optical signal. The light is travelling according whispering gallery modes (WGMs) or circulating waveguide modes, resulting from the total internal reflection of the light along the curved boundary between the high and low refractive index media as in Figure 1.5.

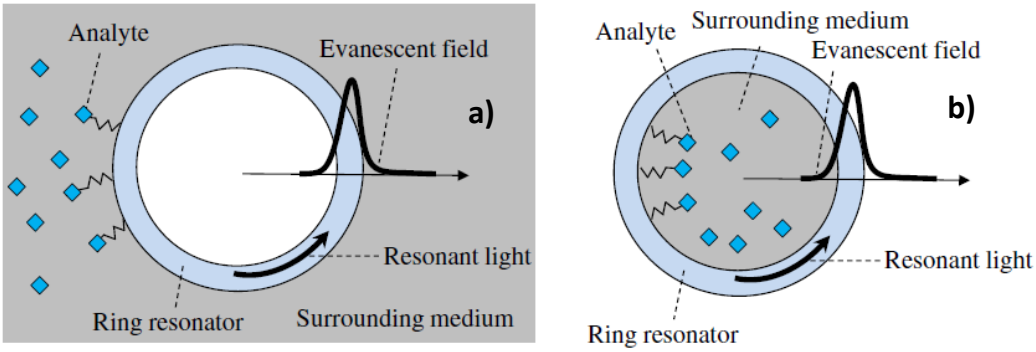

Figure 1.5 The principle of optical ring resonator sensor: the light circulating along the resonator and its evanescent field is present in the surrounding medium outside (a) or inside (b) the ring resonator, interacting with the analyte on the ring resonator exterior surface (a) or interior surface (b) and in the surrounding medium

The detection of surface and bulk changes of refractive index is possible with low detections limits, about 60 fM[31]. For some applications, instead of measuring the refractive index change, other sensing signals such as fluorescence, Raman or optical absorption can be detected with the same system.

I. 3. 5. Optical fibers biosensors and Fiber Bragg gratings

Optical fibers can be a good alternative as materials for optical sensors. They are made of silica and the light is transmitted along their axis by total internal reflection. The structure of a fiber is made of two dielectric materials (core and cladding). The core with a higher refractive index is covered by the cladding (with a lower refractive index), as represented in Fig.1.6.

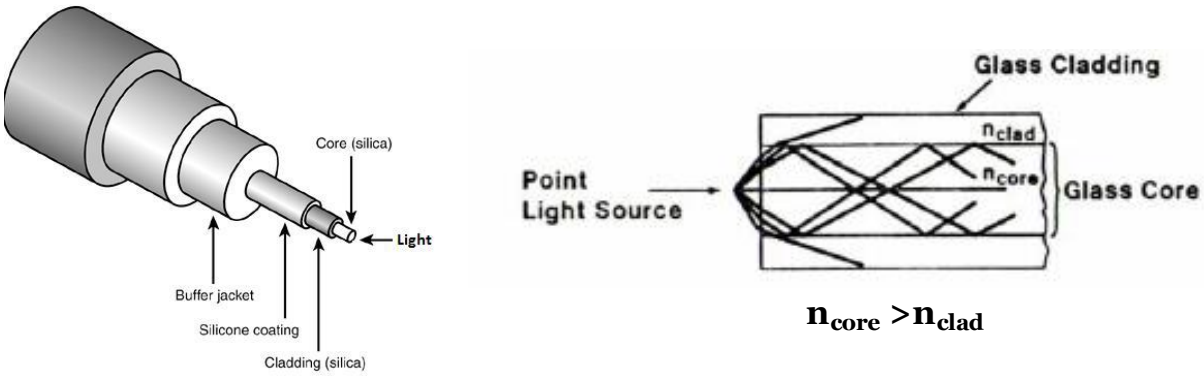

Figure 1.6 The schematic of an optical fiber

As almost all light is internally reflected, the evanescent field can appear and penetrate into the cladding layer. To allow the interaction of the evanescent wave with the surrounding medium, the fiber should be modified, in order to have a cladding thinner than the core. These biosensors can be divided into two groups: intrinsic and extrinsic. For the intrinsic sensors, an element of the optical fiber interacts with the analyte, while the extrinsic sensors serve only for light coupling into the fiber. As the construction of optical fibers already reaches submicrometer dimensions, the application for single cell sensing can be envisioned. Due to the optical nature of both excitation and detection, the optical fibers signals are not influenced by external factors such as electromagnetic interferences from static energy or surface potentials.

A particular case of optical fibers system, is the Fiber Bragg gratings[32]. The core of optical fiber is modified by printing periodic structures, by UV radiations or by local etching with hydrofluoric acid (HF).

After this modification step, for a small part of optical fiber, structures with periodical variation of the refractive index are observed (Fig. 1.7).

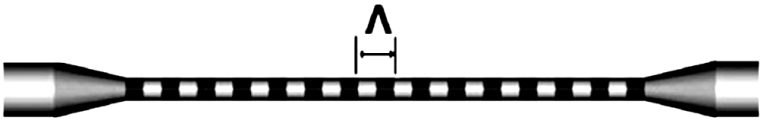

Figure 1.7 The diagram of a FBG (fiber Bragg grating) on a etched fiber

For a specific light wavelength, called the Bragg wavelength (λ_B), the reflectivity is maximum and the light is reflected back up along the fiber, as the reflections from each sub-structure are in phase with the printed pattern separation period. For light wavelengths different on the Bragg wavelength (λ_B), the light wave is transmitted. The Bragg wavelength (λ_B) is given by:

$$\lambda_B = 2n_{eff}\Lambda$$

where n_{eff} is the effective refractive index of the mode propagating in the fiber, and Λ is the FBG (fiber Bragg grating) period. By detecting the shifts for the Bragg wavelength, this system can be used as a refractive index sensor, with application in biochemical sensing[33]. An advantage of these devices is that they can be coupled in series, allowing the simultaneous measurement of different parameters.

I. 4. *Ellipsometry*

Ellipsometry allows depth characterization of different systems or phenomena occurring at various interfaces (solid-air, liquid-air). This optical technique is non-invasive and highly sensitive for in-situ investigation of thin films and for analysis of optical properties of surfaces. It is applied to evaluate simultaneously and quickly a film thickness and the refractive index of a deposited film[34].

I. 4. 1. Principle

The principle of this technique relies on the measurement of the change of polarization due to light reflection at the sample surface.

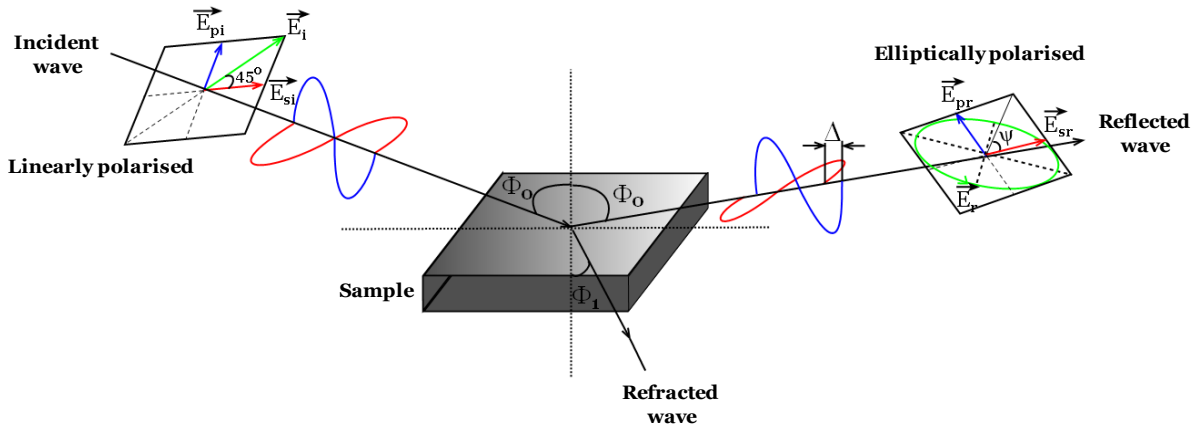

Figure 1.8 Ellipsometry principle: p, s-parallel and perpendicular direction of light components to the plan of incidence; Φ_0-incidence angle; Φ_1 – refractive angle

In the case of the reflection of a linearly polarized light at oblique incidence from a sample surface, the reflected light is elliptically polarized (Fig. 1.8). The shape and orientation of the resulting ellipse is directly dependent on the angle of incidence, the initial direction of the polarization of the incident light, and the reflection properties of the surface. The modification in the state of polarization can be represented as the ratio of complex reflection coefficients:

$$\rho = \frac{r_p}{r_s} = \tan\psi e^{i\Delta}$$

where r_p and r_s correspond to complex reflection coefficients of light linearly polarized parallel (p) and perpendicular (s) to the plane of incidence. **Δ** and tan **ψ** are the relative phase and amplitude change respectively, between p and s polarized components due to reflection from the surface.

By knowing the state of polarization of the incident light wave, we can determine the ellipsometric angles **Δ** and **ψ**, from the measurements of the state of polarization of the reflected wave.

In the example shown in Fig. 1.8, for a linearly polarized incident wave with its electric vector oriented at 45 degrees to the plan of incidence, **Δ** and tan **ψ** characterized the elliptically polarized reflected wave. The optical constants and thickness of a deposited film are estimated as the result of an iterative calculation process using appropriate optical models. The area of the analyzed surface is usually a few square millimeters. The setup proposed by Sugimoto and Matsuda permit to determine the thickness and optical properties of a thin film on an area about 10 μm in diameter[35]. Two groups of lenses are held behind the analyzer of a common polarizer-compensator-analyzer configuration, in order to magnify the polarized reflection image of the specimen. In this way, a magnification of x600 can be obtained, allowing the measuring of **Δ** and **ψ** in this micrometer zone.

I. 4. 2. Spectroscopic and multiple-angle ellipsometry

Usually, to determine the thickness and refraction index of a transparent deposited film, the ellipsometry measurements are carried out at a single-wavelength and a specific angle of incidence. The incident angle is chosen to achieve the highest sensitivity for the deposited layer thickness determination; it depends on the optical constants of samples.

For some applications, such as spectroscopic ellipsometry and multiple-angle ellipsometry, the wavelength and the incidence angle, respectively, are varied. By changing the wavelength of the incident light, it is possible to get ellipsometric measurements with high precision and very high thickness sensitivity (~0.1 Å)[36]. With this technique one also accesses optical constants (complex refractive index or complex dielectric constant)[37, 38] and to the analysis of multilayer thin film structures.

Depending on the wavelength range used, further parameters can be apprehended. In the case of UV/VIS region interband transitions, band gap of high energies can be described. From the band structure data, properties which are directly related as alloy composition, grain size or phase structure can be revealed. Infrared ellipsometry is also very interesting, as in this region the appearance of particular phenomena as free-carrier absorption induced by free electrons (or holes), molecular vibrations and

phonon absorption, allows to study electric properties and local atomic structures of the layer such as for Si–H and –OH[36]. Infrared ellipsometry can be also employed to characterize in detail layers such as coatings, surface films in the subnanometer range, reaching 1/1000th part of the wavelength[39].

Using multiple angles of incidence allows to enhance the accuracy of ellipsometric measurements. It can be used as a tool for characterizing and understanding the physical properties of materials[40, 41], especially if coupled with other techniques, as for VASE approach[42] (variable angle spectroscopic ellipsometry).

I. 4. 3. Ellipsometry used to characterize electrochemical processes

Ellipsometry allows to modify surfaces in numerous applications ranging from chemical sensing to lab-on-a-chip, corrosion inhibition, microelectrodes, electrocatalysis[43] and biosensing[44, 45]. It is then crucial to be able to monitor the coatings formations mechanism from both chemical and physical points of view with a good spatial and temporal resolution.

Ellipsometry techniques were extensively used to characterize such surface modifications, before the development of surface characterization microscopies such as STM or AFM in the late 1980's. During an electrochemical process, the classification of the surface film either as an insulator, a semiconductor or a metal is very important. This information can be obtained from the magnitude of the extinction coefficient of the film, corresponding to the imaginary part of the complex index of refraction.

More generally, during the growth of a film on a surface, whatever the means to get it, the light dispersion, which describes the variation of the real part of the refractive index with the wavelength, is modified due to interband transitions (VB and CB), and also as a result of intraband transitions resulting from delocalized electrons. More details on the electronic properties of the deposited film can be obtained using spectroscopic ellipsometry which provides the spectral features of the complex refractive index of the film. As ellipsometry measures the energy loss through absorption, along with the variation of the real part of the complex refractive index,

more rigorous data can be obtained for a layer which is totally nonabsorbing in the studied wavelength region.

I. 4. 4. Determination of Film Thickness: electrochemistry vs. ellipsometry

A common application of ellipsometric measurements when a film is formed at a surface consists of detecting the film thickness and the rate of its growth. Under electrochemical conditions, the determination of the film thickness is also possible from Faraday law and mass conservation. A non electrochemical technique, such as ellipsometry, provides an independent method to characterize the layer, which allows for the estimation of the electrochemical reaction yield.

Indeed, when the faradic yield of the reaction is lower than 1, and for heterogeneous films which show different levels of porosity, the thickness of the deposited layer cannot be estimated from the coulometry. Even if a reaction has 100 % faradic efficiency, as for example for the growth of a thick oxide film, the ellipsometric measurements reveals that at the beginning of the deposition process, the faradic yield can be different. Such an example was showed in the case of the growth of a molybdenum oxide in acetic acid, where the delay between the film growth and the increase of the voltage for initial stages was assigned to a simultaneous process of the film growth with the metal dissolution[46].

Another interesting way of characterizing a deposited layer consists in revealing qualitatively its porosity. It was shown that the deposition of hydrous oxide films fits an electrochemical model, which considers a uniform film. But when coupling ellipsometric measurements with quantitative elemental analysis of the same hydrous oxide films, the high porosity of the film is evidenced with a 20% difference in the volume density compared to the compact oxide[47].

I. 4. 5. Coupling ellipsometry to AFM

When it is important to obtain accurate geometrical parameters of the deposited films, such as thickness and roughness, ellipsometry can be coupled to atomic force microscopy (AFM). This coupling allows to apprehend better and obtain higher precision in surface science, as AFM offers a local measurement technique, compared to ellipsometry, which averages the response of a macroscopic area[48, 49].

II. *Coupling optical techniques with electrochemistry*

II. 1. *Ellipsometry coupled to electrochemistry*

The combination of ellipsometry and electrochemistry techniques for *in-situ* and real time analysis has been used in various domains such as corrosion processes[50], study of oxide film properties[51, 52], polymer multilayer film formation[53], or investigation of permeability and stability of layered polyelectrolyte films[54]. For this coupling of techniques, the optical properties measured are dictated by the nature of the electronic states in the surface phase formed on the electrode and by nature of the interaction of the electromagnetic probe with these states[55].

An alternative way to understand the complex behavior of electrode surface during electrochemical processes is the complementary association of other in-situ techniques to ellipsometry, such as quartz crystal balance (QCM)[56, 57]. This association allows characterizing the 2 steps chemisorption of alkanethiols SAM on gold with ability to obtain the deposited film thickness and porosity with respect of time[58].

II. 2. *Coupling SPR to Electrochemistry*

Thus, depending on application and on needed information, alternative techniques can be used. For example, the measurements through optical techniques are very fast and easy to realize. The ellipsometry or reflectivity techniques which are possible also at different interfaces can provide average measurements on larger areas. To overcome some practical limitations by applying a singular technique, it can be observed during last years the appearance of coupling between different techniques to improve their performances while obtaining more varied information related to analyzed surface properties.

In this way, the sensitive optical technique that can be combined to electrochemistry is the Surface Plasmon Resonance (SPR). Then, electrochemistry is used to generate reactions at a substrate, while in the same time the change of the optical properties is monitored. The SPR is well known for its efficiency in characterizing different types of ultrathin films from structural and optical points of view, and also for its sensing applications.

The Dong's group has shown that during the electrochemical oxidation/reduction of a polyaniline (PAn) film on a gold electrode, transitions in the conductivity contribute to a large change of the surface plasmon resonance (SPR) response. This results from the modification in the imaginary part of the dielectric constant of the PAn film[59]. Based on these effects, an electrochemical SPR biosensor has been built. The response of SPR is amplified during the redox transformation of the PAn film due to the enzymatic reaction between horseradish peroxidase (HRP) and PAn in the presence of H_2O_2. Compared to a simple binding assay sensor, the electrochemical one has the advantages of a larger SPR response and also of the system electrochemical reversibility.

By combining SPR to electrochemistry, more information on in-situ kinetics, or doping-dedoping processes[60], or optical changes during the electropolymerization of electroactive monomers[61, 62] can be obtained. Various conductive polymers such as polyaniline[63] or polypyrole derivatives[64] have been used in gas sensors and biological systems containing glucose and enzymes.

An SPR immunosensor based on an electropolymerized amino benzoic acid film was recently presented. It is used to electrochemically detect human IgG in neutral pH solution at different constant applied potentials [65]. Depending on the biased potential, the morphology of the immunosensor surface is changed leading to enhancing or reducing the quantity of bounded human IgG. A minimal detection of 1µm/mL of human IgG was shown.

Different sensing applications coupling electrochemistry with SPR can be found, in which the EC-SPR measurements allow apprehending in-situ thin layer formation, the immobilization of a probe followed by the sensing of target through antigen-antibody interaction.

Let us mention protein immunosensing[66], the bioelectrocatalyzed oxidation of glucose or lactate[67], glucose biosensing[68] or detection of an enzymatic reaction in bilayer lipid membranes[69].

III. *Optical imageries coupled to electrochemistry*

III. 1. *Development of ellipsometric imagery*

To get information from ellipsometry, an optical model adapted to each specific case must be built, which in some cases can be laborious, with difficulties to interpret data that result in errors on calculated values of the optical constants.

Because of beam size (~1mm²), conventional ellipsometry does not allow studying accurately microstructured surfaces. The first high spatial resolution approach was reported by Erman *et al*[70]. It is called “scanning microellipsometry”, or “microspot optics ellipsometry”. The beam of a standard ellipsometer focused to a thin spot size is scanned back and forward to cover the whole surface of the sample. As the observation and illumination are performed with a finite numerical aperture, the incidence angle is not well defined, which can affect the ellipsometric performance if the spatial resolution is driven beyond 10 µm[71] and the time to obtain an image is too long.

The need to analyze the microscopic details of ultrathin surface structures was the argument to develop imaging ellipsometry, by coupling high spatial resolution of optical microscopy with thin-film measurement performances of ellipsometry[72]. The principle of this imaging technique is based on conventional ellispometry, with collection of the reflected light from the analyzed sample on a charged coupled device (CCD) camera. Hence, the spatial details of surface film thickness can be extracted from pixel to pixel analysis.

The first imaging ellipsometer microscope was proposed by Beaglehole's group[73]. An objective lens is used to obtain the magnified image of the surface on a CCD array, which allows enhancing the image resolution to 1-2μm. However, since different regions of the surface are at different distances from the objective lens, and because the image plane is not perpendicular to the direction of the reflected light, the resulting image of the surface in some parts is out of focus, due to limited depth of field in focusing the image.

A new instrumental configuration based on the reflection at the Brewster angle was built by Hénon and Meunier[74]. The drawback from Beaglehole's setup was overcome by mechanically shifting the object lens and collecting light only from focused regions, allowing a final reconstruction of a whole focused image. Another system, which operates at non Brewster angle was developed by Cohn *et al*[75]. They proposed a new rapid full-field imaging technique for high spatial resolution studies of thin films named "Dynamic imaging microellipsometry" (DIM).

To solve some issues related to defocusing, beam translation or pixel by pixel calibration, a new two-dimensional (2D) imaging ellipsometric microscope was constructed by Pak *et al*.[76].

The optical system for all setup described above is based on the standard PCSA configuration (polarizer, compensator or retarder, specimen, and analyzer).

Using another configuration, the highest lateral and thickness resolution was obtained with the setup of Neumaier *et al.[71]*. This system is characterized by a light beam focused into the back focal plane of an infinity-corrected high-power microscope objective. Therefore, the object located in the front focal plane of the objective, is illuminated with a parallel beam of polarized light, which attains the

substrate under a shallow angle (Fig. 1.9). The angle of incidence can be easily controlled and full field of view of the lens is in focus. This setup reports for the first time a lateral resolution below 1 μm and of about 1 nm in thickness.

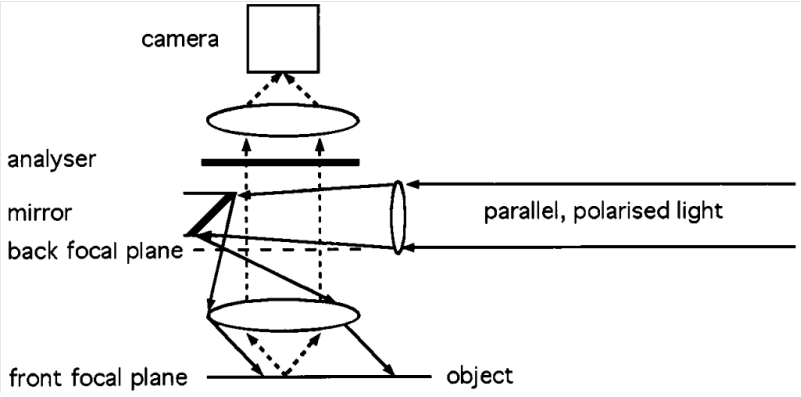

Figure 1.9 Principle of imaging ellipsometric microscopy – Neumaier's setup

This setup combines the advantages of light microscopy with those of ellipsometry [77, 78]. It was used in different applications to confirm its capability of quantitative ellipsometric measurements with a high lateral resolution. A coupling of ellipsometric imagery technique based on the Neumaier's setup, which presents the best measurement resolution (lateral and thickness) so far, and electrochemistry is not known. Nevertheless, an application coupling these two techniques based on another configuration with less good resolution is presented by Yu *et. al.*and [79].

III. 2. *SPR imaging techniques coupled to electrochemistry*

III. 2. 1. Surface Impedance Imaging

The group of N.J. Tao *et al.* has proposed a setup capable of imaging surface impedance[80]. It is based on the sensitive dependence of surface plasmon resonance (SPR) on the local surface charge density, a phenomenon confirmed by electroreflectance spectroscopy[81]. A potential modulation is applied to the sensor surface and three images corresponding to i) the dc (direct current) component, and ii) amplitude and phase of the ac (alternative current) component are collected simultaneously. The dc image measures the local molecular binding activity on the surface as for conventional SPR imaging, while the ac images show the direct

contribution of the surface local impedance. The interfacial impedance can be represented as: $\boldsymbol{Z=\Delta V/\Delta I}$, where ΔV correspond to the potential modulation applied to the electrode, and ΔI is the current response to the potential modulation. Since the impedance is very sensitive to any interfacial change at the electrode surface, it allows to evidence molecular adsorption. The interfacial impedance can be obtained from SPR measurements. Indeed, the applied potential modulation induces a modulation of the surface charge, which modifies the surface plasmons in the metal film. From the measurements of the amplitude and phase of the resonance angle (the incident angle at which the evanescent wave is formed and the surface plasmons appear) the data related to interfacial impedance can be accessed. The schematic diagram of the proposed setup is shown in the Fig.1.10.

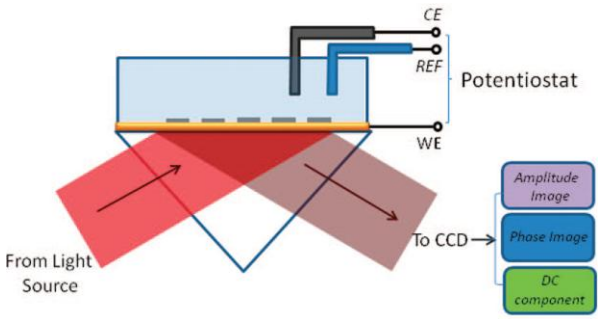

Figure 1.10 Surface impedance imaging setup

Then, the coupling of the SPR and impedance techniques can be applied to local surface characterization, along with acquiring some data, not attainable by the conventional SPR imaging technique.

III. 2. 2. Imaging Local Electrochemical Current via Surface Plasmon Resonance

More recently, the coupling of SPR with electrochemistry has been used to measure local variations of the electrochemical current through optical imagery of the signals recorded from SPR [82]. Compared to other electrochemical surface characterization techniques, as for example the SECM, the local electrochemical current is imaged without any electrode or scanning probe.

Thus, the main advantages of this approach are i) the rapid and non-invasive electrochemical current imaging of the surface and ii) the proportionality of the measured local current with the optical signal, without being scaled with the area of the analyzed area.

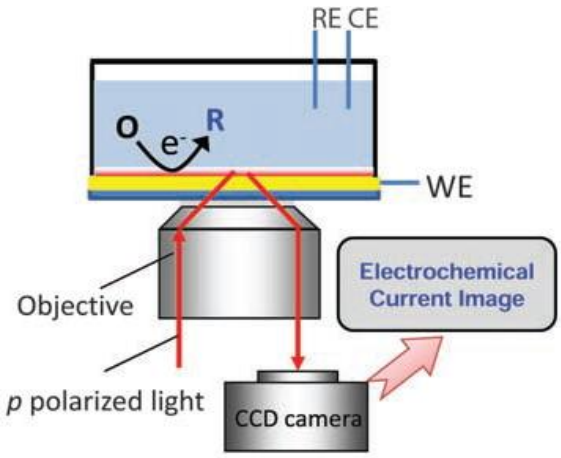

Figure 1.11 Schematic diagram of the setup for imaging local electrochemical current through SPR

The schematic diagram of the setup is presented in the Fig. 1.11. The electrochemical reaction occurring at the electrode corresponds to the electron transfer between the electrode and the reactant in solution. The electrochemical transformation of the chemical species upon the electron transfer at the electrode is detected optically from changes in the SPR signal.

The smallest interrogated areas were as small as 0.2 μm x 3 μm with a current sensitivity of 0.3 pA. This technique has revealed its specific capabilities for studying the heterogeneous surface reaction, and also for the analyzing of chemical traces polluting the electrode surface.

IV. *Surface reactivity interrogated by local probes: coupling with optical imageries techniques - a tool for confined chemical surface imaging and characterization*

IV. 1. *Chemical surface activity interrogated by SECM*

The SECM (Scanning Electrochemical Microscopy) is a very popular analytical method used to study structures and processes at the micrometer to submicrometer range. It allows characterizing the electrochemical reactivity of different interfaces. It has been used to investigate electron, ion or molecule transfers at solid-liquid, liquid-liquid, and liquid-air interfaces [83].

The principle of this technique is based on measuring the current, which flow through a local probe (electrode tip) held in a solution at a close distance from a conductive, semi-conductive or insulating substrate. By moving the probe above the surface, the collection of redox processes at the substrate can be monitored at the tip with a simultaneous collection of topographical information[84]. This situation corresponds to the imaging capability of the SECM.

If compared to conventional electrochemical techniques, the SECM has the advantages to probe local properties of an interface whatever its electrical nature or connection. The detailed principle and theories of SECM, with the most attractive applications have been carefully selected and presented in different papers[85-87], books chapters[88] or review articles[89-91].

The most important feature for the SECM measurements is related to the dimension of the local probe (UME-ultramicroelectrode), which is directly related to the spatial resolution. Owing to the current possibilities to fabricate UMEs with diameter less than 1 μm, the resolution of electrochemical measurements is enhanced, and additionally, applications of SECM at the nanoscale can be envisioned. The current nanoscale studies by SECM are focused on the characterization of biological and biomimetic systems where the nanoscale spatial resolution is efficient to study for membranes or living cells [92, 93].

IV. 2. *AFM and STM - local probes for substrate topographic imaging*

The main and mostly used techniques for surface characterization with a high resolution are scanning probe techniques: the STM (scanning tunneling microscopy) and the AFM (atomic force microscopy tunneling microscope). The STM initially developed by Bining and Rohrer[94] has lead to the development of AFM. The basic principle of these two techniques relies on scanning a local probe (nanoprobe) over a surface, with a simultaneous observation of the interactions between the local probe and the surface. These techniques are differentiated through the nature of the monitored properties between the probe (nanoprobe) and the surface. In the case of STM, the tunneling current between a metallic tip placed at an atomic distance from a conductive substrate is observed. The applications of STM are numerous, from measurements in air, water, liquid or gas, in a large range of temperatures. Although highly sensitive, with a lateral resolution of about 0.1 nm and a depth resolution of 0.01nm, which allow analyzing surfaces at atomic level, the development of this technique was pulled back by the requirement of a conductive substrate. However, this requirement was fulfilled in applications where a conductive or semiconductive surface is modified by electrochemistry with the simultaneous imaging through STM. The group of *Allongue et al.* used STM imaging to characterize the modifications of different substrates by etching [95-97] or by metal electrodeposition[98, 99]. Thus, this approach allowed characterizing more precisely the mechanisms of surface modification processes and then developing new insights in surface chemistry and anisotropy of reactions.

The requirement of using a conductive substrate for STM, was the main reason for developing of the AFM technique. The AFM provides direct measurements of surface topography by measuring intermolecular forces, such as the Van der Waals forces. In the non-contact mode, a cantilever tip approaches within some angstroms the sample surface; thus, long range attractive forces are detected. When the tip hits the surface, the AFM mode turns to the AFM contact mode and short range repulsive forces are measured. The first difference with STM is that the AFM measurements are possible for conductive, as for insulating surfaces. It is much used for surface analysis at atomic resolution, but the main applications are in microbiology for imaging cells surfaces at high resolution[100] or for characterizing polymers[101-103].

AFM and STM are very powerful for surface characterization due to their capacity to distinguish structures at the nanoscale. However, a high resolution implies other requirement such as the accuracy for the positioning of the tip over the region of interest, along with the preference of very sharp tips. These requirements are time demanding, and it is only possible to move the tip in an area of at maximum of 200µm x 200µm.

While the initial generations of STM setups were based on a two-electrode cell configuration, for which the electron tunneling is obtained between the sample surface and the tip, Itaya *et al.* proposed a setup in which the sample and the tip are controlled separately with respect to a reference electrode potential[104]. Thus, the in-situ observation of the electrode surfaces during its electrochemical activation is possible. This configuration was validated in the case of the electrochemical deposition and dissolution of Ag on HOPG electrode.

The coupling of electrochemistry with STM (EC-STM) allows interesting applications in electrochemical deposition and dissolution[105-108], molecular adsorption[109-112], also for the study of electrode surfaces at molecular resolution[113-116]. The images of electrode surfaces were investigated in complex systems, as in the case of biological molecules [117, 118] or for the study of electrochemical reaction between organic molecules[119, 120].

The development of different indirect STM-based methods have permitted the enhancement of the temporal resolution, which consequently allowed to probe the processes with fast kinetic, as extracting electron transfer properties and the electronic states of the analyzed molecules[121].

IV. 3. *SECM coupled to AFM*

In the case of SECM imaging, when the sample topography and reactivity are imaged through the current response that depends on the tip position, some limitations can be pointed out. For example, when the sample presents variations in topography as well as in reactivity, it is difficult to efficiently evaluate these two components from SECM measurements at a fixed height. To solve this problem, a second redox mediator is added in the solution, to obtain only the information related to the

sample topography [122-124]. For the experiments that require a very high resolution, small local probes are used and positioned at a very close distance from the sample; then, the risk to break the probe and damage the sample structure is very high.

To overcome these drawbacks and obtain topographical and reactivity information independently, SECM was coupled to AFM, that is the most current technique for surface topographic characterization at atomic level (nanometer spatial resolution). Then, the AFM probe simultaneously records topographical and electrochemical image of the sample surface at enhanced spatial resolution [125-127]. So, the electrochemical probe is used to obtain local chemical information, such as the electrochemical reactivity and charge transfer, which is complimentary to topographic information provided by STM and AFM.

V. *Coupling between optical microscopy and local probes*

V. 1. 1. AFM coupled to optical microscopy

An alternative way to obtain more information from the SPM local probes techniques can be achieved by coupling optical microscopies with local probes. The combination of confocal fluorescence microscopy with the AFM has opened different new directions of investigations in biology. By correlating structural/nanomechanical changes with optical/fluorescence images, this coupling allowed to simultaneously study phenomena occurring at the cell surface and observe events occurring inside the cell. The AFM technique allows to evidence phenomena which are not optically addressable or are hidden by the diffraction limited optical resolution [128, 129] and also to image cells under physiological conditions [130].

The $\lambda/2$ limit imposed by the diffraction can be overcome by SNOM technique (Scanning Near-field Optical Microscopy). This technique is based on the detection of the evanescent waves which are directly dependent on the sub-wavelength sample

features. The SNOM probe tip can be integrated into an AFM cantilever for a final simultaneous AFM/SNOM operation, as represented in Fig. 1.12 [131].

The AFM is used as a regulation for the SNOM tip, because the amplitude of the optical near field varies intensely with the distance between the probe tip and the sample[132].

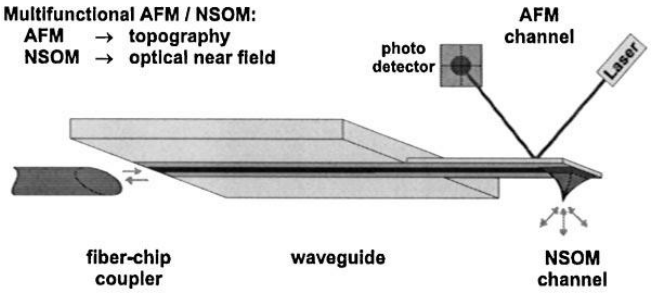

Figure 1.12 Concept of AFM/SNOM coupling, based on a standard AFM setup with a beam deflection distance regulation

An AFM cantilever is integrated with an optical guide on one side, forming the AFM-SNOM probe tip, and on the other side it is coupled to a standard optical fiber. Depending on the application, the sensor can be connected either to light emitter or detector. Thus, the sample topographical and optical properties can be investigated simultaneously.

V. 1. 2.SECM associated with OM (optical microscopy)

The coupling of optical microscopy with SECM allows a simultaneous analysis of the electrochemical and optical properties of the sample. To achieve this setup, it is necessary to design a special probe tip, which can operate as both a light source and a microelectrode; it is typically a metalized optical fiber. The tip fabrication is similar to that of a SNOM probe, and it includes some important fabrication steps: i) heating and pulling optical fibers; ii) metal coating; iii) electrical insulation; iv) exposing a ring electrode at the end of tip [133]. The scheme of this type of SECM/OM tip is showed in Fig. 1.13.

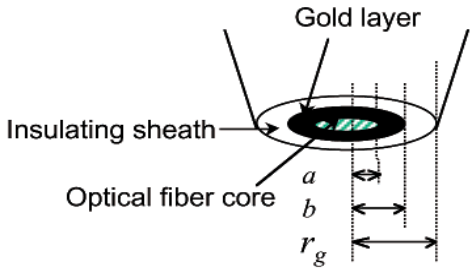

Figure 1.13 Schematic diagram of the tip for SECM – OM coupling: a) inner radii; b) outer radii; c) outermost radii including the insulating sheath (r_g)

The resolution of the SECM images of the sample topography can be enhanced if the tip-substrate separation distance is controlled by the shear force feedback, which allows an efficient approach to a very close distance to the substrate[134].

V. 2. *SECM coupled to SPR*

A different approach where a sensitive optical technique is combined with SECM was developed by *Szunerits et al.*[135]. The SECM was used as a 'writing' tool, serving to form a DNA array, by local deposition of polypyrole-ODN (oligonucleotide) samples onto SPR gold substrates. Then, the SPR-i (imaging) is applied as a "reading" tool to detect changes in the thickness or in the refractive index close to the gold substrate that result in changes in the intensity of the reflected light beam as in Fig.1.14. This allows to confirm the efficiency of the deposition step.

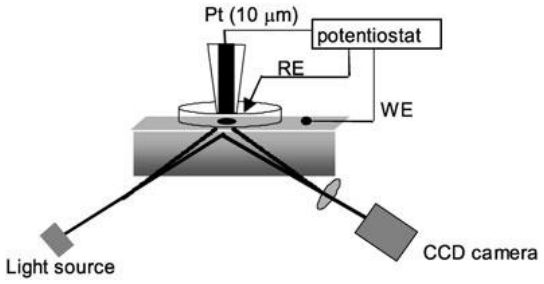

Figure 1.14 Schematic diagram of SECM and SPR-i configuration : RE-reference electrode, WE-working electrode

One important advantage of using SECM is that for a single surface different DNA probes can be patterned. SPR technique has shown its high sensitive capabilities in the detection of very low quantities of biomacromolecular adsorbates[136-138].

As SPR is very sensitive to the refractive index of the medium in the close vicinity of the metal film, the adsorption of a very small amount of adsorbate or small changes in orientation/conformation can be detected. The coupling of SECM with SPR was thus applied for observing ferrocenylalkanethiol SAM thickness variation and for monitoring the cytochrome *c* conformational changes [139]. Compared to EC-SPR, the SECM has the advantage of avoiding the application of the potential on the entire SPR substrate, which could introduce some interferences and perturb the SPR measurements.

References

1. Grieshaber, D., et al., *Electrochemical biosensors - Sensor principles and architectures*. Sensors, 2008. **8**(3): p. 1400-1458.
2. Soni, G.V., et al., *Synchronous optical and electrical detection of biomolecules traversing through solid-state nanopores*. Review of Scientific Instruments, 2010. **81**(1).
3. Narayanaswamy, R., Wolfbeis, O., *Optical Sensors*. 2004. **1**.
4. Velasco-Garcia, M.N., *Optical biosensors for probing at the cellular level: A review of recent progress and future prospects*. Seminars in Cell & Developmental Biology, 2009. **20**(1): p. 27-33.
5. Weiss, S., *Fluorescence spectroscopy of single biomolecules*. Science, 1999. **283**(5408): p. 1676-1683.
6. Zhuang, X.W., et al., *A single-molecule study of RNA catalysis and folding*. Science, 2000. **288**(5473): p. 2048-+.
7. Moerner, W.E., *Single-molecule chemistry and biology special feature: New directions in single-molecule imaging and analysis (vol 104, pg 12596, 2007)*. Proceedings of the National Academy of Sciences of the United States of America, 2007. **104**(39): p. 15584-15584.
8. Cox, W.G. and V.L. Singer, *Fluorescent DNA hybridization probe preparation using amine modification and reactive dye coupling*. Biotechniques, 2004. **36**(1): p. 114-+.
9. Ozkumur, E., et al., *Label-free and dynamic detection of biomolecular interactions for high-throughput microarray applications*. Proceedings of the National Academy of Sciences of the United States of America, 2008. **105**(23): p. 7988-7992.
10. Ozkumur, E., et al., *Spectral Reflectance Imaging for a Multiplexed, High-Throughput, Label-Free, and Dynamic Biosensing Platform*. Ieee Journal of Selected Topics in Quantum Electronics, 2010. **16**(3): p. 635-646.
11. Liedberg, B., C. Nylander, and I. Lundstrom, *Surface-Plasmon Resonance for Gas-Detection and Biosensing*. Sensors and Actuators, 1983. **4**(2): p. 299-304.
12. Manuel, M., et al., *Determination of Probable Alcohol Yield in Musts by Means of an Spr Optical Sensor*. Sensors and Actuators B-Chemical, 1993. **11**(1-3): p. 455-459.
13. Dostalek, J., et al., *Surface plasmon resonance biosensor based on integrated optical waveguide*. Sensors and Actuators B-Chemical, 2001. **76**(1-3): p. 8-12.
14. Mouvet, C., et al., *Determination of simazine in water samples by waveguide surface plasmon resonance*. Analytica Chimica Acta, 1997. **338**(1-2): p. 109-117.
15. Matsubara, K., S. Kawata, and S. Minami, *Optical Chemical Sensor Based on Surface-Plasmon Measurement*. Applied Optics, 1988. **27**(6): p. 1160-1163.
16. Liedberg, B., I. Lundstrom, and E. Stenberg, *Principles of Biosensing with an Extended Coupling Matrix and Surface-Plasmon Resonance*. Sensors and Actuators B-Chemical, 1993. **11**(1-3): p. 63-72.
17. Sharma, A.K., R. Jha, and B.D. Gupta, *Fiber-optic sensors based on surface plasmon resonance: A comprehensive review*. Ieee Sensors Journal, 2007. **7**(7-8): p. 1118-1129.
18. Yu, F., et al., *Surface plasmon enhanced diffraction for label-free biosensing*. Analytical Chemistry, 2004. **76**(13): p. 3530-3535.
19. Alleyne, C.J., et al., *Enhanced SPR sensitivity using periodic metallic structures*. Optics Express, 2007. **15**(13): p. 8163-8169.
20. Fan, X.D., et al., *Sensitive optical biosensors for unlabeled targets: A review*. Analytica Chimica Acta, 2008. **620**(1-2): p. 8-26.
21. Nenninger, G.G., et al., *Long-range surface plasmons for high-resolution surface plasmon resonance sensors*. Sensors and Actuators B-Chemical, 2001. **74**(1-3): p. 145-151.

22. Hastings, J.T., et al., *Optimal self-referenced sensing using long- and short-range surface plasmons*. Optics Express, 2007. **15**(26): p. 17661-17672.
23. Slavik, R. and J. Homola, *Ultrahigh resolution long range surface plasmon-based sensor*. Sensors and Actuators B-Chemical, 2007. **123**(1): p. 10-12.
24. Blanco, F.J., et al., *Microfluidic-optical integrated CMOS compatible devices for label-free biochemical sensing*. Journal of Micromechanics and Microengineering, 2006. **16**(5): p. 1006-1016.
25. Ymeti, A., et al., *Development of a multichannel integrated interferometer immunosensor*. Sensors and Actuators B-Chemical, 2002. **83**(1-3): p. 1-7.
26. Kinning T and Edwards P, *The resonant mirror optical biosensor*. Optical biosensors. Present and future, ed. Ligler F and Taitt C2002: Elsevier.
27. Cush, R., et al., *The Resonant Mirror - a Novel Optical Biosensor for Direct Sensing of Biomolecular Interactions .1. Principle of Operation and Associated Instrumentation*. Biosensors & Bioelectronics, 1993. **8**(7-8): p. 347-353.
28. Serpenguzel, A., S. Arnold, and G. Griffel, *Excitation of Resonances of Microspheres on an Optical-Fiber*. Optics Letters, 1995. **20**(7): p. 654-656.
29. Vollmer, F., et al., *Protein detection by optical shift of a resonant microcavity*. Applied Physics Letters, 2002. **80**(21): p. 4057-4059.
30. Sun, Y.Z. and X.D. Fan, *Optical ring resonators for biochemical and chemical sensing*. Analytical and Bioanalytical Chemistry, 2011. **399**(1): p. 205-211.
31. Iqbal, M., et al., *Label-Free Biosensor Arrays Based on Silicon Ring Resonators and High-Speed Optical Scanning Instrumentation*. Ieee Journal of Selected Topics in Quantum Electronics, 2010. **16**(3): p. 654-661.
32. Hill, K.O. and G. Meltz, *Fiber Bragg grating technology fundamentals and overview*. Journal of Lightwave Technology, 1997. **15**(8): p. 1263-1276.
33. Chen, X.F., et al., *Dual-peak long-period fiber gratings with enhanced refractive index sensitivity by finely tailored mode dispersion that uses the light cladding etching technique*. Applied Optics, 2007. **46**(4): p. 451-455.
34. R. M. A. Azzam , N.M.B., *Ellipsometry and Polarized Light* 1977, North-Holland, Amsterdam.
35. Sugimoto, K. and S. Matsuda, *Analysis of Passive Films on Austeno-Ferritic Stainless-Steel by Microscopic Ellipsometry*. Journal of the Electrochemical Society, 1983. **130**(12): p. 2323-2329.
36. Fujiwara, H., *Spectroscopic Ellipsometry:Principles and Applications*2007: Wiley.
37. Palik, E.D., *Handbook of Optical Constants of Solids*1985, New York: Academic Press.
38. Palik, E.D., *Handbook of Optical Constants of Solids II*1991, New York: Academic Press.
39. Korte, E.H. and A. Roseler, *Infrared spectroscopic ellipsometry: a tool for characterizing nanometer layers*. Analyst, 1998. **123**(4): p. 647-651.
40. Paneva, A. and I. Ohlidal, *Multiple Angle of Incidence Ellipsometric Analysis of Nonabsorbing 2-Layer and 3-Layer Systems*. Thin Solid Films, 1986. **145**(1): p. 23-37.
41. Colard, S. and M. Mihailovic, *Characterization of inhomogeneous films by multiple-angle ellipsometry*. Thin Solid Films, 1998. **336**(1-2): p. 362-365.
42. Jenkins, T.E., *Multiple-angle-of-incidence ellipsometry*. Journal of Physics D-Applied Physics, 1999. **32**(9): p. R45-R56.
43. Adzic, R., *Electrocatalysis on Surfaces Modified by Metal Monolayers Deposited at Underpotentials*, in *Encyclopedia of Electrochemistry*, Wiley-VCH, Editor 2007.
44. Wang, J., *Electrochemical glucose biosensors*. Chemical Reviews, 2008. **108**(2): p. 814-825.
45. Wang, J., *Carbon-nanotube based electrochemical biosensors: A review*. Electroanalysis, 2005. **17**(1): p. 7-14.

46. Desmet, D.J. and J.L. Ord, *OPTICAL ANISOTROPY AND ELECTROSTRICTION IN THE ANODIC OXIDE OF MOLYBDENUM*. Journal of the Electrochemical Society, 1983. **130**(2): p. 280-284.
47. D. Michell, D.A.J.R., R. Woods, *Analysis of the anodic oxygen layer on iridium by X-ray emission, electron diffraction and electron microscopy* J. Electroanal. Chem, 1977. **84**: p. 117.
48. Mykhaylyk, T.A., et al., *Comparative characterisation by atomic force microscopy and ellipsometry of soft and solid thin films*. Surface and Interface Analysis, 2007. **39**(7): p. 575-581.
49. Han, S.Y., et al., *Interfacial adsorption of cationic peptide amphiphiles: a combined study of in situ spectroscopic ellipsometry and liquid AFM*. Soft Matter, 2012. **8**(3): p. 645-652.
50. Stein, N., et al., *In-situ ellipsometric study of copper passivation by copper heptanoate through electrochemical oxidation*. Electrochimica Acta, 1998. **43**(21-22): p. 3227-3234.
51. Giskeodegard, N., et al., *In situ ellipsometric and electrochemical characterisation of oxide formed on aluminium in acetate buffer*. Physica Status Solidi C - Conferences and Critical Reviews, Vol 2 , No 12, 2005. **2**(12): p. 3953-3957.
52. Stein, N., et al., *In situ spectroscopic ellipsometric study of porous alumina film dissolution*. Electrochimica Acta, 2002. **47**(11): p. 1811-1817.
53. Haberska, K. and T. Ruzgas, *Polymer multilayer film formation studied by in situ ellipsometry and electrochemistry*. Bioelectrochemistry, 2009. **76**(1-2): p. 153-161.
54. Harris, J.J. and M.L. Bruening, *Electrochemical and in situ ellipsometric investigation of the permeability and stability of layered polyelectrolyte films*. Langmuir, 2000. **16**(4): p. 2006-2013.
55. Gottesfeld, S., *Electroanalytical Chemistry*. Vol. 15. 1989: MARCEL DEKKER.
56. Rishpon, J., et al., *Simultaneous Ellipsometric and Microgravimetric Measurements during the Electrochemical Growth of Polyaniline*. Journal of Electroanalytical Chemistry, 1990. **294**(1-2): p. 73-85.
57. Broch, L., et al., *Real time in situ ellipsometric and gravimetric monitoring for electrochemistry experiments*. The Review of scientific instruments, 2007. **78**(6): p. 064101.
58. Rodenhausen, K.B., et al., *In-situ monitoring of alkanethiol self-assembled monolayer chemisorption with combined spectroscopic ellipsometry and quartz crystal microbalance techniques*. Thin Solid Films, 2011. **519**(9): p. 2817-2820.
59. Kang, X.F., G.J. Cheng, and S.J. Dong, *A novel electrochemical SPR biosensor*. Electrochemistry Communications, 2001. **3**(9): p. 489-493.
60. Baba, A., et al., *Electropolymerization and doping/dedoping properties of polyaniline thin films as studied by electrochemical-surface plasmon spectroscopy and by the quartz crystal microbalance*. Journal of Electroanalytical Chemistry, 2004. **562**(1): p. 95-103.
61. Badia, A., et al., *Probing the electrochemical deposition and/or desorption of self-assembled and electropolymerizable organic thin films by surface plasmon spectroscopy and atomic force microscopy*. Sensors and Actuators B-Chemical, 1999. **54**(1-2): p. 145-165.
62. Baba, A., et al., *Electrochemical Surface Plasmon Resonance and Field-Enhanced Light Scattering: Monomer Copolymerization with a Polysiloxane-Conjugated Polythiophene Network Precursor*. Macromolecular Chemistry and Physics, 2010. **211**(24): p. 2624-2635.
63. Bakker, E., *Electrochemical sensors*. Analytical Chemistry, 2004. **76**(12): p. 3285-3298.
64. Dong, H., et al., *Sensitive amperometric immunosensing using polypyrrolepropylic acid films for biomolecule immobilization*. Analytical Chemistry, 2006. **78**(21): p. 7424-7431.

65. Sriwichai, S., et al., *Electrochemically controlled surface plasmon resonance immunosensor for the detection of human immunoglobulin G on poly(3-aminobenzoic acid) ultrathin films*. Sensors and Actuators B-Chemical, 2010. **147**(1): p. 322-329.
66. Dong, H., et al., *An in situ electrochemical surface plasmon resonance immunosensor with polypyrrole propylic acid film: Comparison between SPR and electrochemical responses from polymer formation to protein immunosensing*. Biosensors & Bioelectronics, 2008. **23**(7): p. 1055-1062.
67. Raitman, O.A., et al., *Integration of polyaniline/poly(acrylic acid) films and redox enzymes on electrode supports: An in situ electrochemical/surface plasmon resonance study of the bioelectrocatalyzed oxidation of glucose or lactate in the integrated bioelectrocatalytic systems*. Journal of the American Chemical Society, 2002. **124**(22): p. 6487-6496.
68. Baba, A., et al., *Electrochemical Surface Plasmon Resonance and Waveguide-Enhanced Glucose Biosensing with N-Alkylaminated Polypyrrole/Glucose Oxidase Multilayers*. Acs Applied Materials & Interfaces, 2010. **2**(8): p. 2347-2354.
69. Wang, J.L., et al., *Electrochemical surface plasmon resonance detection of enzymatic reaction in bilayer lipid*. Talanta, 2008. **75**(3): p. 666-670.
70. Erman, M. and J.B. Theeten, *Spatially Resolved Ellipsometry*. Journal of Applied Physics, 1986. **60**(3): p. 859-873.
71. Neumaier, K.R., et al., *Ellipsometric microscopy*. Europhysics Letters, 2000. **49**(1): p. 14-19.
72. Asinovski, L., D. Beaglehole, and M.T. Clarkson, *Imaging ellipsometry: quantitative analysis*. Physica Status Solidi a-Applications and Materials Science, 2008. **205**(4): p. 764-771.
73. Beaglehole, D., *PERFORMANCE OF A MICROSCOPIC IMAGING ELLIPSOMETER*. Review of Scientific Instruments, 1988. **59**(12): p. 2557-2559.
74. S. Hénon, J.M., *Microscope at the Brewster angle: Direct observation of first-order phase transitions in monolayers*. Review of Scientific Instruments, 1990. **62**(4): p. 936.
75. Cohn, R.F., J.W. Wagner, and J. Kruger, *Dynamic imaging microellipsometry: theory, system design, and feasibility demonstration*. Appl. Opt., 1988. **27**(22): p. 4664-4671.
76. Pak, H.K. and B.M. Law, *2D imaging ellipsometric microscope*. Review of Scientific Instruments, 1995. **66**(10): p. 4972-4976.
77. Linke, F. and R. Merkel, *Quantitative ellipsometric microscopy at the silicon-air interface*. Review of Scientific Instruments, 2005. **76**(6).
78. Linke, F. and R. Merkel, *Quantitative ellipsometric microscopy at the glass–water interface*. New Journal of Physics, 2005. **7**(1): p. 128.
79. Yu, Y. and G. Jin, *Influence of electrostatic interaction on fibrinogen adsorption on gold studied by imaging ellipsometry combined with electrochemical methods*. Journal of Colloid and Interface Science, 2005. **283**(2): p. 477-481.
80. Foley, K.J., X. Shan, and N.J. Tao, *Surface impedance imaging technique*. Analytical Chemistry, 2008. **80**(13): p. 5146-5151.
81. Kotz, R., D.M. Kolb, and J.K. Sass, *ELECTRON-DENSITY EFFECTS IN SURFACE-PLASMON EXCITATION ON SILVER AND GOLD ELECTRODES*. Surface Science, 1977. **69**(1): p. 359-364.
82. Shan, X.N., et al., *Imaging Local Electrochemical Current via Surface Plasmon Resonance*. Science, 2010. **327**(5971): p. 1363-1366.
83. Barker, A.L., et al., *Scanning electrochemical microscopy (SECM) as a probe of transfer processes in two-phase systems: Theory and experimental applications of SECM-induced transfer with arbitrary partition coefficients, diffusion coefficients, and interfacial kinetics*. Journal of Physical Chemistry B, 1998. **102**(9): p. 1586-1598.

84. Bard, A.J., et al., *SCANNING ELECTROCHEMICAL MICROSCOPY - INTRODUCTION AND PRINCIPLES*. Analytical Chemistry, 1989. **61**(2): p. 132-138.
85. Kwak, J. and A.J. Bard, *SCANNING ELECTROCHEMICAL MICROSCOPY - THEORY OF THE FEEDBACK MODE*. Analytical Chemistry, 1989. **61**(11): p. 1221-1227.
86. Kwak, J. and A.J. Bard, *SCANNING ELECTROCHEMICAL MICROSCOPY - APPARATUS AND TWO-DIMENSIONAL SCANS OF CONDUCTIVE AND INSULATING SUBSTRATES*. Analytical Chemistry, 1989. **61**(17): p. 1794-1799.
87. Lefrou, C. and R. Cornut, *Analytical Expressions for Quantitative Scanning Electrochemical Microscopy (SECM)*. Chemphyschem, 2010. **11**(3): p. 547-556.
88. Bard, A.J., M.V. Mirkin, *Scanning Electrochemical Microscopy*2001, New York: Marcel Dekker.
89. Sun, P., F.O. Laforge, and M.V. Mirkin, *Scanning electrochemical microscopy in the 21st century*. Physical Chemistry Chemical Physics, 2007. **9**(7): p. 802-823.
90. Mirkin, M.V., et al., *Scanning electrochemical microscopy in the 21st century. Update 1: five years after*. Physical Chemistry Chemical Physics, 2011. **13**(48): p. 21196-21212.
91. Wittstock, G., et al., *Scanning electrochemical microscopy for direct imaging of reaction rates*. Angewandte Chemie-International Edition, 2007. **46**(10): p. 1584-1617.
92. Bergner, S., et al., *High-Resolution Imaging of Nanostructured Si/SiO2 Substrates and Cell Monolayers Using Scanning Electrochemical Microscopy*. Electroanalysis, 2011. **23**(1): p. 196-200.
93. Takahashi, Y., et al., *Transfected Single-Cell Imaging by Scanning Electrochemical Optical Microscopy with Shear Force Feedback Regulation*. Analytical Chemistry, 2009. **81**(23): p. 9674-9681.
94. Binnig, G., C.F. Quate, and C. Gerber, *Atomic Force Microscope*. Physical Review Letters, 1986. **56**(9): p. 930-933.
95. Allongue, P., V. Kieling, and H. Gerischer, *ETCHING MECHANISM AND ATOMIC-STRUCTURE OF H-SI(111) SURFACES PREPARED IN NH4F*. Electrochimica Acta, 1995. **40**(10): p. 1353-1360.
96. Allongue, P., V. Costakieling, and H. Gerischer, *ETCHING OF SILICON IN NAOH SOLUTIONS .1. INSITU SCANNING TUNNELING MICROSCOPIC INVESTIGATION OF N-SI(111)*. Journal of the Electrochemical Society, 1993. **140**(4): p. 1009-1018.
97. Allongue, P., H. Brune, and H. Gerischer, *INSITU STM OBSERVATIONS OF THE ETCHING OF N-SI(111) IN NAOH SOLUTIONS*. Surface Science, 1992. **275**(3): p. 414-423.
98. Damian, A., F. Maroun, and P. Allongue, *Selective Growth and Dissolution of Ni on a PdAu Bimetallic Surface by In Situ STM: Determining the Relative Adsorbate-Substrate Interaction Energy*. Physical Review Letters, 2009. **102**(19).
99. Damian, A., F. Maroun, and P. Allongue, *Electrochemical growth and dissolution of Ni on bimetallic Pd/Au(111) substrates*. Electrochimica Acta, 2010. **55**(27): p. 8087-8099.
100. Liu, S.Y. and Y.F. Wang, *Application of AFM in Microbiology: A Review*. Scanning, 2010. **32**(2): p. 61-73.
101. Magonov, S.N. and D.H. Reneker, *Characterization of polymer surfaces with atomic force microscopy*. Annual Review of Materials Science, 1997. **27**: p. 175-222.
102. Zhong, Q., et al., *FRACTURED POLYMER SILICA FIBER SURFACE STUDIED BY TAPPING MODE ATOMIC-FORCE MICROSCOPY*. Surface Science, 1993. **290**(1-2): p. L688-L692.
103. Albrecht, T.R., et al., *IMAGING AND MODIFICATION OF POLYMERS BY SCANNING TUNNELING AND ATOMIC FORCE MICROSCOPY*. Journal of Applied Physics, 1988. **64**(3): p. 1178-1184.
104. Itaya, K. and E. Tomita, *SCANNING TUNNELING MICROSCOPE FOR ELECTROCHEMISTRY - A NEW CONCEPT FOR THE INSITU SCANNING*

TUNNELING MICROSCOPE IN ELECTROLYTE-SOLUTIONS. Surface Science, 1988. **201**(3): p. L507-L512.
105. Green, M.P., et al., *Insitu Scanning Tunneling Microscopy Studies of the Underpotential Deposition of Lead on Au(111)*. Journal of Physical Chemistry, 1989. **93**(6): p. 2181-2184.
106. Magnussen, O.M., et al., *Atomic-Structure of Cu Adlayers on Au(100) and Au(111) Electrodes Observed by Insitu Scanning Tunneling Microscopy*. Physical Review Letters, 1990. **64**(24): p. 2929-2932.
107. Hachiya, T., H. Honbo, and K. Itaya, *Detailed Underpotential Deposition of Copper on Gold(111) in Aqueous-Solutions*. Journal of Electroanalytical Chemistry, 1991. **315**(1-2): p. 275-291.
108. Tao, N.J., et al., *Initial-Stage of Underpotential Deposition of Pb on Reconstructed and Unreconstructed Au(111)*. Surface Science, 1992. **271**(1-2): p. L338-L344.
109. Yau, S.L., C.M. Vitus, and B.C. Schardt, *Insitu Scanning Tunneling Microscopy of Adsorbates on Electrode Surfaces - Images of the (Square-Root 3 X Square Root3)R30-Degrees-Iodine Adlattice on Platinum(111)*. Journal of the American Chemical Society, 1990. **112**(9): p. 3677-3679.
110. Mccarley, R.L. and A.J. Bard, *Scanning Tunneling Microscopy Studies of Iodide Adsorption on Au(111) - Direct Observation of Adlattice Orientation*. Journal of Physical Chemistry, 1991. **95**(24): p. 9618-9620.
111. Tao, N.J. and S.M. Lindsay, *Insitu Scanning Tunneling Microscopy Study of Iodine and Bromine Adsorption on Au(111) under Potential Control*. Journal of Physical Chemistry, 1992. **96**(13): p. 5213-5217.
112. Gao, X.P., Y. Zhang, and M.J. Weaver, *Observing Surface Chemical-Transformations by Atomic-Resolution Scanning Tunneling Microscopy - Sulfide Electrooxidation on Au(111)*. Journal of Physical Chemistry, 1992. **96**(11): p. 4156-4159.
113. Trevor, D.J., C.E.D. Chidsey, and D.N. Loiacono, *Insitu Scanning-Tunneling-Microscope Observation of Roughening, Annealing, and Dissolution of Gold(111) in an Electrochemical-Cell*. Physical Review Letters, 1989. **62**(8): p. 929-932.
114. Wiechers, J., et al., *An Insitu Scanning Tunneling Microscopy Study of Au(111) with Atomic Scale Resolution*. Journal of Electroanalytical Chemistry, 1988. **248**(2): p. 451-460.
115. Gao, X.P., A. Hamelin, and M.J. Weaver, *Reconstruction at Ordered Au(110)-Aqueous Interfaces as Probed by Atomic-Resolution Scanning Tunneling Microscopy*. Physical Review B, 1991. **44**(19): p. 10983-10986.
116. Tao, N.J. and S.M. Lindsay, *Observations of the 22xsquare-Root-3 Reconstruction of Au(111) under Aqueous-Solutions Using Scanning Tunneling Microscopy*. Journal of Applied Physics, 1991. **70**(9): p. 5141-5143.
117. Tao, N.J., J.A. Derose, and S.M. Lindsay, *Self-Assembly of Molecular Superstructures Studied by Insitu Scanning Tunneling Microscopy - DNA Bases on Au(111)*. Journal of Physical Chemistry, 1993. **97**(4): p. 910-919.
118. Lindsay, S.M. and B. Barris, *Imaging Deoxyribose Nucleic-Acid Molecules on a Metal-Surface under Water by Scanning Tunneling Microscopy*. Journal of Vacuum Science & Technology a-Vacuum Surfaces and Films, 1988. **6**(2): p. 544-547.
119. Tao, N.J. and Z. Shi, *Real-Time Stm Afm Study of Electron-Transfer Reactions of an Organic-Molecule - Xanthine at the Graphite Water Interface*. Surface Science, 1994. **321**(1-2): p. L149-L156.
120. Tao, N.J. and Z. Shi, *Kinetics of Oxidation of Guanine Monolayers at the Graphite-Water Interface Studied by Afm/Stm*. Journal of Physical Chemistry, 1994. **98**(31): p. 7422-7426.
121. Tao, N.J., C.Z. Li, and H.X. He, *Scanning tunneling microscopy applications in electrochemistry - beyond imaging*. Journal of Electroanalytical Chemistry, 2000. **492**(2): p. 81-93.

122. Bard, A.J., et al., *CHEMICAL IMAGING OF SURFACES WITH THE SCANNING ELECTROCHEMICAL MICROSCOPE*. Science, 1991. **254**(5028): p. 68-74.
123. Macpherson, J.V., et al., *Quantitative spatially resolved measurements of mass transfer through laryngeal cartilage*. Biophysical Journal, 1997. **73**(5): p. 2771-2781.
124. Gonsalves, M., et al., *Scanning electrochemical microscopy as a local probe of oxygen permeability in cartilage*. Biophysical Journal, 2000. **78**(3): p. 1578-1588.
125. Macpherson, J.V. and P.R. Unwin, *Combined scanning electrochemical-atomic force microscopy*. Analytical Chemistry, 2000. **72**(2): p. 276-285.
126. Kueng, A., et al., *Combined scanning electrochemical atomic force microscopy for tapping mode imaging*. Applied Physics Letters, 2003. **82**(10): p. 1592-1594.
127. Fasching, R.J., Y. Tao, and F.B. Prinz, *Cantilever tip probe arrays for simultaneous SECM and AFM analysis*. Sensors and Actuators B-Chemical, 2005. **108**(1-2): p. 964-972.
128. Konig, M., et al., *Time-Resolved Single Molecule Microscopy coupled with Atomic Force Microscopy*, in *Three-Dimensional and Multidimensional Microscopy: Image Acquisition and Processing Xix*, J.A. Conchello, et al., Editors. 2012, Spie-Int Soc Optical Engineering: Bellingham.
129. Kassies, R., et al., *Combined AFM and confocal fluorescence microscope for applications in bio-nanotechnology*. Journal of Microscopy-Oxford, 2005. **217**: p. 109-116.
130. Madl, J., et al., *A combined optical and atomic force microscope for live cell investigations*. Ultramicroscopy, 2006. **106**(8-9): p. 645-651.
131. Drews, D., et al., *Nanostructured probes for scanning near-field optical microscopy*. Nanotechnology, 1999. **10**(1): p. 61-64.
132. Abraham, M., et al., *Micromachined aperture probe tip for multifunctional scanning probe microscopy*. Ultramicroscopy, 1998. **71**(1-4): p. 93-98.
133. Lee, Y. and A.J. Bard, *Fabrication and characterization of probes for combined scanning electrochemical/optical microscopy experiments*. Analytical Chemistry, 2002. **74**(15): p. 3626-3633.
134. Lee, Y., Z.F. Ding, and A.J. Bard, *Combined scanning electrochemical/optical microscopy with shear force and current feedback*. Analytical Chemistry, 2002. **74**(15): p. 3634-3643.
135. Fortin, E., et al., *Micro-imprinting of oligonucleotides and oligonucleotide gradients on gold surfaces: A new approach based on the combination of scanning electrochemical microscopy and surface plasmon resonance imaging (SECM/SPR-i)*. Electroanalysis, 2005. **17**(5-6): p. 495-503.
136. Piscevic, D., et al., *OLIGONUCLEOTIDE HYBRIDIZATION OBSERVED BY SURFACE-PLASMON OPTICAL TECHNIQUES*. Applied Surface Science, 1995. **90**(4): p. 425-436.
137. Nelson, B.P., et al., *Surface plasmon resonance imaging measurements of DNA and RNA hybridization adsorption onto DNA microarrays*. Analytical Chemistry, 2001. **73**(1): p. 1-7.
138. Goodrich, T.T., H.J. Lee, and R.M. Corn, *Direct detection of genomic DNA by enzymatically amplified SPR imaging measurements of RNA microarrays*. Journal of the American Chemical Society, 2004. **126**(13): p. 4086-4087.
139. Xiang, J., J. Guo, and F.M. Zhou, *Scanning electrochemical microscopy combined with surface plasmon resonance: Studies of localized film thickness variations and molecular conformation changes*. Analytical Chemistry, 2006. **78**(5): p. 1418-1424.

Chapter 2 :Sensing the chemical reactivity of surfaces by light reflectivity at macro and microscale. Application to the electrografting of diazonium salts

I. *Introduction*

The work presented here is a part of a larger project whose purpose is to build a simple and efficient configuration capable of imaging and studying surface chemical reactions. This feature is intended to be further applied to the electro-optical detection of surface reactions at micromechanical sensing platforms, typically microcantilevers, by detection of mechanical changes associated to electrochemical activation or chemical modification at their surface.

The principle of this approach relies on the coupling of existing optical microscopic imaging techniques with micro-electrochemical techniques in order to image and investigate in-situ and in real-time micro-electrochemical surface processes. This coupling can bring new insights to improve the understanding of different mechanistic issues.

In order to reach the sensing potential of our proposed setup, initial researches have been carried out as prerequisite for the validation of the concept. In this chapter, I will discuss about the selection of a very simple optical technique based on light reflectivity measurements. It is illustrated in the case of the electrochemically activated grafting of surfaces by diazonium salts.

The area of optical microscopes is very well developed in different configurations allowing optical imaging with a lateral resolution of the order of a fraction of micrometer. However, the most widely used optical technique is surface plasmon resonance (SPR). As described in chapter 1, SPR is a very powerful label-free tool to study the interactions between a target and a biorecognition molecule, by measuring the change in local refractive index near a gold surface. Thus, it can be adapted to perform label-free molecular interactions assays with low detection limits in microsystems [1-3]. Even if it is widely used, for some specific applications, the experimental configuration of the SPR technique is difficult to carry out.

These limitations are: (i) use of gold plated substrates and high-quality optical prisms, (ii) optimal detection of a solute only in the close proximity of the gold surface (within nanometers, where the evanescent field is forming), and (iii) inherent incompatibility with microfluidic systems.

We propose to evidence structural changes at substrate generated by an electrochemical transformation using optical imaging techniques such as reflectivity and ellipsometry. In this way, in-situ coupled optical and electrochemical characterizations of surface transformation processes at the micrometer scale can be achieved. The model system we have studied with our setup involves the electrografting of electrodes by the reduction of diazonium salts. This system has proved large interest since the last two decades, and is widely used for various applications as biomedicine, microelectronics, protection against corrosion, and fabrication of printing inks. The success of diazonium chemistry for surface chemical functionalization resides mainly in the simple manner it forms on surfaces strongly adherent organic coatings with controlled thickness, from a monolayer to micrometer multilayers [4-6].

Figure 2.1 schematically depicts the surface modification of different materials by diazonium compounds using the electrochemical activation. Upon electron transfer, a diazonium moiety is transformed into a highly reactive radical species. This intermediate may undergo different chemical routes, which provide complex structuration of the electrode. Among them, it can react with the surface were it has been generated and bind to it. This scenario explains also the formation of multilayers by attack of a radical to an already grafted organic layer. The surface grafting can be achieved by electroreduction of an added diazonium salt or of an in-situ generated diazonium salt. Moreover, diazonium may instantaneously dissociate, allowing for chemical (spontaneous) surface grafting. For all our experiments, we will use only the direct electrografting of diazonium salts. Even if this reaction of reduction of diazonium salts has been largely studied, some mechanistic aspects of the electrografting process are not completely understood. Thus, we wish to validate the approach, which couples in situ and real-time electrochemical-optical imaging, to depict the kinetic growth of the organic coating during diazonium electrografting.

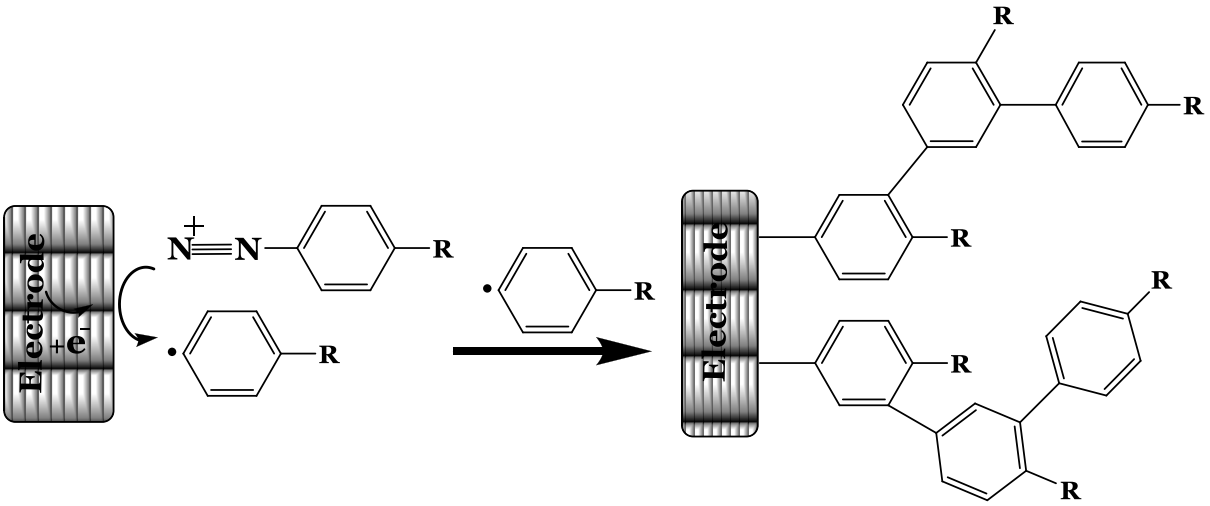

Figure 2.1 The schematic mechanism of modification of surfaces by electrochemical reduction of diazonium salts.

II. *Theoretical aspects and experimental setup of the electro-optic imaging technique*

II. 1. *Principle and optical model employed for the measurements*

The principle of the method is based on monitoring the surface reflectivity variations by simply measuring the intensity of light that has been reflected by a reflective surface illuminated by a light beam. In this way, it is necessary to have a reference reflecting surface to compare, which in some cases can be : (1) a surface of the same nature, but which will not be modified (for example, one non-connected electrode, in the case of array of electrodes), or (2) the initial unmodified state of the substrate. Thus, continuous acquisition of images allows determining the local evolution of a thin layer deposition on a reflecting surface.

The scheme of the optical model is illustrated in Fig. 2.2. The model is based on the variation of light reflectivity (R) due to deposition of an organic coating. The variation of light reflectivity (R) is directly dependent on the complex refractive indexes of the substrate (in our case, Au, $\tilde{n}_{Au}$), of the ambient medium and also on that of the deposited layer, n_F along with the deposited organic film thickness. The presented model allows quantifying the thickness of the deposited film by converting the information from the light reflectivity changes.

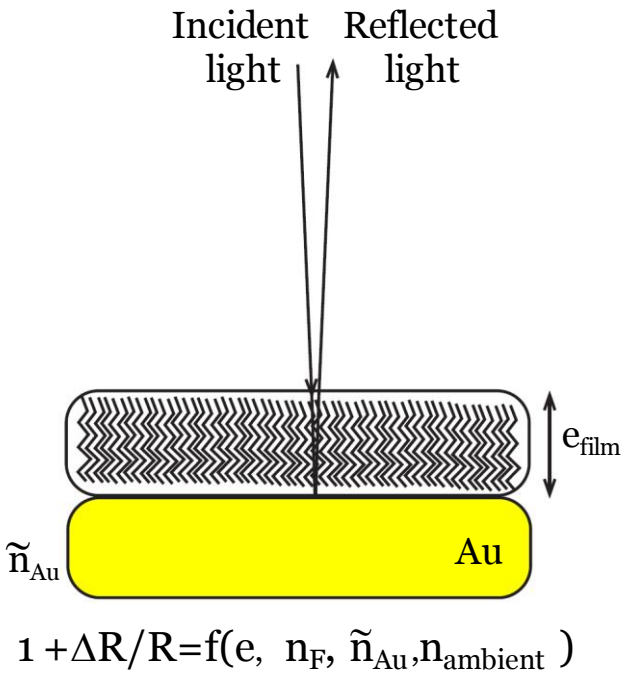

Figure 2.2 Proposed optical model used for the reflectivity variation measurement during deposition of an organic thin layer.

II. 2. *Fundamental theory of optical measurement*

During the electrografting of diazonium salts, a thin film is deposited on the electrode surface. This accumulation of material forms a layer on the electrode, with a refractive index different from that of the ambient medium where the light propagates. In this way, in the close vicinity of the electrode surface, the refractive index changes. If the electrode is a reflecting surface, when illuminated by a light source, the reflected light intensity at the deposited layer is changed. The light reflectivity is the ratio of the intensity of the reflected beam $I_{reflected}$ by the intensity of the incident beam $I_{incident}$: $R= I_{reflected}/I_{incident}$. For specific incidence angle and orientation of a polarized light, the light reflectivity of a beam propagating in an ambient medium (medium a, real index n_A) reflecting on a substrate (medium s), is given by (1). The substrate is optically characterized by a complex refractive index $\tilde{n}_s= n_s + i\ k_s$, where n_s represents the real part of refractive index, and k_s is the complex part, which is known also as the extinction coefficient.

The light reflectivity is equal to the square of the modulus of the reflection coefficient of the reflected electromagnetic wave, $\tilde{r}_{AS}$, which is a complex number and in the case of a normal incidence, such as in our setup, is obtained through Fresnel equations.

$$R_{AS} = |\tilde{r}_{AS}|^2 = \left| \frac{n_A - \tilde{n}_S}{n_A + \tilde{n}_S} \right|^2 \qquad (1)$$

When the light passes through an intermediate organic layer (with refractive index $n_F \approx 1.5$, and thickness d) intercalated between the ambient medium and the reflecting substrate, the reflection coefficients at each interface (A/F and F/S) can be expressed by relations similar to (1). The overall light reflectivity takes into consideration the multiple reflections at each interface (ambient/film described by $\tilde{r}_{AF}$ and the second one film/substrate described by $\tilde{r}_{SF}$), along with the phase shift induced by the light traversing the deposited film. The expression of light reflectivity extends to:

$$R = |\tilde{r}|^2 = \left| \frac{\tilde{r}_{AF} + \tilde{r}_{FS} e^{2i\frac{2\pi}{\lambda} n_F d}}{1 + \tilde{r}_{AF} \tilde{r}_{FS} e^{2i\frac{2\pi}{\lambda} n_F d}} \right|^2 \qquad (2)$$

If the incident light beam has a constant intensity, one can measure from recorded snapshots, the evolution of the reflected beam light intensity collected at constant time t, compared to that one recorded at time t=0, $I_{reflected}(0)$: $I_{reflected}(t)/I_{reflected}(0) = 1 + \Delta R/R$. Finally, we measure the relative variation of the collected reflected beam: $[I_{reflected}(t)-I_{incident}(0)] / I_{incident}(0)$, which is equal to the relative variation of reflectivity: $\Delta R/R$. The sensitivity of the technique is directly dependent on the optical properties of the studied surface, as reflectivity or optical indexes of the substrate. The appropriate material should be chosen with :

i) an important difference in refractive index compared to the studied deposited layer (the case of semiconductors);

ii) a steep variation of the optical index with the wavelength;

II. 3. *Choice of substrate of interest – the case of Au*

The most promising materials for our technique are the silicon and gold, and also ITO and copper. In the case of Si which has a complex refractive index with a high real part (n~ 4 and k<0.1 in the visible spectrum) in comparison with the refractive index of the deposited layer, the monitoring of the growth of thin coated film is possible with a high sensitivity (>0.1 nm). These specific properties of Si are well known, and they are already largely used for the characterization of deposited films by ellipsometric techniques. Gold is also a very promising material, mostly due to its reflectivity spectrum in the visible electromagnetic spectrum. As observed from the reflectivity spectrum presented in Figure 2.3, gold (like copper) shows a steep decrease of reflectivity in the blue-violet part of the spectrum, which explains its yellow color. This decrease is related to the important variation of the real part of its complex refractive index for λ<500 nm. Thus, contrary to the silicon, the deposition of a thin film on the gold surface - will lead to relative variations of reflectivity strongly dependent on the wavelength of the light beam, and calculus shows that the reflectivity variations are more substantial in the blue spectral region (14 times more than in the red spectral region). This phenomenon confirms that the growth of an organic layer on a gold surface can be characterized through an optical detection based on measuring variations of light reflectivity in the blue spectral region.

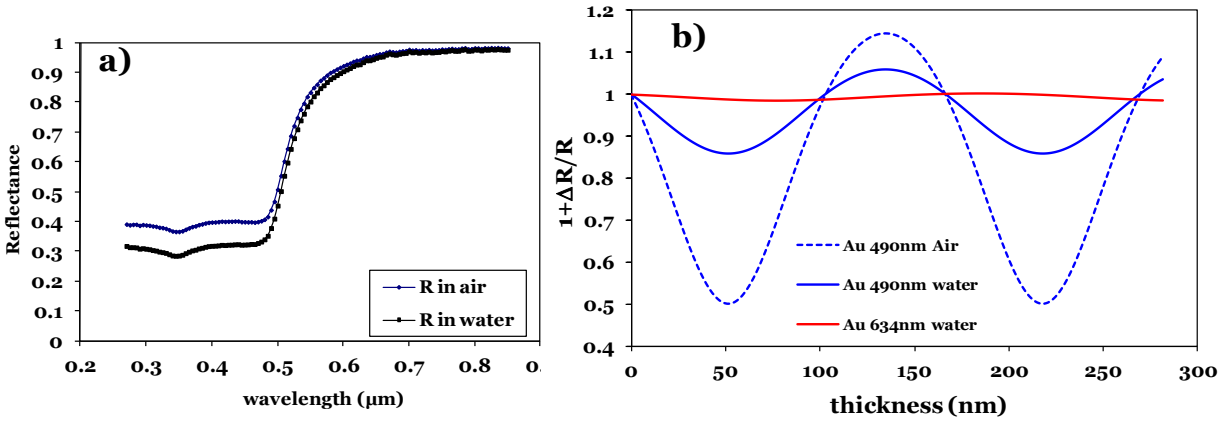

Figure 2.3 a) Reflectivity spectrum of a bare gold surface in air and water; b) Theoretical relative variations of reflectivity as function of deposited layer thickness on gold surface and wavelength of light beam (blue or red spectral regions) and optical indexes of the media where the light is propagated (air and water).

This is illustrated in figure 2.3 b) which shows for 2 specific wavelengths (blue and red) the theoretical evolution of the relative variation of light reflectivity of a gold surface covered with an homogeneous layer as a function of the thickness of the deposited film of refractive index n= 1.5, for a light beam propagating in air (n=1) or in water (n=1.33). This figure shows for example that under illumination by a blue light, the deposition of a 50 nm layer results in a 50% decrease of surface reflectivity in the air and about 15% in a water solution. While the same deposited layer is almost invisible when illuminated by a red light. This figure confirms the simplicity and the sensitivity of the proposed method based on the measurement of the relative variation of surface reflectivity for the real time and in-situ detection of the growth of a thin film on a reflecting surface.

II. 4. *Experimental configuration of the electro-optical imagery setup*

The experimental configuration of the proposed setup is very simple, if compared with the SPR one, for example. It consists only of an optical microscope equipped with a camera, which allows for the recording of the images of light intensity during the experiments. The scheme of the setup is depicted in Fig. 2.4

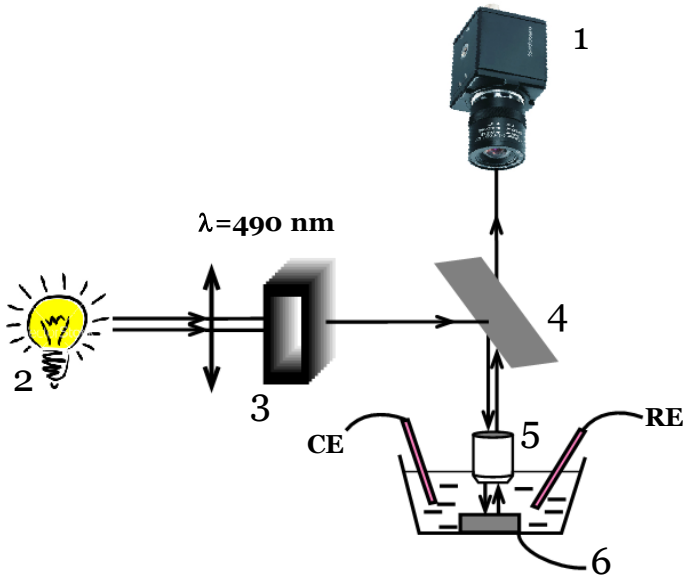

Figure 2.4 Schematic representation of the setup used for measuring relative variations of light reflectivity.

The analyzed substrate (6) is illuminated from the top at almost zero degree of incidence by a light beam with a known numerical aperture. The light beam source can be polychromatic, or as in our case for a gold substrate, monochromatic, as a higher sensitivity is obtained for a blue lightning (400nm<λ<500nm, here λ=490 nm). This specific illumination is obtained from a standard source of halogen white light(2), which passes through a spectral filter(3). The incident light beam illuminates the surface via a microscope objective (5). The microscope objective collects consequently a part of the reflected and diffused light beam from the surface, which should be positioned within the limits of the objective numerical aperture.
The collected light beam is conducted to an optical detector (a CCD or CMOS)(1), which allows imaging in real-time the light flux received by each pixel, on the analyzed surface. Thus, a clear image of the surface is obtained on the light reflectivity reading system. The separation of the incident from the reflected beam is achieved through a beam separator (4).

III. *Validation of the technique and sensitivity of measurements*

First, we have validated the opto-electrochemical microscopic device with the imaging of electrochemically-induced local surface modifications on large surfaces (gold wafer) of ≈ 1cm², prior to study in situ processes and access quantitative information at the micrometer scale. Fig. 2.5 presents the validation of the optical model used to depict reflectivity changes induced by a transparent layer immobilized on a Au reflecting surface. It consists of realizing measurements of relative reflectivity variations on substrates modified by organic films of different thicknesses obtained by electrografting from aryldiazonium salts. Here, the grafting was carried out with NBD for different times and potential activations. The thickness of nitrophenyl (NP) deposited layer was estimated with conventional ellipsometry technique. The experimental light reflectivity measurements in different environment media (ACN or air) show a good correlation between the experimental and the theoretical evolution of the reflectivity with the layer thickness.

It also shows a better sensitivity in air than a liquid system as predicted by (2) and Fig 2.3.b.

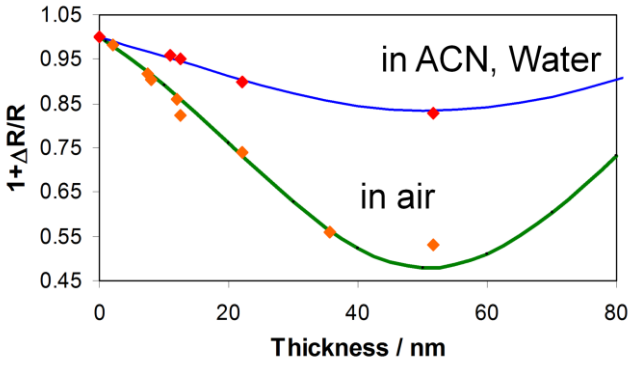

Figure 2.5 Validation of optical model for measurements of relative reflectivity variation in air, ACN and water on Au surfaces grafted with organic layers of different thicknesses (different deposited layer thicknesses measured in air (orange rectangles) and ACN and water (red rectangles).

The optical model of light reflectivity variation at the spectral wavelength λ=490 nm on a gold surface allows to calculate, for deposited layers e<30 nm, that light reflectivity decreases by 0.43 % per 1 nm of homogeneous deposited layer when measured in situ in a water or ACN solution. This value is obtained from the slope of the linear region on the variation of relative reflectivity in ACN and water (till 0.85, blue line; Fig. 2.5)

IV. Characterization of surface chemical reactivity: kinetic analysis of film deposited by electrografting of diazonium salts

To illustrate the imaging capabilities of our setup, the reflectivity measurements were carried out on different substrates, which are depicted in table 1:

	Au microdisc electrode ∅=25µm
	Au disc electrode ∅=250µm
	Au disc electrode ∅=500µm
	Micro-array Au electrode, 1mm-long, 10µm- width interspaced by 5, or by 10 µm
	Au Micro cantilever 70 µm x 20µm

Table 1 Substrates used for opto-electrochemical experiments

The electrografting of diazonium salts is illustrated by CV (cyclic voltammetry) in Fig. 2.6. Starting from a positive potential where no reaction proceeds at the electrode, the potential is swept to cathodic regions. A reduction peak appears at a threshold potential of 0.3 V vs Ag/AgCl. It is characteristic of a surface immobilization process resulting from the grafting of electrogenerated radical as in the mechanism depicted in the Fig. 2.1. As a consequence of the deposition of the organic layer, the electrode is blocked for further ET. This is confirmed by the disappearance of the reduction peak after the first cycle.

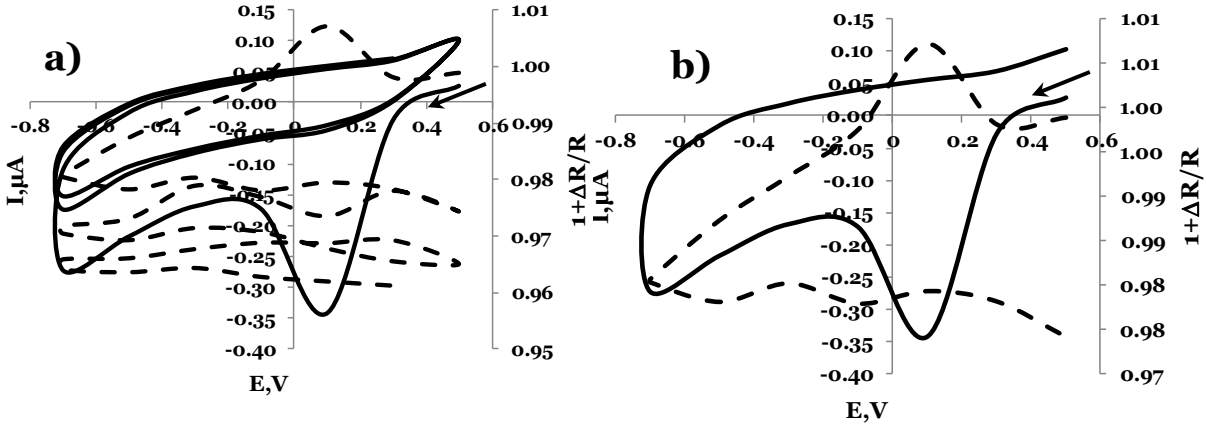

Figure 2.6 Variation of light reflectivity during the electrografting of NBD (C=5 mM) in ACN + 0.1 M NBu4BF4 on gold microelectrode (∅=250µm): a) black line : I=f(E), v=0.1 V/s; dashed black line: reflectivity during the electrografting; b)representation of the first cycle for CV and reflectivity (black line: I=f(E); dashed line: reflectivity variation.

Simultaneously with the recording of the electrode current response as a function of the applied potential, the variation of light reflectivity of the electrode surface is monitored. As can be noticed in Fig. 2.6 b), after a slight increase of reflectivity associated with the peak foot, the light reflectivity decreases by ≈2% as the peak is obtained. This ΔR/R increase is associated to charge flow and is in favor of an electro-reflectance phenomenon, along with the desorption process of spontaneously attached moieties, prior to the electrode grafting detected by the further ΔR/R decrease.

The desorption of near monolayer would correspond to a ΔR/R variation of ≈ +0.5%.

Upon further negative potential is applied, a layer is grown and its thickness corresponding to 1+ΔR/R =0.96, is higher than 8 nm. This observation proves that the deposition of the organic film is realized mostly during the first cycle of CV.

IV. 1. *Kinetics investigation on the electrografting of thin layers derived from different dizonium salts*

IV. 1. 1. Electrografting of NBD (4-nitrobenzenediazonium salt)

In the case of small electrodes such as microelectrodes (∅ =25 µm), similar quantitative information can be accessed for the deposition of thin organic layers during slow electrografting processes, for applied electrode potential E<-0.5V (Fig. 2.7).

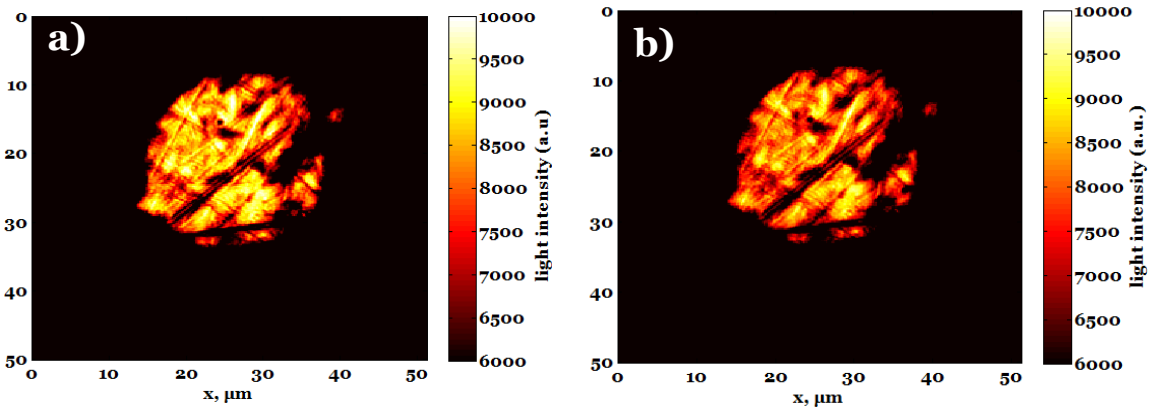

Figure 2.7 Light intensity image of a gold microelectrode (∅=25 µm) a) before grafting; b) after grafting of NBD, (C=5 mM) in ACN + 0.1 M NBu4BF4, chronoamperometry (CA) potential step from 0.2V to -0.3 V vs Ag/AgCl, for a duration of 300s.

The light intensity image of the grafted microelectrode is reported in figure 2.7 b). Compared to that recorded before grafting (Fig.2.7 a), the deposition of the organic layer is confirmed by a decrease of almost 5% in the reflected light intensity. During the electrografting of the diazonium salt, the kinetics of the microelectrode coating is also investigated by converting 1+ΔR/R variation into film thickness, as represented in Fig. 2.8, which present directly the growth of the organic layer during another electrografting experiment on the same substrate.

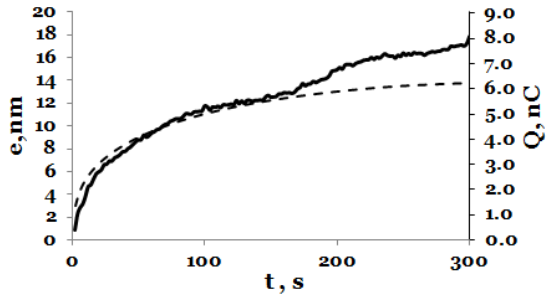

Figure 2.9 Evolution of the thickness (plain line) and charge (dashed line) for the deposition of a nitrophenyl film (NP) during a chronoamperometric potential step between 0.3 and -0.3 V vs Ag/AgCl for 300s at a gold microelectrode (∅=25 µm) of NBD (C=5 mM) in ACN + 0.1 M NBu4BF4.

The thickness evolution with time is then compared to the charge consumed that is deduced from the electrode current integration. It can be observed that till a deposition of a layer with the thickness of about 12 nm, the correlation between the deposited layer thickness and the charge consumed during the reaction is good. The proportionality between the consumed charge and the deposited layer film allows estimating the faradic yield of the electrografting reaction, **η**. The faradic yield relation is obtained from the 2nd law of Faraday:

$$\mathbf{Q = n_e * F} \qquad (3)$$

where **Q**=the consumed charge [C]; $\mathbf{n_e}$ corresponds to the number of moles of electron transferred during the grafting. Moreover light reflectivity measurement gives access to the thickness of the film deposited on the electrode, **th**. It is converted into an amount, **n**, of radical moieties immobilized on the electrode surface:

$$\mathbf{n = \rho * th * S / M} \qquad (4)$$

whith **ρ** the volumetric mass of the layer (assumed 1), **M** the molecular mass of the radical unit (M=123 g/mol for NP radical) and **S** the geometric area of the electrode surface. The comparison of **n** with $\mathbf{n_e}$ the overall number of electrons transferred yields the apparent number of electron transferred per diazonium molecule for grafting:

$$\mathbf{z = n_e / n = Q * M / (F * \rho * th * S)} \qquad (5)$$

Knowing that 1 electron is theoretically exchanged for the formation of 1 radical upon 1 diazonium molecule reduction the inverse of z gives the faradic yield of the electrografting reaction:

$$\eta(\%)=100/z \qquad (6)$$

Here, $\eta \approx 50$ %, which indicates that one radical out of two formed at the electrode is used for the growth of the deposited film, along with the fact that the growth rate of the film is limited only by the radical reaction with the surface. Similarly, the efficiency of grafting process can be characterized by the number of transferred electrons required during the diazonium electrografting for the layer growth.

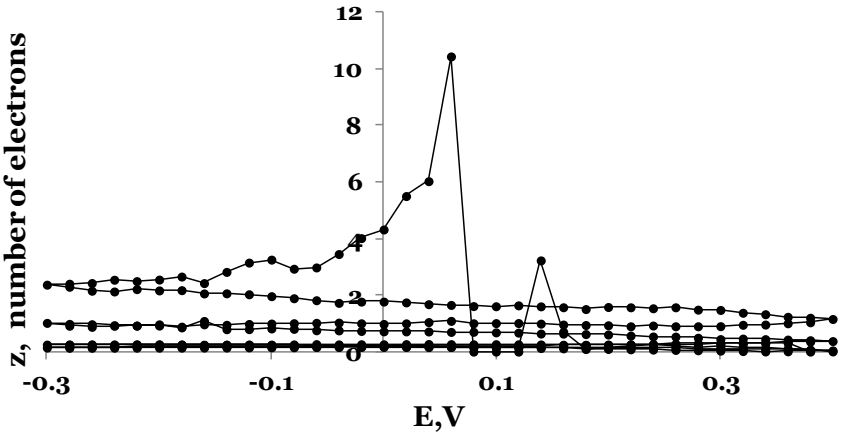

Figure 2.9 z, number of transferred electrons during the electrografting of the NBD (C=5 mM) in ACN + 0.1 M NBu4BF4, scan limits: 0.4 and -0.3V vs Ag/AgCl, v=0.01 V/s, on a gold microelectrode, ∅ =25 µm.

As observed in figure 2.9, the electrografting process is less efficient at the beginning of the first potential scan as the number of transferred electrons goes to 10. Indeed, many radicals are formed at the beginning and not all of them are grafted, but for the second cycle, **z** tends to a value between 1 and 2 transferred electrons. During the third cycle, the yield becomes very low as on the already blocked surface of the electrode, both the growth of the layer and the radical formation are slower.

IV. 1. 2. Electrografting of CBD (4-carboxybenzenediazonium salt)

We have also investigated the grafting of 4-carboxybenzenediazonium (CB) on gold electrodes, because of its potential application to functionalize organic layers. One of these applications involves the immobilization of many entities such as proteins through the peptidic coupling of the substrate prefunctionalized with carboxyphenyl (CP). It has already been shown that the deposition of CP is less efficient than that of NP. Hartig *et al.* have advanced the idea that these differences could be explained by differences in the dipole moment of the radicals. The dipole moment of the NP radical is perpendicular to the electrode surface and the less negatively charged side is directed to the surface, which can favor the fast grafting of NP and the formation of close-packed layers[7]. But this is not the only explanation of this phenomenon, many other hypotheses are discussed, as for example the formation of hydrogen bonds between the CP radicals, which can block further growth of deposited layer, but still a more detailed research on this topic was not yet realized. We have confirmed the difference in the efficiency for the electrografting of these different diazonium salts by studying the faradic yield of the reaction, as illustrated in Table 2. The values obtained for NBD and CBD, are of the same order of those founded by Belanger et al. using EQCM[8].

IV. 1. 3. Electrografting of dimethyl benzenediazonium salt

In the case of 2,6 dimethyl benzenediazonium (DMBD), we have confirmed the fact already discussed elsewhere, that for this specific diazonium salt, the grafting does not take place, as the formed radical is deactivated by steric hindrance[9].

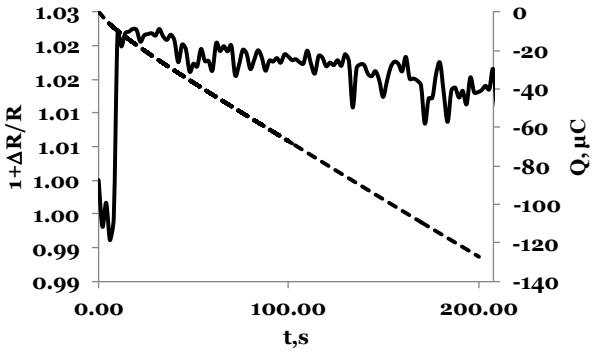

Figure 2.10 Electrografting of DMBD, C=5 mM in ACN+ 0.1M NBu4BF4, to an Au microelectrode (∅=250 µm), chronoamperometric potential step between 0.5 and -0.7V vs Ag/AgCl, t=200s; plain line - variation of light reflectivity during the electrografting; dashed line: the consumed charge during the electrografting reaction

As can be observed in Fig. 2.10 for the electrografting of (DMBD) even if the charge is consumed (dashed line), the light reflectivity remains almost constant (<0.4% decrease upon 200s). It is in agreement with a very low grafting yield, if any. Moreover in this context it was shown the acetonitrile could graft the electrode surface on long term electrolysis. The low variation of reflectivity may indicate the very slow acetonitrile grafting of the substrate.

This proves zero efficiency for the electrografting reaction.

z, nr. of transferred electrons per mol of diazonium		
	Opto-electrochemical microscope	**EQCM**
Φ-NO_2 (NBD)	between 2-4	1-1.5
Φ-COOH (CBD)	≈30	7-33
2,6-Me-Φ (DMBD	>100	

Table 2 Faradic yield of electrografting reactions of NBD, CBD and DMBD diazonium salts on a gold surface

V. *Applied potential and electrochemical activation duration – factors for controlling the thickness of deposited layer*

Another interesting application of our setup is its ability to confirm that the thickness of the deposited layer can be controlled either through the applied potential or the duration of the electrochemical modification. For example in Fig. 2.9, we obtain a direct measurement of the grafting yield with the electrode potential. For potentials -0.5 V<E<-0.2V, the faradic yield is not dependent on the potential, η ~50 %. By going to more negative potentials, we detect the formation of thicker layers, going from few hundred nm to 1 *μm*. Such representative case is shown in Fig.2.11 for the electrografting of NBD on gold microarray electrodes at high electric potential (E>-0.9 V).

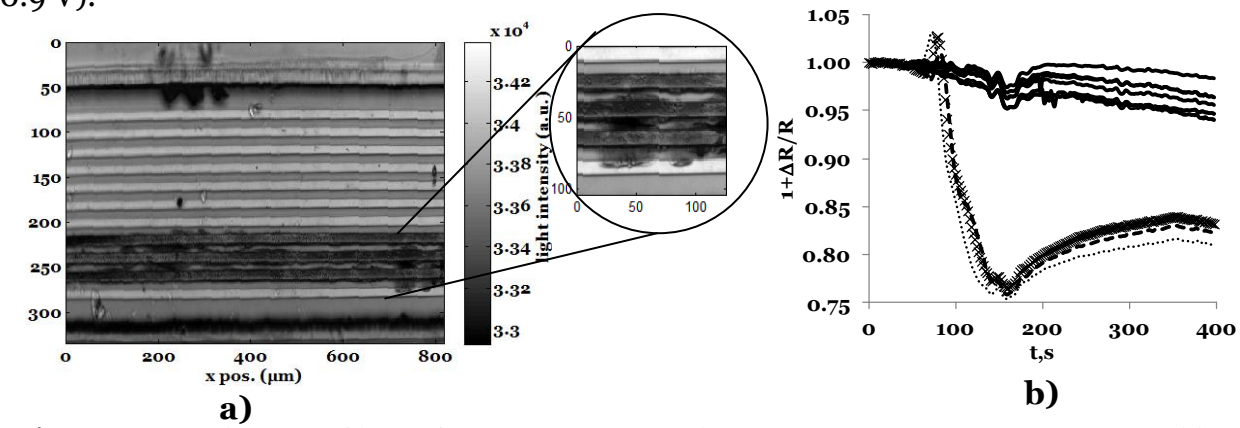

Figure 2.11 Electrografting of NBD (C=5 mM) in ACN + 0.1 M NBu4BF4 on gold microarray electrodes for a chronoamperometric potential step between 0.3 V and -0.9 V vs Ag/AgCl for 400s.

We are able to observe in Fig. 2.11(a) the heterogeneous diazonium grafting, with the formation of structures, which can overlap to neighboring bands, as observed in the zoomed region of grafted electrodes. The heterogeneous structures are mostly formed on the edge of the bands. During the application of this high negative potential, the reflectivity decreases on the 3 electrically connected bands by about 25 %. A slight decrease is also observed on the neighboring unconnected bands: the closer the band, the higher the decrease. Moreover, the 25 % decrease observed on the 3 bands (Fig. 2.11 b, bottom curves), is too high to be fitted by our optical model. These observations indicate the possible diffusion of reactive grafting species over ~10μm.

V. 1. *Electrografting of NBD at highly negative electric potentials*

Similar phenomena are observed when using highly negative potential at bigger substrates. In Figure 2.12, the electrografting of NBD is represented on a 500µm diameter gold microelectrode. We observe that light reflectivity presents periodic oscillations as predicted by theory. Moreover, the oscillations decrease when the film grows. From the optical model, minimum and maximum in $1+\Delta R/R$ occurs every $\mathbf{\Delta e}=\lambda/4n\approx82nm$ (positions associated to red circles in Fig. 2.12 a) and b) (for $\lambda=490nm$ and $n\approx1.5$). As predicted by theory, the variation of light reflectivity then corresponds to a deposition of an organic film of about 600 nm in thickness. Moreover, taking in consideration only the minimum and maximum values, a good correlation with the electrode charge is also found (Fig.2.12,c) with a faradic yield of ≈50%. The global decrease in light reflectivity observed in Fig. 2.12 a) is not predicted for transparent coating on a gold substrate. Some formed species under these highly negative potential conditions can be either diffusing or absorbing light. It can be assumed that at such potentials, anion radicals of nitrophenyl can be formed at the electrode. As the electrode surface becomes blocked for fast electron transfer, radical anions can mediate homogeneously the grafting[10] and form more complex nanostructures.

It also yields oligomeric structures that can be deposited onto the substrate by physisorption.

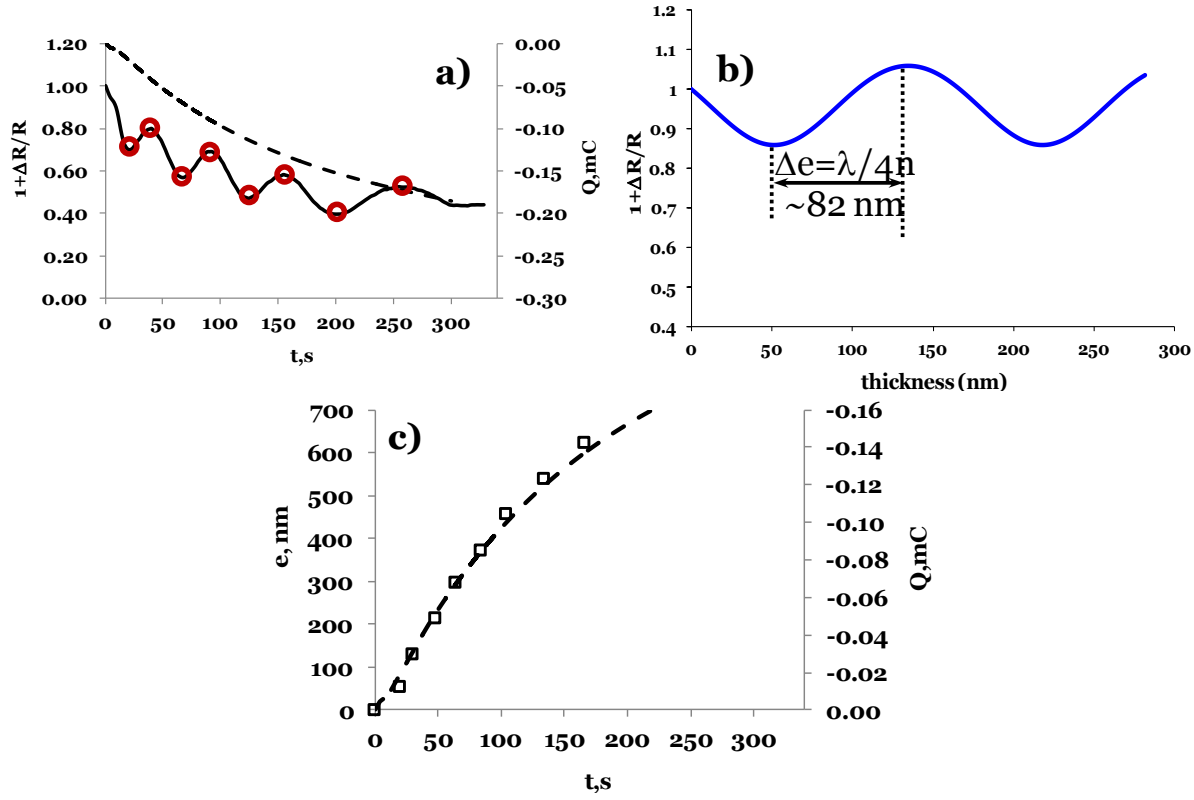

Figure 2.12 a) The electrografting of NBD salt (C=5 mM) in ACN + 0.1 M NBu_4BF_4 on a gold microelectrode (∅ = 500 µm), for a chronoamperometric potential step between 0.5 and -1.2 V vs Ag/AgCl for 300s, black line: the variation of light reflectivity, dashed line: consumed charge during the reaction; b) 1+ΔR/R theoretical variation with a deposited film thickness (λ=490 nm, $n_{ambient}$=1.33, n_{film}=1.5); c) variation of deposited film thickness (open squares) obtained from minima and maxima (red circles in a) of relative light reflectivity variation correlated with the charge (dashed line).

VI. *Optical investigation of deposited thick layers*

VI. 1. *Electrografting of NBD on ITO electrodes: Optical characterization of structures formed during electrodeposition at highly negative potentials*

As the reason of huge reflected light loss upon electrografting at highly negative potentials was not well apprehended, we wish to inspect the possibility of the formation of absorbing species during the electrografting process. Then the same electrografting at highly negative potentials was carried out on ITO electrodes in a spectrophotometer cell, while simultaneously monitoring absorption at the same λ as that used for reflectivity measurements (λ=490 nm).

As observed in Fig. 2.13, the electrografting of NBD at E=-1.2V vs Ag/AgCl forms absorbing species, as absorption increases with the deposition of an organic layer on the ITO electrode.

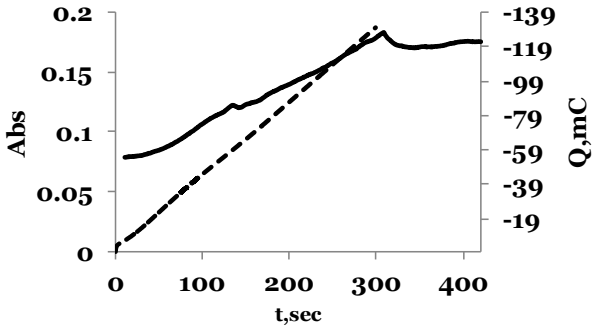

Figure 2.13 Electrografting of NBD (C=5 mM) in ACN + 0.1 M NBu4BF4 on an ITO electrode, for a chronoaperometric potential step between 0.5 and -1.2V vs Ag/AgCl, t=300s; black line: absorption; dashed line : charge consumed.

A good correlation of absorption with charge during the coating is found, demonstrating the formation of absorbing species during the grafting process. To characterize optically the formed structures during the electrografting on ITO electrode, we have calculated the experimental absorption coefficent (**α**) and extinction coefficient (**k**) for the film electrografted at highly negative potentials for the wavelength region λ=490 nm. In figure 2.14 the absorption spectra of the electrografted electrode is represented after the end of the electrochemical process.

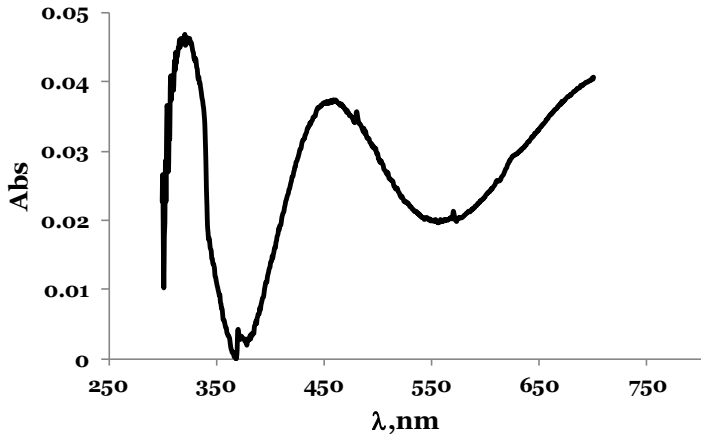

$\alpha_{exp,\ cm^{-1}}$	k_{exp}
1.711E+03	6.67 E-03

Figure 2.14 Absorption spectra of the electrografted electrode at the end of the electrochemical process in the presence of ACN and NBD.

The absorption spectrum can be assigned to the formation of aromatic multiconjugated oligomeric structures, composed mainly of 1 or 2 nitrosubstituted phenyl moieties.

The absorptivity contribution can be implemented in the optical model that describes light reflectivity. The theoretical variation for absorbing film with **ε** and **k** close to the values determined experimentally (α_{th}=2.5 E+03 cm^{-1}, $\mathbf{k}_{th}$=0.01 for λ=490nm) is represented in figure 2.15.

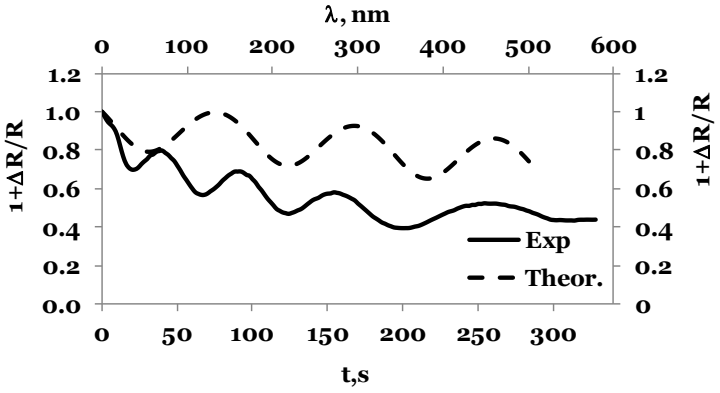

Figure 2.15 Comparison of experimental (black line) showed in Fig.2.11, and theoretical (dashed line) light reflectivity for λ=490 nm with a deposited film thickness (only for theoretical variation).

A general decay of ΔR/R is confirmed eventhough it is not the only effect detected here. A possible difusing structure (disordered oligomeric structure) could be postulated. This is confirmed from the images of disordered materials obtained under such electrografting processes, as illustrated in the magnification proposed in Fig 2.11.

VI. 2. *Desorption of nonchemisorbed structures obtained during the electrografting at highly negative potentials*

The presence of a complex film structure is confirmed by further optical characterization of the deposited layer. When an electrode has been grafted by NBD at highly negative potential and further sweeped in an electrolyte solution containing no NBD (0.1 M NBu_4BF_4 in ACN) between 0.1 and -1.4 V, a change in light reflectivity

is observed (Fig. 2.16). For E>-0.1V, ΔR/R increases, indicating a decrease in the thickness of the layer. This phenomenon can be assigned to the opening of the grafted structure upon potential activation and to the release of physisorbed species [10].

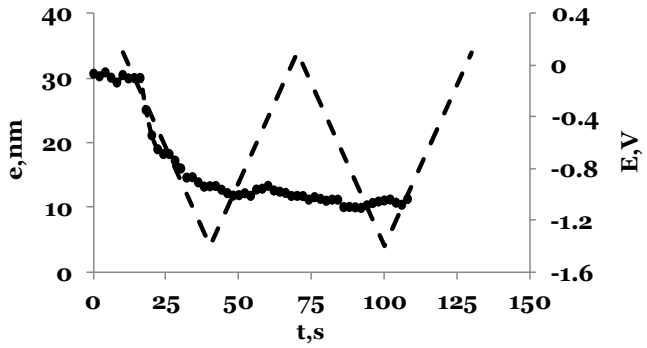

Figure 2.16 Release of adsorbed species during the electrografting of NBD at highly negative potentials by biasing the grafted electrode in a electrolyte solution of 0.1 M NBu4BF4 in ACN between 0.1 V and -1.4 V vs Ag/AgCl.

We observe similar results for the characterization of the ITO electrode electrografted at highly negative potentials. The absorption spectra of the grafted ITO electrode were recorded at different time intervals during the potential sweeping in a solution containing only the supporting electrolyte (0.1 M NBu_4BF_4). As observed in Fig. 2.17, after an electrode potential application for 257 s, the absorptivity of the previously electrografted species has almost disappeared. This is consistent with a release of oligomer structures formed inside the film, along with solution discoloration.

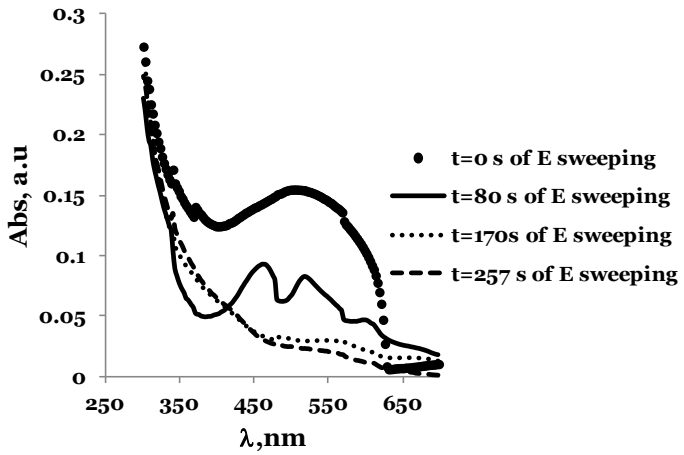

Figure 2.17 Variation of absorption during the biasing of an electrografted ITO electrode in a solution containing only the electrolyte (0.1 M NBu4BF4 in ACN) between 0.5 et -1.2 V for 300s.

VII. *Application of electro-optical imagery setup to monitor biological reactions: Immunoassay on gold surface*

Once the detection mode based on light reflectivity has been validated, and the coupling with electrochemical techniques has been used to apprehend chemical reactivity on different surfaces using as a model system the electrografting of diazonium salts, we have tested our device to develop an imunoassay platform. It consists of immobilizing a target biological molecule on a refelecting surface, for exemple an antigen on a gold surface. The detection of the interaction between the immobilized antigen and its associated antibody results from the comparison of the surfaces images before and after the interaction with the antibody. The quantitative estimation of the relative change of reflectance is then obtained using the principle presented in section II.1, by comparing the light intensity measured on the first image, $I_o(i,j)$ at each pixel of coordinates (i,j), with the intensity measured on each pixel of the same image obtained at the time interval t, $I_t(i,j)$, giving $1+\Delta R(t,i,j)/R= I_t(i,j)/I_0(i,j)$. The real time detection is performed simply by *in situ* monitoring, in an aqueous solution, for example a solution of a serum, the intensity of the beam reflected at the surface. The quantitative determination of the amount of immobilized material is directly obtained from the measurement of $1 +\Delta R/R$ and the theoretical correlation of 0.43% decrease for 1 nm of deposited homogeneous film.

VII. 1. *Detection of antigen-antibody interaction (Ag-Ab)*

VII. 1. 1. Preparation of the immunosensor surface

In a first step one has to prepare the immunoassay platform. It consists in immobilizing on a gold surface a biochemical entity able to trap a target in a solution. In the case of antigen-antibody recognition one can either anchor the antigen or the antibody on the Au surface for, respectively, efficient detection of the antibody or antigen present in a test solution. The anchoring of biomolecules on a gold surface can be apprehended by electrografting processes. Several methods of electrochemical surface functionalization are described in the literature using for example, diazoniums[11] or [12].

The electrochemistry of diazoniums allow to graft onto an electrode either (1) a carboxyphenyl group ($-C_6H_5COOH$) from carboxybenzenediazonium ($+N_2C_6H_5COOH$) or (2) an antigen from the corresponding diazonium that can be prepared by peptide coupling between the antigen and the same carboxybenezenediazonium[11]. Path (1) introduces selectively the carboxyphenyl group on any polarized electrode. Path (2) allows to graft directly and selectively an antigen on an electrode polarized at a potential less than -0.4 V vs. SCE.

Following path (1), the further anchoring of, say, an antigen will be achieved by peptide coupling (by use of reagents like EDC (1-ethyl-3-(3-dimethylaminopropyl)-carbodiimide)/NHS (N-hydrosuccinimide) between the COOH group anchored on the surface and the antigen present in a solution. The immunosensor surface optimization often requires the hindering of sites for nonspecific interactions. These nonspecific interactions could be limited by surface passivation treatments as recommended in the literature either by PVP[13] or PEG[14, 15] treatment.

VII. 1. 2. Principle of immunosensing detection

An example of immunoassay on a gold surface is given in Figure 2.18, which represents the evolution of the reflectivity on an area of 5x5 μm^2 of a gold surface submitted to the interaction between the β-lactoglobulin and its associated antibody present in a rabbit serum.

We were then able to realize a quantitative analysis of a biochemical reaction. The amount of target molecules immobilized on the surface could be deduced from the relative change in reflectivity. For example, in Figure 2.18B, the reflectivity measured at long times on a 5x5 μm^2 region corresponds to the adsorption of 4.5 ng/mm^2 of the antibody, corresponding to a surface concentration of $3x10^{-14}$ mol/mm^2. The image of the entire surface can map the homogeneity of the surface coverage by the antibody throughout the whole imaging field (for example: 400x400μm^2 with a resolution of 0.4 μm).

It is also possible to determine, from the in situ and real-time monitoring of the antigen-antibody interaction, the kinetics and thermodynamics of this recognition process. The kinetics presented in Figure 2.18 B, where a decrease in reflectivity is observed, can be analyzed, as for example in many SPR biosensors, by a process of

adsorption / desorption of the first order. The experimental reflectivity variations are compared to an exponential evolution of the Langmuir type (red curve in Figure 2.18 B). From the comparison between the experiment and the model, the apparent speed of antibody-antigen coupling is extracted.

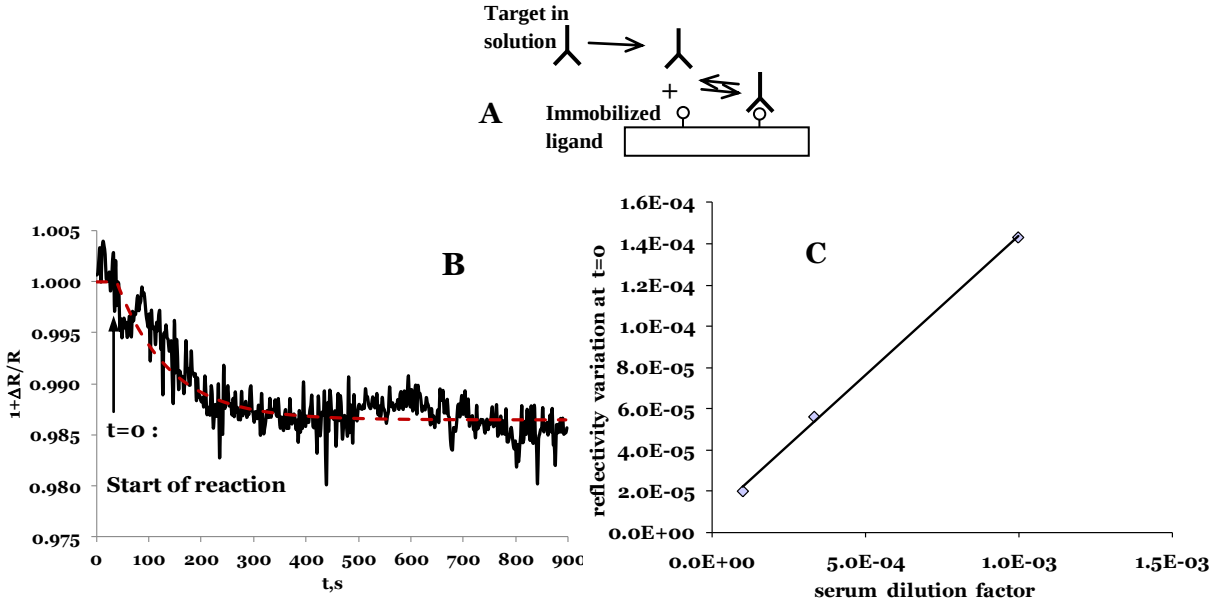

Figure 2.18 Real time in situ evolution of the interaction between immobilized β-lactoglobuline on a gold surface with its associated antibody in a solution of rabbit serum. **A** : principle; **B** : experimental kinetic response (black) considering an adsorption kinetics. **C** : dynamic range of the immunoassay obtained from the slope (in s^{-1}) for short intervals using Langmuir model (the starting point is at t=40 s, that corresponds to the injection of the target molecule).

The sensitivity and dynamic range of the immunoassay are preferably obtained by the slope at the origin of the variation of the reflectivity with the reaction time. In the case of β-lactoglobulin and a 4 μm^2 gold surface with, the sensitivity corresponds to a dilution of 1/50000 of the patient serum that is comparable to that obtained by SPR (1/30000). The linear dynamic range of detection extends serum dilutions from 1/50000 to more than 1/1000.

The observation of the interaction of the rabbit serum with ovalbumin shows high selectivity for β-lactoglobulin since no interaction is detected for a solution of diluted serum to 1/1000.

VII. 2. *Detection of sandwich immunoassays - Antibody/anti-antibody (IgG/Anti-IgG)*

As for ellipsometry, the reflectivity measurement is not associated with the creation of an electromagnetic evanescent wave propagating near the surface of the reflective metal film (surface plasmon). Contrary to SPR, based on the detection of disturbances of this evanescent field induced by the layer, the detection by measuring the reflectivity is not limited to thin films of thicknesses less than the penetration depth of the evanescent wave (less than 150 nanometers with a decreasing sensitivity when the thickness of the layer increases). It is therefore possible (in theory) to observe by this technique more complex biomolecular assemblies including, for example, multi-stack biochemicals or even to track linkages to larger objects, such as agglutinated or assembled nanoparticles or nano-objects on a gold surface.

We were able to show in situ and real-time the presence of an antibody (anti-α-lactalbumin, IgG) immobilized on a reflective surface by interaction with its associated antigen (α-lactalbumin) present in solution (Figure 2.19 A), and also by subsequent interaction of the immobilized antibody with its associated anti-IgG (Figure 2.19 B).

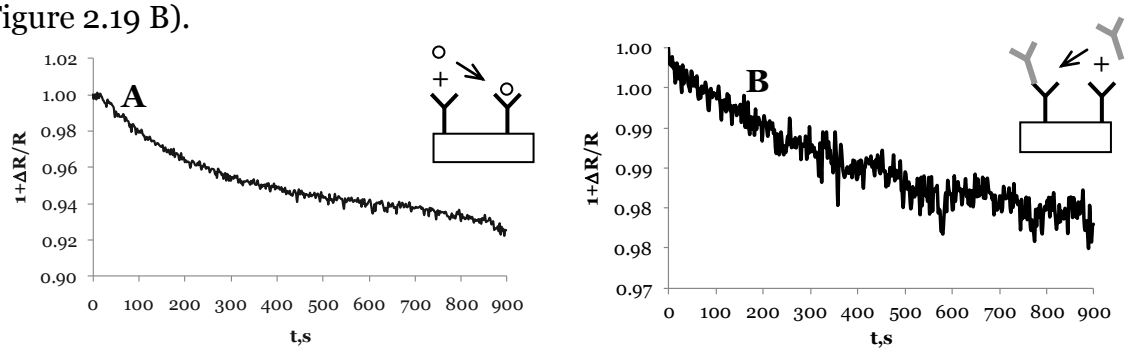

Figure 2.19 Monitoring in real time and in situ of the interaction between the antibody of α-lactalbumin (IgG) immobilized on a gold surface and α-lactalbumin in solution (antigen, A) or anti IgG (B); measurements realized with 0.2 µmol/L of a-lactalbumine (A), and with a serum of anti-IgG diluted to 1/1000 (B).

This example shows that, using our device, it is possible to detect immunological full sandwiches (sequence Ag / Ab / anti-Ab) without loss of sensitivity, which is more difficult to realize by SPR. Finally, all the assemblies can be separated by contact with a solution of glycine or another solution of high ionic strength. This rapid dissociation

can also be followed by imaging in situ and in real time of the subsequent increase in surface reflectivity.

VIII. *Strategies to develop new design of immunoassay using the electro-optical imagery*

Once the methodology for the detection of immunological reactions has been validated, we have developed two strategies for high throughput label free immunoassay platforms.

VIII. 1. *Immunoassay in miniaturized format*

The first approach is based on microfabrication and microfluidics. Microfabrication allows to deposit microstructures of the desired architecture, as micro-zones of gold, on any type of substrate (glass, polymer) and electrically addressing them individually (array of gold microelectrodes). In a high-throughput chip-type immunoassay a large number of protein ligands (for example different antigens) are immobilized on the microelectrode. The selective immobilization of an antigen on a microelectrode is made possible by the use of an electrochemical process: one can activate selectively and independently an electrode by applying an electric potential or current in order to change its surface chemistry.

As proposed earlier this step of surface functionalization can be followed in real time and in situ by imaging relative changes at the surface. For example, Fig. 2.20 shows the selective electrografting of an organic layer derived from a diazonium on a gold microelectrode inserted in a microfluidic channel. An organic layer grows only on the electrochemically activated microelectrode, which is evidenced by the decrease in the reflectivity of this only connected microelectrode during the grafting (from red to blue in fig. 2.20 B).

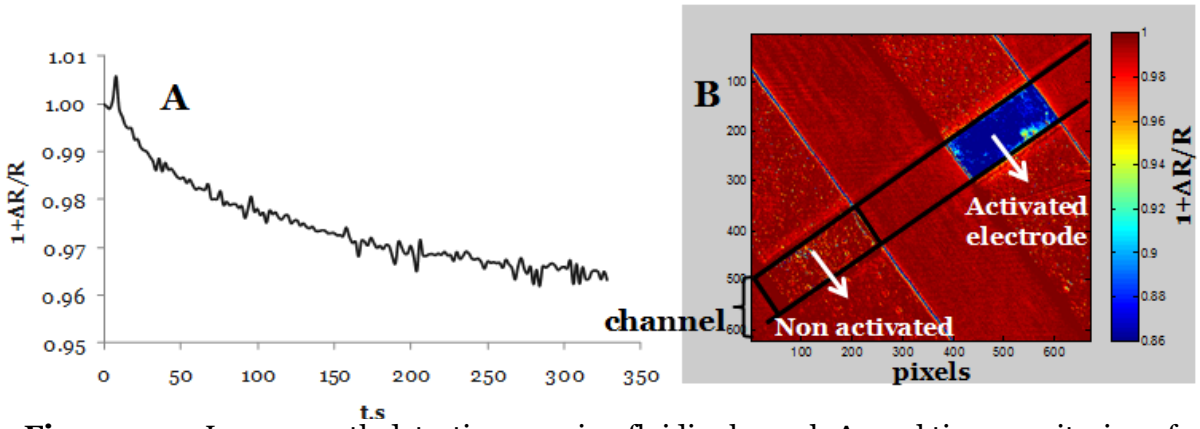

Figure 2.20 Layer growth detection on microfluidic channel; **A:** real time monitoring of kinetics of film growth with a final thickness of about 10 nm obtained from the electrografting of a diazonium salt; **B** : reflectivity image showing the selective deposition of a thin layer (about 30 nm) on the activated gold electrode .

Our device that allows to detect in situ and in real time the deposition of a thin film resulting from a biochemical reaction can be used to define a miniaturized immunoassay in closed microfluidic cell as schematized in Fig. 2.21.

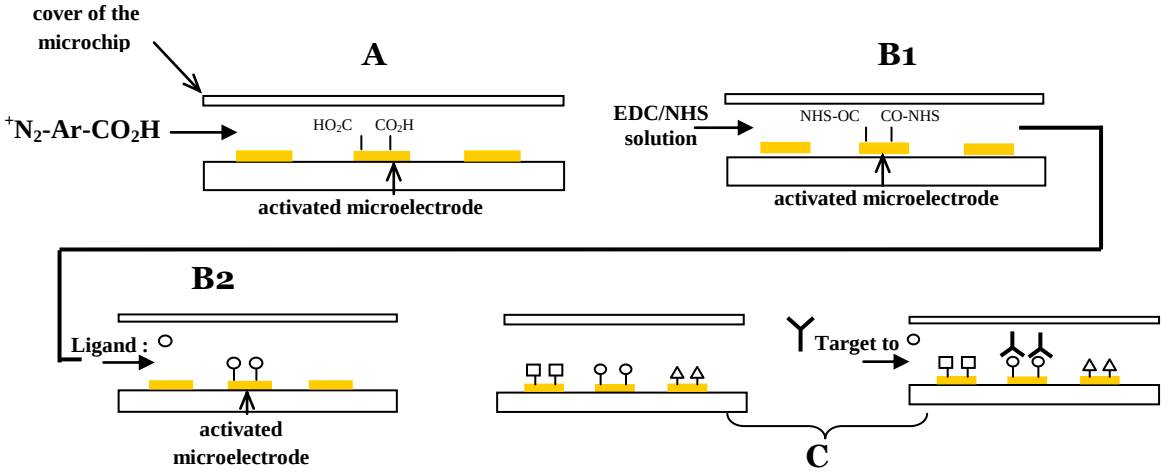

Figure 2.21 Example of an immunoassay in a microfluidic cell: preparation of a platform with multi-ligands by repetition of the procedures from step A+B: A: selective electrografting of an initial attaching layer by electrochemical selective activation of a microelectrode; B1+B2: Selective coupling of a ligand; C: Multiple detection of a biological target present in a mixture solution.

The imaging of the reflectivity informs simply about the selectivity of each step: the surface functionalization by the COOH terminal group (step A), the selective attachment of the ligand (B1+B2), and the selective detection of the target on the electrode functionalized with the corresponding antigen.

The specificity of the reaction is evidenced simultaneously by testing the functionalized electrode with another antigen (step C).

This approach is not limited to the simple platform described here, consisting of a microelectrode array implanted in the bottom of a microfluidic channel. It can be adapted to platforms made of microcantilevers addressed individually. In this way, a configuration derived from that proposed in [16] can be used. It consists of lighting the surface by 2 wavelengths to decouple the optical contributions related to the deformation of the cantilever and to the biochemical reaction, by identifying the dependent and independent contributions of the wavelength. A two-color light is obtained easily and inexpensively by using LEDs. Selective activation of different cantilevers is also made possible by the electrochemical activation and electrografting methods already mentioned. These electrochemically activated platforms allow to increase the number of detection parameters (optical and electrochemical, also mechanical in the case of microcantilevers). This redundancy of measures of interactions can increase the reliability of the immunoassay.

VIII. 2. *Immunoassay on big surfaces*

The second proposed strategy is related to the construction of big format immunoassays. Due to the principle of the measurement, we are not constrained by the size of the substrate to be analyzed. Indeed, the detection of the presence of a protein of interest is obtained by comparison point-by-point of an image of the substrate before and after (or during) the immobilization of the protein on the substrate.

The analysis of a large substrate (> 5x5cm^2, for example) is possible by reconstruction from images of different regions (succession of images, and surface displacements relative to the objective). This requires to image first (all or part of) the substrate surface before the immobilization step that we want to study. In this configuration, the first acquisition is taken as the reference image. For example, for each image, the parts of the image where the intensity values are the highest can be taken as reference

region. The substrate images obtained after immobilization will be compared to those of the reference, thus the immobilization step will be identified.

For each region, the presence of a protein (or interaction) on the surface is detected by a local decrease of the surface reflectivity. The analysis can be done either ex-situ to increase the detection sensitivity, or in situ.

We discovered the possibility of detecting immunological reactions by reflectivity only recently. Even if we are controlling separately each step of the proposed procedures for the miniaturized or big formats immunoassay, so far we are not able to setup a complete immunoassay, neither in miniaturized or big formats. Nevertheless, the obtained results are very promising, mainly for the ex-situ analysis of big surfaces for the moment. In the case of the miniaturized format immunoassay, the problems are coming from the difficulties of the deposition of the –COOH group by electrografting of carboxybenzenediazonium. One known reason is that the electrografting of this specific diazonium salt is not very efficient, forming only a very thin layer on the gold substrate. Another problem is related to the choice of the pumping system. The surface forces are more important in microchannels than at the macroscopic scale and the organic layer can be quickly destroyed. To handle this point, it is very important to have a good control of the flow in the channel. We have tested few pumps, and good results were obtained. As the proof of concept was shown, we hope that the complete immunoassay based on the presented strategies will be operative soon.

Conclusion

The proposed setup of electro-optic real-time imaging based on light reflectivity measurement was validated on different structures, going from macro to micrometer substrates using as a model system the electrografting of diazonium salts. Two main results must be pointed out. Firstly, this setup is a good alternative as a sensing approach with the advantages of obtaining the same range of sensitivities as QCM or SPR techniques in a more simple way. Secondly, the imagery mode was validated for in situ and real time surface chemistry analysis. Reflectivity measurements allow to follow in-situ the growth of electrografted layers in real-time on electrode > 1µm with sensitivity <1 nm and time resolution <1s. The controlled film growth kinetics can be accessed on small reflecting surfaces. The heterogeneous film structuration at E<-0.7 V was evidenced, with a deposition on surface of a disordered oligomeric structure composed mainly of nitrosubstituted phenyl moieties, which may have light diffusing properties. The imagery mode allowed the local characterization of surface modification with little lower sensitivities than the SPR and QCM. The opto-electochemical imagery technique was also validated for the development of Au immunoassays platforms. The detection of antigen-antibody reaction was confirmed. The advantage over SPR was evidenced through the detection of sandwich immunoassays, application which is difficult to realize by SPR due to limited penetration depth of the evanescent wave. The initial results of two proposed strategies for the immunoassay in miniaturized -based on microfabrication and microfluidics, and big formats were discussed with perspectives of developing fully functional immunoassays very soon.

References

1. Jin-Lee, H., T.T. Goodrich, and R.M. Corn, *SPR imaging measurements of 1-D and 2-D DNA microarrays created from microfluidic channels on gold thin films.* Analytical Chemistry, 2001. **73**(22): p. 5525-31.
2. Lee, H.J., A.W. Wark, and R.M. Corn, *Creating advanced multifunctional biosensors with surface enzymatic transformations.* Langmuir, 2006. **22**(12): p. 5241-5250.
3. Singh, B.K. and A.C. Hillier, *Surface plasmon resonance imaging of biomolecular interactions on a grating-based sensor array.* Analytical Chemistry, 2006. **78**(6): p. 2009-2018.
4. Downard, A.J., *Electrochemically assisted covalent modification of carbon electrodes.* Electroanalysis, 2000. **12**(14): p. 1085-1096.
5. Pinson, J. and F. Podvorica, *Attachment of organic layers to conductive or semiconductive surfaces by reduction of diazonium salts.* Chemical Society Reviews, 2005. **34**(5): p. 429-439.
6. Belanger, D. and J. Pinson, *Electrografting: a powerful method for surface modification.* Chemical Society Reviews, 2011. **40**(7): p. 3995-4048.
7. Hartig, P., T. Dittrich, and J. Rappich, *Surface dipole formation and non-radiative recombination at p-Si(111) surfaces during electrochemical deposition of organic layers.* Journal of Electroanalytical Chemistry, 2002. **524–525**(0): p. 120-126.
8. Laforgue, A., T. Addou, and D. Belanger, *Characterization of the deposition of organic molecules at the surface of gold by the electrochemical reduction of aryldiazonium cations.* Langmuir, 2005. **21**(15): p. 6855-6865.
9. Combellas, C., et al., *Steric Effects in the Reaction of Aryl Radicals on Surfaces.* Langmuir, 2009. **25**(1): p. 286-293.
10. Ceccato, M., et al., *Nitrophenyl Groups in Diazonium-Generated Multilayered Films: Which are Electrochemically Responsive?* Langmuir, 2010. **26**(13): p. 10812-10821.
11. Corgier, B.P., et al., *Protein-Diazonium Adduct Direct Electrografting onto SPRi-Biochip.* Langmuir, 2009. **25**(16): p. 9619-9623.
12. Herrwerth, S., et al., *Covalent coupling of antibodies to self-assembled monolayers of carboxy-functionalized poly(ethylene glycol): Protein resistance and specific binding of biomolecules.* Langmuir, 2003. **19**(5): p. 1880-1887.
13. Lou, X.J., et al., *Increased amplification efficiency of microchip-based PCR by dynamic surface passivation.* Biotechniques, 2004. **36**(2): p. 248-+.
14. Kenausis, G.L., et al., *Poly(L-lysine)-g-poly(ethylene glycol) layers on metal oxide surfaces: Attachment mechanism and effects of polymer architecture on resistance to protein adsorption.* Journal of Physical Chemistry B, 2000. **104**(14): p. 3298-3309.
15. Bearinger, J.P., et al., *Chemisorbed poly(propylene sulphide)-based copolymers resist biomolecular interactions.* Nat Mater, 2003. **2**(4): p. 259-264.
16. Garraud, N., et al., *Multiple wavelength reflectance microscopy to study the multiphysical behavior of microelectromechanical systems.* Optics Letters, 2011. **36**(4): p. 594-596.

Chapter 3 : Imaging the local chemical and biochemical surface reactivity using opto-electrochemical microscope

I. *Introduction*

In the previous chapter we have demonstrated how we were able to detect and follow quantitatively in-situ and in real time the growth of a thin organic layer on a surface by coupling electrochemical activation with light reflectivity. The versatility and simplicity of the proposed technique were proven from its ability to characterize the chemical reactivity of different shapes and natures of surfaces. In this chapter, we are more particularly focused on the association of this optical microscopy to the direct measurement of light reflectivity change. This will provide a light reflectivity microscope able to interrogate local light reflectivity changes at the (sub-) micrometer range. We wish to inspect the performance of such optical microscopy by light reflectivity to image and address the local chemical reactivity or the local chemical structuration of surfaces.

The phenomena that will be analyzed in this way can be divided in two groups. The first ones are related to the visualization of the chemical heterogeneities of patterned surfaces. Light reflectivity images taken in the air provide the most sensitive mode of detection of organic layers with a sub-monolayer limit of detection. It is then possible to detect and characterize the possible chemical modifications locally introduced on a patterned surface.

A second part concerns the imaging of the heterogeneity of the chemical reactivity of a surface. This imaging is then obtained from *in-situ* and real time measurement. It is, as before, illustrated in the case of the reactivity of the nitrophenyl (NP) radicals formed by the electrografting of the 4-nitrobenzenediazonium (NBD) salt, vis-à-vis different species immobilized on a surface. For both aspects, heterogeneities will be introduced on a surface from standard patterning procedures: μCP (micro-contact printing) or UV-VIS photolitographic techniques.

II. *Imaging the chemical structuration of patterned surfaces*

Light reflectivity measurements in air provide a very sensitive method of detection of organic material adsorption on a reflecting surface. In principle, it allows a very fast and efficient quantification of the amount immobilized with sub-monolayer limit of detection.

II. 1. *Imaging fingerprints*

For example, Fig. 3.1 is shows how the technique can be used to detect fingerprints on an Au wafer surface.

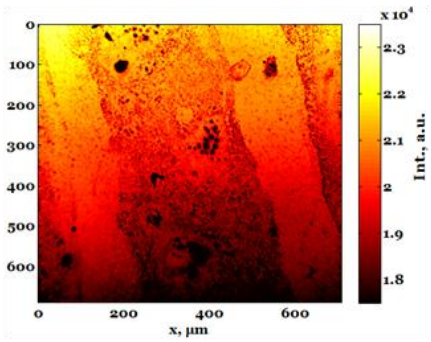

Figure 3.1 Light reflectivity image taken in air of a fingerprint on Au substrate

This presents the most simple μCP transfer of molecules on a surface associated with its very crude visualization from the change in reflected light intensity.

As can be observed, the stripes corresponding to higher (with better contact with the substrate) and lower regions of the fingerprints can be easily distinguished. The area with lower intensity (black) is assigned to the higher zone, which shows that during contact with the Au surface, natural secretion as sweat or the fat species from the fingerprint grease has been transferred onto the Au surface. The fingerprints are highly heterogeneous as a lot of defects at the 10μm scale are detected. A wide field image of the whole fingerprint is also possible by successive snapshots and image reconstruction.

II. 2. *Imaging surfaces patterned by microcontact printing (μCP)*

One of the most popular methods for the patterning of surfaces with dedicated chemical functionality is the μCP. This surface modification method is a form of soft lithography, which uses the relief patterns of a master polydimethylsiloxane (PDMS) stamp for patterned transfer of different species as chemicals or biological materials onto surfaces [1, 2]. The procedure of this modification method consists in a succession of steps, as depicted in Fig. 3.2.

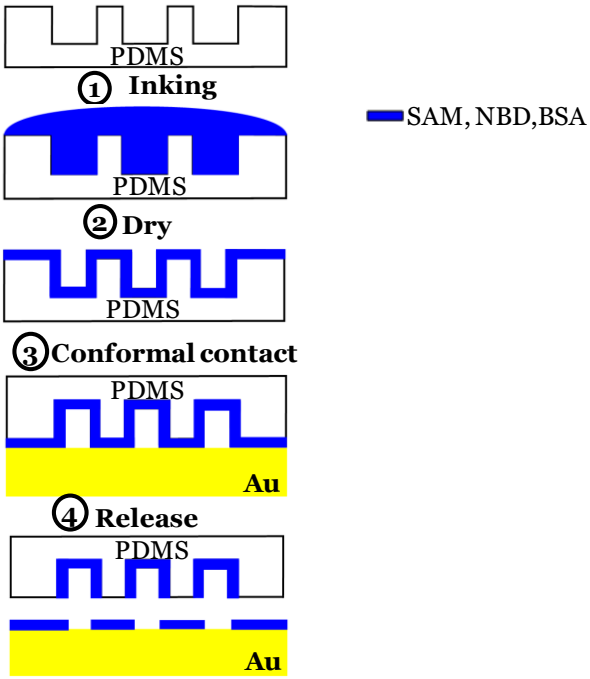

Figure 3.2 Diagram illustrating μCP procedure for Au surface patterning with chemicals.

After the PDMS stamp is peeled from the desired template and cut to the needed size, the stamp is inked with the material to be printed on the surface, step 1, Fig.3.2. Then the surfaces are allowed to dry or the solution in excess is removed, step 2. To transform accurately and uniformly the material from the stamp to the substrate, the stamp needs to be characterized by two properties: the first one is related to the high mechanical stability of the micro-structures and the second, the potentiality to form conformal contact down to the nanometer scale, despite the potential roughness of the substrate.

The quality of conformal contact, step 3, is controlled by the elasticity of the stamp structure. After mask releasing, step 4, the material is transferred to the substrate.

We have used this strategy to transfer from PDMS stamps onto Au wafer surface different sizes and chemical structures of thiols (SAM), nitrobenzendiazonium (NBD), and proteins (BSA- bovine serum albumine).

Light reflectivity microscopy is then well adapted to characterize the stamped surfaces and allows in principle determining the thickness of the material transferred from the stamp to the substrate. Figure 3.3 a) presents the image of an Au surface printed with a PDMS stamp composed of disks of 100 μm in diameter, spaced by 100 μm, and inked with NP. Due to the high sensitivity of the method in air, the periodic structure of the stamp is reproduced on Au and the transferred patterns are visible as the regions of lower light reflectivity, in agreement with the deposition of organic moieties on the Au surface.

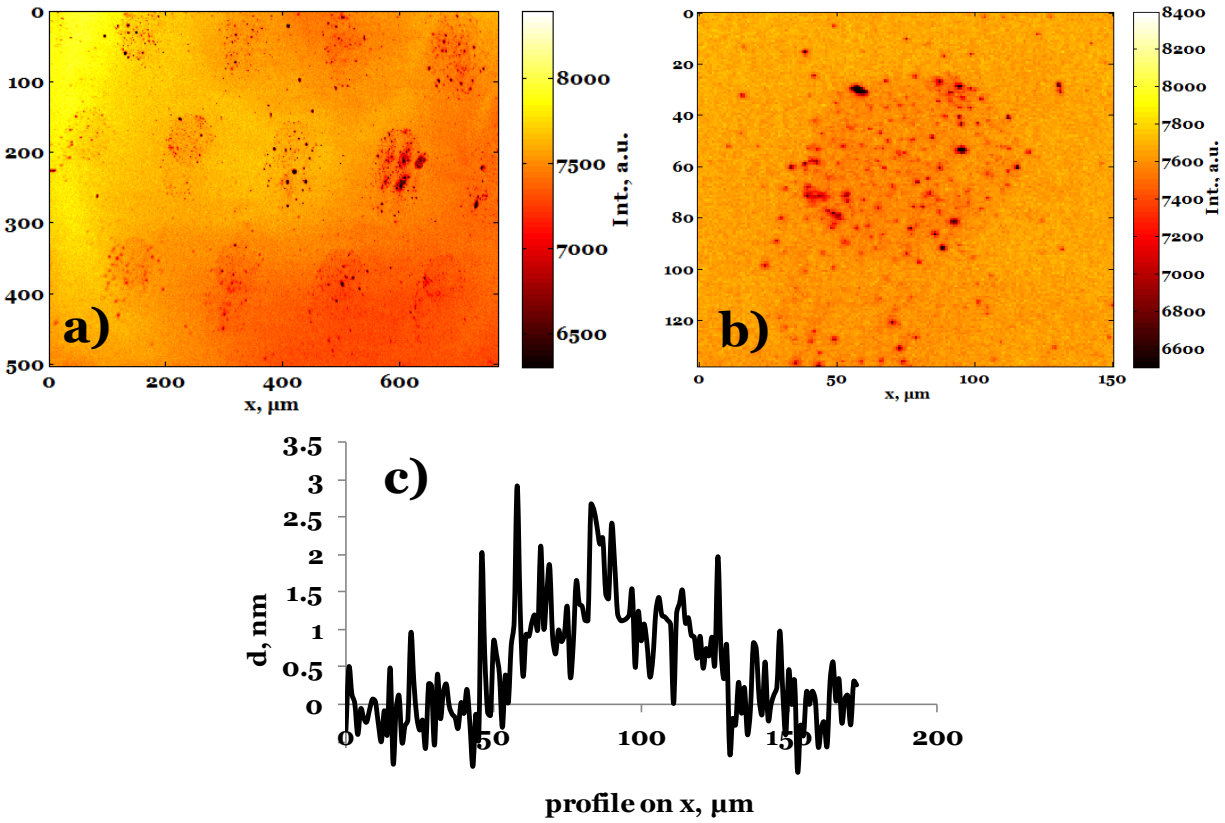

Figure 3.3 Light reflectivity images in air of Au substrate printed with NBD (C=20 mM) in H_2SO_4 (1M): a) full-field image and b) magnification of a single printed spot; c) Cross-section profile (thickness) along x direction on the single spot image.

At the level of a single printed pattern, a higher resolution image (Fig 3.3, b) and analysis of the thickness of deposited material can be obtained. Fig 3.3 c presents a plot of the layer thickness profile along the x direction on a single spot image, which was obtained from the average difference in intensity on the non-modified Au and the stamped region. A thickness ≈1.1 nm of transferred material was estimated from the light reflectivity image. Within individual patterns, the amount of transferred material does not seem homogeneous as much darker regions (disks <2µm diameter) are clearly observed, and more material seems to be transferred along the edge of the pattern (Fig 3.3.c).

II. 3. *Imaging surfaces patterned by photolithography*

As surfaces patterned with µCP could present some heterogeneities, we have examined another concurrent way of patterning surfaces. We have then apprehended experimentally the patterning Au surfaces with chemical structuration using standard UV-VIS photolithographic techniques. The scheme of the entire procedure used in this work is drawn in Fig. 3.4 that represents the preparation of a pattern on an already self assembled monolayer of thiol adsorbed on an Au surface.

A bare gold wafer was immersed for 24 h in a solution of 1-decanethiol (C=1 x 10^{-3} mol L^{-1}) (step 1, green rectangle), then a photosensitive resin (AZ5214, Clariant) was deposited on the thiolated gold wafer via spin coating (second step, the blue rectangle). Afterwards, the surface was exposed to UV irradiation (365 nm) through a mask with the designated pattern (step 3). The photoresist was developed with AZ726MIF developer (TMAH-tetramethylammonium hydroxide). The final step consisted of the local etching of the thiol layer in the regions where the resin on the sample had been removed, by reactive ion etching (RIE, step 4). The areas without photoresist are then exposed to O_2 plasma and the thiol layer is removed. The final removing of the resin is achieved by rinsing the sample in acetone under ultrasound activation, which allows at the end of these surface modifications steps, obtaining a structure as shown after step 5.

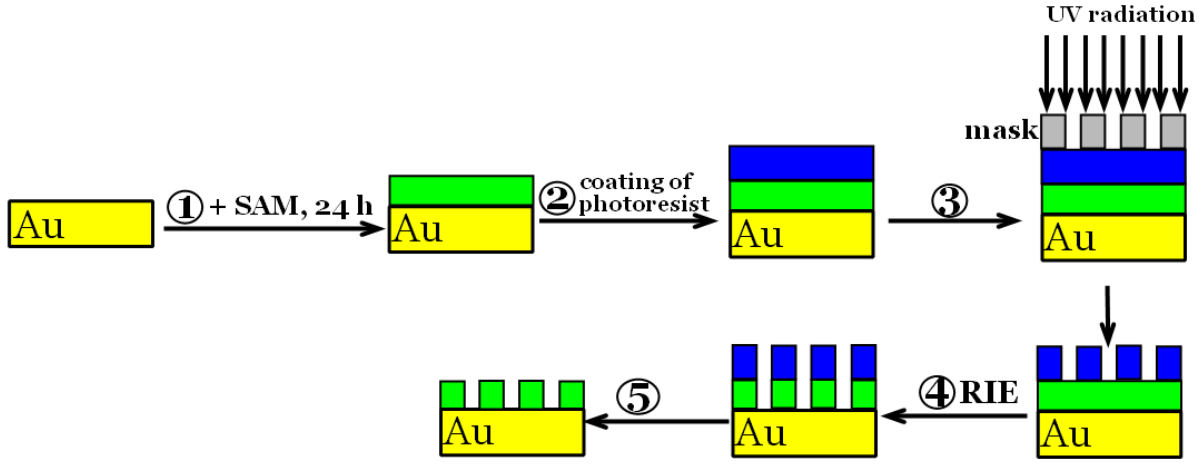

Figure 3.4 Illustration of the steps of UV-VIS photolithography performed for the preparation of patterned Au substrates

First, the general scheme presented in Fig 3.4 was applied to a bare Au surface non-modified by a thiol (step 1 has been omitted) prior the photolithographic transformation. The surface then obtained was imaged in air by light reflectivity as represented in Fig. 3.5. This figure shows that the photolithographic procedure yields the formation of patterns on the surface which consists in the etching of disks of 24µm diameter spaced by 120 µm, in agreement with the dimensions and periodicity of the holes present on the photomask. The patterns corresponding to areas irradiated by both UV and RIE treatments appear as regions of higher reflectivity.

The pattern results from the action of the vigorous RIE. The difference in the intensity between the irradiated and protected regions can be explained by the modification of the structure of the Au inside the disks due to RIE, which is affecting consequently the optical response of these zones. It suggests that the action of RIE makes the surface more reflective than the original bare Au, showing the cleaning effect of the RIE (removal of oxide or contaminant traces). As will be discussed later, this demonstrates that RIE and cleaning procedures may strongly modify the optical properties of surfaces and this will most likely affect the chemical reactivity of the overall surfaces. When the whole photolithographic procedure has been applied to a thiol-coated Au wafer, similar patterned images have been obtained. As the RIE intrinsically 'cleans' the Au surface, it is difficult to quantify, as was done with µCP, the effect of RIE on the thiol removal directly from light reflectivity imaging.

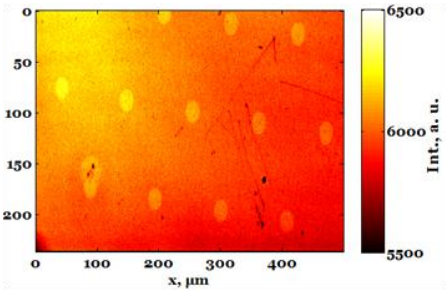

Figure 3.5 Light reflectivity image in air of a bare Au surface modified by UV-VIS photolithography

III. *Imaging in-situ and in real-time the local chemical reactivity of surfaces*

We have shown how light reflectivity microscopy can be used as a useful and simple tool to image the impact of patterning techniques for local chemical transformation of surfaces. In the next section, we wish to illustrate its further potentiality for the *in situ* and real time imaging of the local electrochemical reactivity of electrode surfaces during an electrografting process. This was analyzed following two approaches. In the first one, the electrochemical reactivity was examined from evidencing the grafting heterogeneity on a single micrometric surface (a microdisk electrode or a microcantilever). This was already presented in Chapter II on arrays of microelectrodes, where differences in the grafting were observed for connected and non-connected electrodes. Here we rather inspect heterogeneity appearing within an individual microelectrode as peculiar electrical and mass-transfer edge effects are expected to occur. The second approach consists of imaging the reactivity of generated $Ar^{\bullet}$ radicals during the electrografting of NBD on chemically structured Au surfaces. The chemical structuration has been introduced from the pre-patterning of the Au surface with different moieties, either by μCP or UV-VIS photolithographic techniques. We expect to detect the reactivity of electrogenerated radicals, $Ar^{\bullet}$, towards different chemical species immobilized on the surface, from the differences in grafting kinetics between the non-modified (bare) Au regions and those chemically modified by chemical moieties, as depicted in Fig. 3.6.

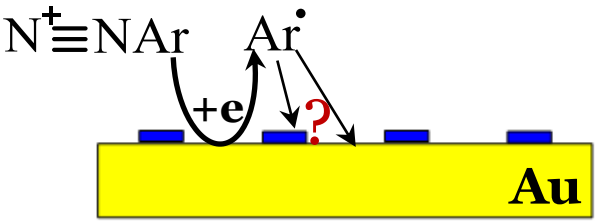

Figure 3.6 Principle of the inspection of local chemical reactivity of $Ar^{\bullet}$ radical towards different species (blue rectangle) patterned on an Au surface.

III. 1. *Electrochemical activation as a source of heterogeneous reactivity*

III. 1. 1. Heterogeneous reactivity in the case of slow grafting

We have used the light reflectivity microscope to follow the generation of thin nitrophenyl, NP, layers during the electrografting of the NBD salt on a gold microdisk electrode with a 250µm diameter. The optical setup is versatile enough to be used with simple home-made microelectrode, which is actually impossible so far with any other competing techniques (QCM, SPR). We confirmed on such microelectrodes, as was presented in the previous chapter, that the electrografting process proceeded in a similar mode (same grafting or electron transfer efficiency) than on larger electrodes. This was obtained from averaging the light reflectivity measurement on a large number of pixels of the microelectrode. The observation of a microelectrode smaller than the optical field of the microscope allows to depicting local heterogenity, if any, associated with the electrografting process. As depicted in Fig 3.7 b), the variations of light reflectivity, associated to the microelectrode electrografting, were estimated at different positions on the microelectrode and, for example, along the diameter line represented in Fig 3.7 b).

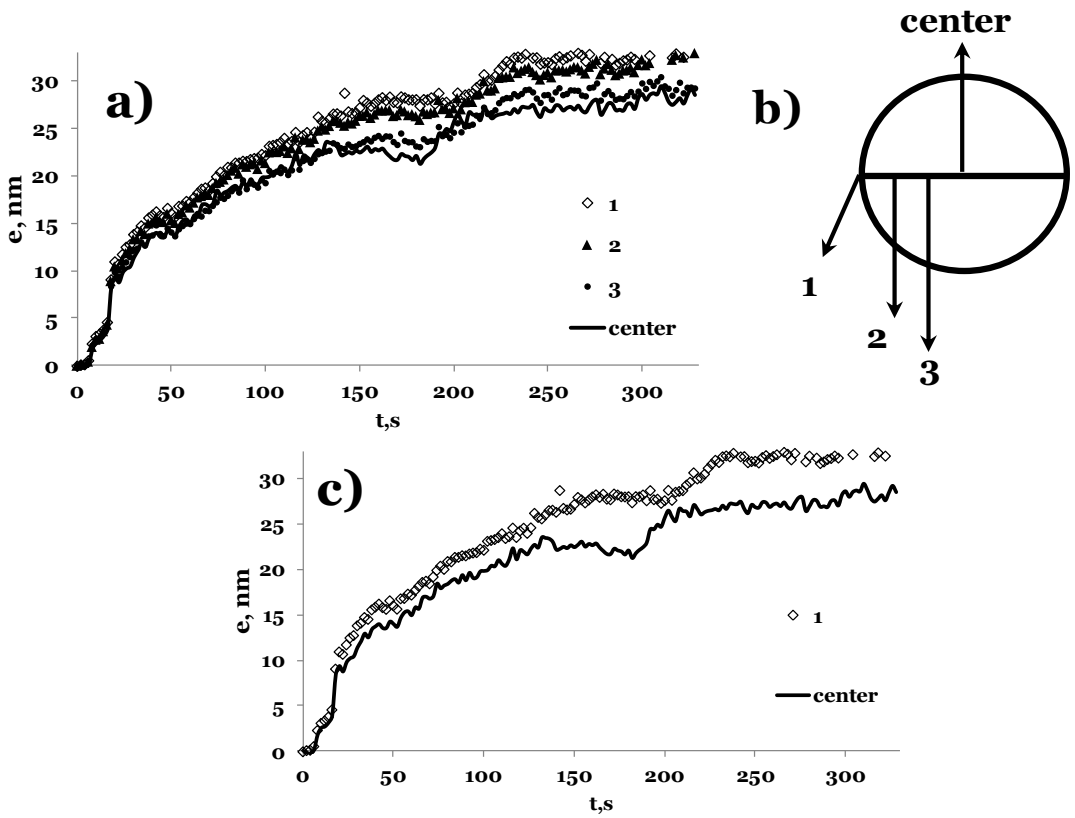

Figure 3.7 Variation (a,c) with time of the thickness of deposited NP film on different regions along the diameter line (b) of a microdisk electrode (∅=250 μm) for a chronoamperometric potential step between 0.5 and -0.7V vs Ag/AgCl during the electrografting of NBD (C=5 mM) in ACN + 0.1 M NBu_4BF_4; b) scheme presenting the chosen regions on the Au microdisk electrode for light reflectivity monitoring. The thicknesses are estimated from the light reflectivity measurements.

For thin NP layers, the small variations of the measured light reflectivity can be easily converted into thickness of grafted NP layer, as explained in Chapter 2. The local growth of the NP layer, as measured by the local light reflectivity change, with the electrografting time is presented in Fig. 3.7 a) for the 4 specified positions on the microelectrode diameter line. Clearly, for all positions, the NP film growth is similar: the grafting is initiated at t=20s and is associated for any position to a sudden thickness rise, another sudden thickness rise at t=200s is also observed on all electrode positions. This is actually consistent with the fact that an electrochemical process is operating as all electrode regions are actuated.

However, the extent of the grafting is clearly dependent on the position of the microelectrode under analysis. For any electrografting time t>20s, a higher thickness is deposited at positions closer to the edge of the electrode (going from center to 3, 2 and 1 in Fig 3.7). This indicates that the electrografting proceeds at different rates depending on the position on the electrode. If only the border region and the center of the microdisk electrode are compared, as in Fig. 3.7.c), for example for a time of 50s, a 16 nm thick layer is grafted on the edge of the electrode while a 14 nm thick layer is grafted in its center. The grafting is then 1.15 times more rapid on the edge than in the center of the electrode. This phenomenon can be interpreted as a result of the differences in current densities expected over the different regions of the microelectrode. As the current density is higher on the microelectrode border, a higher flux of generated radicals is expected to reach the microelectrode border than its center. This higher flux of radicals may explain that the organic layer deposition is more rapid and form faster the NP coating on the electrode edge.

Despite the difference in diffusional fluxes arriving at the edge or at the center of a microelectrode, the difference in deposition rate (a factor of 1.15) is much smaller than the almost one order of magnitude expected. The observed value then also suggests that even though the grafting rate has been accelerated, the grafting efficiency is lower at the edge than in the center. It indicates that the higher flux of generation of radicals is also associated with a higher loss of these radicals in competing trapping routes.

III. 1. 2. Heterogeneous reactivity in the case of the fast grafting of thicker layer

The differences in the local reactivity observed in the low flux regime provided by electrografting at low overpotential are more exalted when more negative electric potentials are applied.

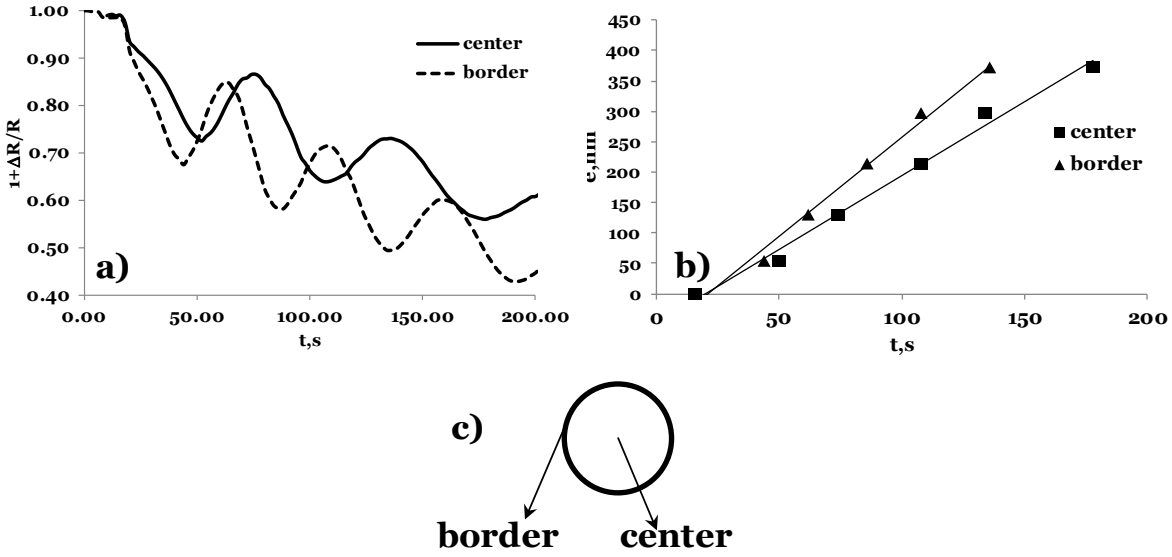

Figure 3.8 Variation with time of NP layer film growth at (c) different regions of a microdisk electrode (∅=250µm) during NP film growth by electrografting of NBD salt (C=5 mM) in ACN + 0.1 M NBu_4BF_4 for a chronoamperometric potential step between 0.5 and -1.1V vs Ag/AgCl. a) experimentally accessed local light reflectivity change, b) time evolution of the NP layer thickness estimated at the maxima and minima of a).

Fig. 3.8 presents the film growth evolution during the same microelectrode elecrografting at a constant potential of -1.1 V vs Ag/AgCl. As already described in the previous chapter, under these high overpotential, the light reflectivity presents oscillating waves, which are assigned to the formation of >150 nm thicker layers. Actually, the oscillations superimpose a gradual decrease of light reflectivity, which is assigned to both the formation of a light absorbing layer and the nanostructuration of the layer, so as to generate a medium that highly diffuses electromagnetic waves. In this particular case, it is difficult to obtain quantitative information about the evolution of the thickness of the layer. However, it was shown that the minima and maxima positions of the oscillating waves correspond to thicknesses equal to

$m\lambda/4n_{film}$ where m is an integer, λ is the illuminating light wavelenght and n_{film} is the real part of the refractive index of the layer (n_{film} = 1.5).

In this specific situation, an approximate growth kinetic of the layer is obtained from the time required for the occurrence of these extrema of light reflectivity. Inspection of Fig 3.8b then clearly confirms a faster growth rate on the edge of the electrode (the black line) than on its center.

From a quantitative point of view, as shown on Figure 3.8a, the occurrence of the initial minimum of reflectivity, which corresponds to the grafting of a NP layer of ~82 nm thickness, is observed for an electrografting time of 24 s on the border of the microelectrode, compared to the 33 s needed for the same deposition on the microelectrode center. The growth rate is then 1.3 times more rapid on the edge than in the center. The further delay in the film growth for the 2 selected regions on the microelectrode is still operating at longer electrografting time as one still records any characteristic extrema with a higher rate for the region at the border of the electrode (black line) than in the center of microelectrode (dashed line). This difference in growth rate is a litlle higher than that obtained at lower overpotential and then at lower generating flux of radicals (Fig 3.7). But still this rate ratio is low compared to what would be expected from comparison of theroretical diffusional fluxes in both regions.

III. 1. 3. Heterogeneous reactivity: Extension to other microelectrode systems

The observation of electrochemical heterogeneity related to the generation of heterogeneous fluxes of electro-active species was also observed in the case of other electrode formats that could present a behavior similar to microelectrodes.

It is the particular case of microcantilever platforms. Figure 3.9 presents a reflected light intensity image of a Au microcantilever platform, where cantilevers, like ‘jumpers’ in a ‘swimming pool’, are extended over a carved pool. They are 70µm long, 20µm wide and 0.84µm thick and have been obtained from specific carving of the pool by standard lithographic techniques.

The microcantilevers are then physically connected with the rest of the substrate (upper part of the image in Figure 3.9) and as the substrate is coated with gold, the overall substrate does not behave as a microelectrode. However, owing to the geometrical shape of the microcantilevers, the latter should behave as microelectrodes and sustain higher diffusional fluxes on their edge than on the rest of the macroscopic substrate.

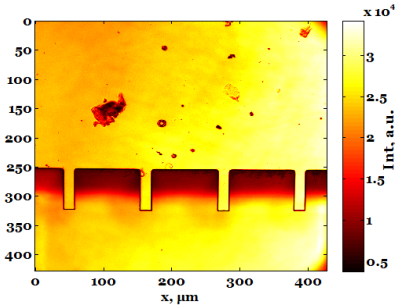

Figure 3.9 Light Reflectivity intensity image in air of a cantilever platform

If the electrografting of this platform with NBD of this platform is monitored, similar phenomena as described before are observed. In Fig. 3.10 images of a microcantilever platform at different instants during the electrografting of NBD are presented.

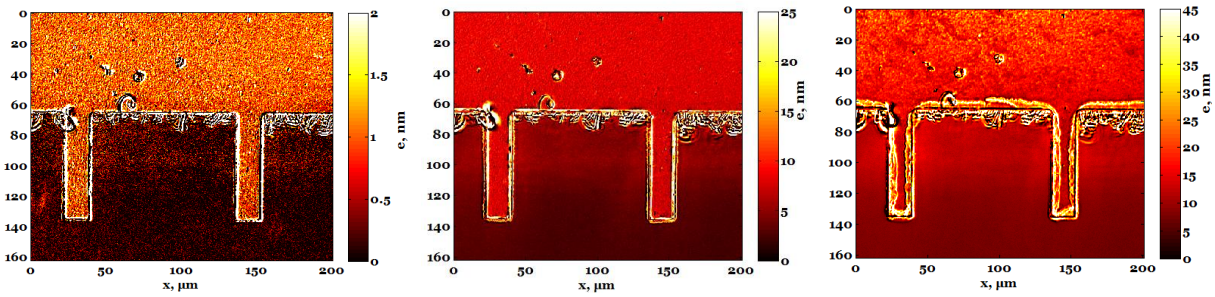

Figure 3.10 Layer thickness images estimated from light reflectivity images recorded during the electrografting of NBD, C=5 mM in ACN + 0.1 M NBu_4BF_4 for a chronoamperometric potential step between 0.3 and -0.7 V vs Ag/AgCl .

It can be observed that after only 8s of electrochemical activation, a deposition of the organic film can be evidenced. At this time, the layer deposited on the plain substrate of the platform has a thickness of the order of 1-2 nm, while a thicker layer is deposited (~5 nm) on the border of both the plain substrate and of the cantilevers.

The phenomenon of electrochemical heterogeneity due to difference in current density is clearly continuously observed during all the electrografting process. It is even more evident at the end of the electrografting process (at t= 200s) in Fig 3.10c, through the thicker film deposition onto the platform edges than onto the plain substrate.

IV. *Imaging local electrochemical reactivity - $Ar^{\bullet}$ reactivity compared to different species*

In a second approach we propose to image in-situ and in real time the local electrochemical or chemical reactivity of surfaces based on the observation of electrografting processes at patterned electrodes. Our objective is to detect how $Ar^{\bullet}$ radicals electrogenerated during an electrografting process are reacting at surfaces locally functionalized with different chemical species, as shown in Fig. 3.6.

Our strategy is based on the comparison of the reaction of $Ar^{\bullet}$ toward different species present on a same surface. This study is then based on the observation of $Ar^{\bullet}$ reaction at surfaces patterned with different chemical functionalities. As presented in Chap II, light reflectivity is a pertinent tool to inspect in situ and in real time the growth rate of an organic layer from a surface. By comparing the grafting efficiency of different diazonium salts under different electrografting conditions (potential), it allowed an indirect inspection of the apparent reactivity of electrogenerated radicals toward a bare gold surface (during the initial grafting stage) or toward an aryl layer (during the continuous multilayer growth). The same strategy is used here and we expect, by observing the growth rate of aryl layer on differently functionalized surfaces, to depict the reactivity of $Ar^{\bullet}$ toward different chemical substances.

Surfaces patterned with chemical structurations is a prerequisite to this study, they have been prepared as presented in section II. Dedicated functionalizations are specifically introduced on or removed from a surface, respectively by using μCP or photolithography (UV then plasma).

IV. 1. *Heterogeneous reactivity at Au surfaces patterned by µCP*

IV. 1. 1. Heterogeneous reactivity at Au surfaces stamped with thiols

First, we have monitored the electrografting of NBD on surfaces stamped with a thiol. Fig. 3.11 presents the final image of the grafting representing the distribution of the grown NP layer thickness over the surface. The darker areas reproduce the square pattern of the stamp. Outside these square areas, a 5 to 6 nm NP multilayer was grown during the electrografting process. However, within the square areas where thiols were imprinted, an organic layer also grew but in a twice thinner (about 3 nm) layer.

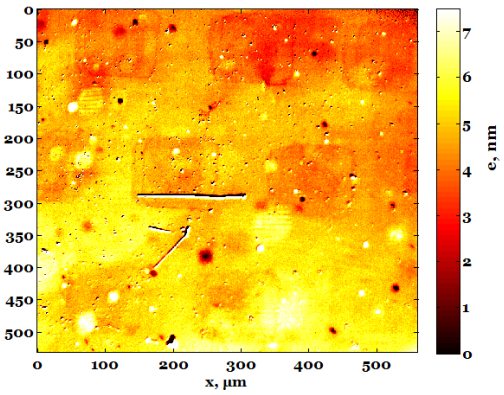

Figure 3.11 Estimated image of the distribution of the thickness of a NP layer grown from the electrografting of NBD (C=0.01 M) in H_2SO_4 (C=0.01M) on a µCP printed Au surface with 1-decanethiol (C=0.01 M) by 100x100 µm² stamps spaced by 100 µm, for a chronoamperometric potential step between 0.5 and -0.4 V for 300s.

This suggests that the electrografting also operated on the stamped zones, even though they are covered with an organic moiety. Different explanations may be proposed. First, as observed in section II, the thiol deposition by µCP is heterogeneous and leaves some pinholes in the stamped layer from which diazonium reduction and radical $Ar^{\bullet}$ can be generated, making possible the film growth. Second, the electrografting process, even though it is not operating under highly reductive

conditions, may lead to desorption of the adsorbed thiol, liberating the Au surface for successive film growth. Finally, one could envision that the electrogenerated radical may react chemically with the thiols and from hydrogen abstraction and radical coupling reactions, may allow the grafting of NP layer on top of the thiol one. In any case, such experiment depicts the reactivity of the $Ar^{\bullet}$ radical in differently chemically structured environments.

IV. 1. 2. Heterogeneous reactivity at Au surfaces stamped with BSA

The radical reactivity was then analyzed within thin layers of other species, as biological molecules, in our case, bovine serum albumine (BSA). The BSA was also transferred to the surface by μCP. This time, the Au surface was printed using a PDMS stamp, which consisted of 24 μm diameter disks spaced by 240 μm. The image of the distribution thickness of the deposited NP layer at the end of the electrografting of the NBD salt process is presented in Fig. 3.12. In this figure, dark disks with the expected diameter and spacing are found as region of lower thicknesses (2nm), but another periodic structure is also observed: a larger ring (60μm outer diameter) of higher thickness (>5nm) surrounds each stamped disk.

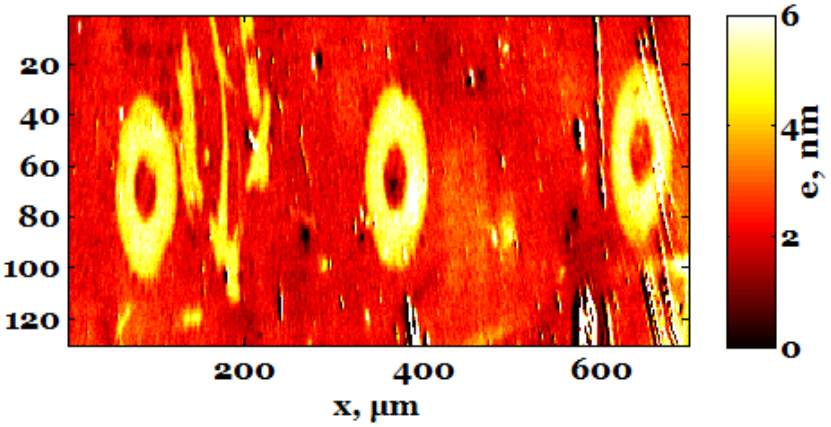

Figure 3.12 Estimated distribution of NP layer thickness obtained from the electrografting of NBD **(**C=10 mM) in ACN + 0.1 M NBu_4BF_4 on surfaces printed with BSA (C=80μg/mL) during a chronoamperometric potential between 0.5 and -0.4V vs Ag/AgCl for 300s.

Outside these structures, the substrate is also a domain of lower thicknesses (2nm), which may seem contradictory as it behaves as the stamped disk while it was expected that it would behave as the rings. This phenomenon may be interpreted as a possible stamping of BSA outside the rings. As the inter-pillar dimension of the stamp is large, compared to the pillar dimension, the observed external circumferences results from a too high mechanical pressure applied on the stamp and a collapse of the stamp roof on the Au surface.

The phenomenon is explained in Fig. 3.13.

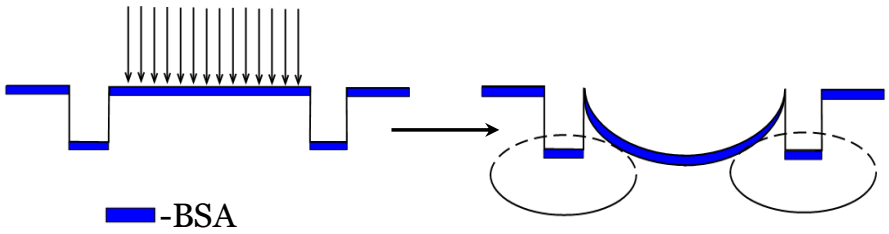

Figure 3.13 Diagram for the formation of external circumferences by roof collapse around the stamped blocks during μCP.

This means that, the BSA was transferred to the entire printed surface except within the observed rings. As noticed with stamped thiols, even if the surface is covered with BSA, the electrografting can be activated in these covered regions and a 2-3 nm thick organic layer was deposited.

As the BSA covers almost all the available Au surface except the rings surrounding the disk patterns, it is not possible to envision that the radicals are generated only in uncovered regions (the rings) and transported over the whole substrate. Moreover, the complete desorption of BSA upon the potential application was not observed: as will be shown later, its infra-red signature is still present after the electrografting procedure. This experiment then suggests that in the stamped regions the diazonium is likely reduced along defects of the stamped layer. These defects are likely nanochannels available for species transport to uncoated Au. They will provide sources of radicals over the whole stamped region. It is expected that they will be filled by NP layer during the grafting process; however the reaction of the radical with the immobilized organic moieties (BSA, thiols, etc…) is not eliminated.

IV. 2. *Heterogeneous reactivity at Au surfaces patterned by photolithography*

To confirm that $Ar^{\bullet}$ radicals are generated through the defect sites of the pre-immobilized moieties, we have inspected the reactivity of $Ar^{\bullet}$ on surfaces patterned by UV-lithography. Indeed, in this approach, photolithography allows removing the immobilized moieties in small areas. Moreover, the quality of the moieties immobilization could be optimized, for example by higher adsorption times and conditions not accessible in μCP experiments. However, this photolithographic technique is more time consuming as a larger number of steps and more frequent accesses to cleanroom facilities are needed. Therefore, photolithography was tested in the case of thiols and diazoniums only.

IV. 2. 1. Heterogeneous reactivity at lithographed thiol Au surfaces

An Au wafer surface was left for 24h in a thiol solution (or pre-electrografted with NBD), prior to UV-lithography. The UV-lithography consisted in removing locally the organic layer (thiol or NP layer), on circular zones of 12 μm, spaced by 120 μm. The reactivity of $Ar^{\bullet}$ was then monitored.

Fig. 3.14 presents the results obtained after the electrografting of NBD, on a thiol patterned surface. Here again, the deposition of the NP organic layer is observed on the entire surface, confirming that electrografting may proceed through defects of the adsorbed layer. However in this figure, a thinner layer of NP is detected in the regions, where the thiol layer was supposedly removed (red disks), and where the reactivity was expected to be higher. This highlights the possible change of reactivity introduced by the plasma treatment as was postulated in section II.

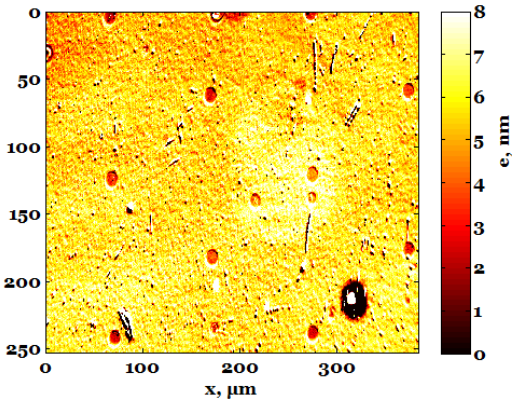

Figure 3.14 Estimated distribution of deposited NP layer thickness resulting from the electrografting of NBD, C=0.01 M in ACN +0.1 M NBu_4BF_4 on Au surface initially modified by 1-decanethiol (C=0.01M) and then modified by UV-lithography, for a chronoamperometric potential step between 0.3 and -0.45 V vs Ag/AgCl for 300s

IV. 2. 2. Heterogeneous reactivity at lithographed NP covered Au surfaces

The same phenomenon was observed for the same UV-lithography modifications conditions of Au surface, which was initially grafted with NBD. In this case, by UV-lithography, the grafted NP layer was etched along a pattern consisting of circles of 24 µm diameter disks spaced by 120 µm. As seen in Fig.3.15, after electrografting of this patterned surface, a deposited film of thickness between 6-8 nm was observed on the entire surface, confirming the possibility of further grafting on an already initially deposited NP film.

Moreover, the etched regions, inside the red disks, are again less reactive than the rest of the surface since a thinner film is deposited inside them, again in contradiction with our initial assumption.

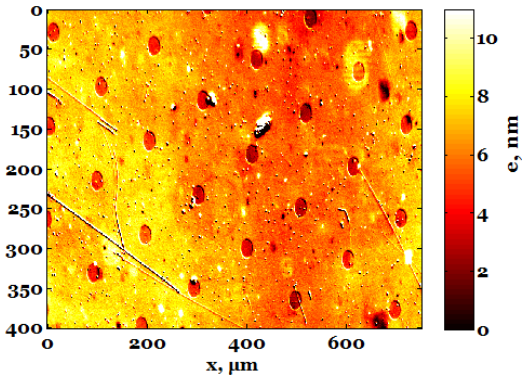

Figure 3.15 Estimated distribution of deposited NP layer thickness resulting from the electrografting of NBD C=0.01 M in ACN +0.1 M NBu_4BF_4 for a chronoamperometric potential step between 0.3 and -0.45 V vs Ag/AgCl for t=300s, on an Au surface previously grafted ex-situ with NBD and then locally patterned by UV-lithography.

At this stage, a more detailed analysis of the effect of O2 plasma irradiation on surface reactivity is needed. We assigned the Au passivation of the irradiated regions to the possible deposition of oxides resulting in a change of the optical response.

IV. 2. 3. Influence of the photolithography etching time on the Au structuration

In the two previous examples, the duration of the final etching step of RIE (reactive ion etching), which is expected to remove the adsorbed species in the areas non-protected by the photoresist, was 3.5 min. For such long RIE time, the light reflectivity images of the patterned surface also clearly show the presence of the pattern indicating that the RIE induces not only the etching of the thiol (or the NP layer) but also seriously affects the optical properties of the underlying Au surface. Chemical structuration may be invoked such as the formation of gold oxides. It could also be accompanied by a physical re-structuring of the Au surface.

A single pattern has been characterized by AFM. The corresponding image is given in Fig 3.16 along with its diameter profile.

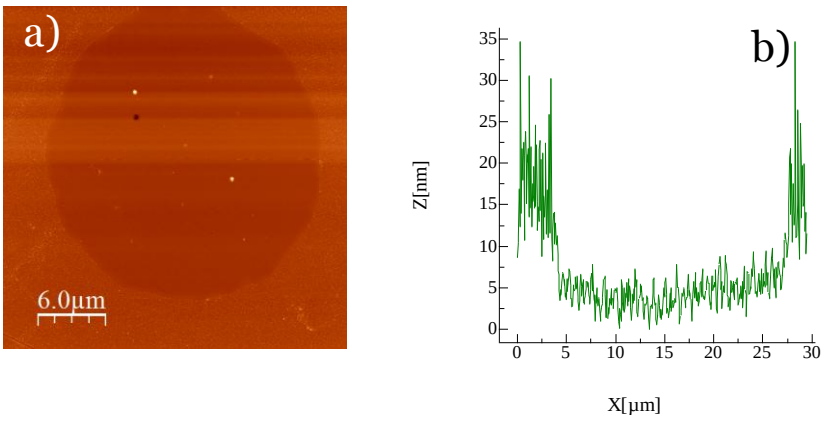

Figure 3.16 a)AFM image of a single pattern (∅ = 24 µm); b) diameter profile of the analyzed spot;

Owing to the higher depth of the patterned region, this AFM characterization clearly shows that at such long RIE time, even the Au surface is etched.

The duration of the RIE has then been reduced. After a 2min RIE treatment of a decanethiol monolayer adsorbed on Au, the patterned electrode was submitted to NBD electrografting. The corresponding surface on which selective deposition of NP layer was examined by light reflectivity microscopy, is depicted in Fig 3.17. We obtain the expected surface reactivity response towards the $Ar^{\bullet}$ radicals formed when electrografting NBD.

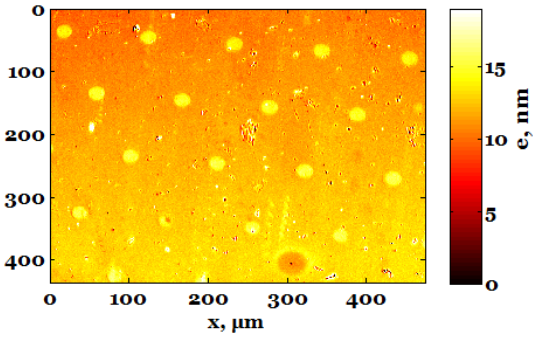

Figure 3.17 The deposited layer thickness after the electrografting of NBD C=0.01 M in ACN +0.1 M NBu_4BF_4 for a chronoamperometric potential step between 0.35 and -0.6 V vs Ag/AgCl for 300s, on an Au surface modified initially with 1-decanethiol (C=0.01 M) and then locally modified by UV-lithography; RIE time:2 min.

Periodic patterns of 24 µm diameter disks spaced by 120µm are clearly visible in this image, as expected from the used photomask. Moreover, in the disks, the areas exposed to the RIE, where the thiols have been etched and where bare Au should have been recovered, a thicker NP layer (15 nm) is grafted comparatively to the external thiol-covered substrate (10 nm). In this example, the reactivity of $Ar^{\bullet}$ is more important on the recovered Au disks, in agreement with the retarding effect of the thiol acting as a barrier to electron transfer.

Here also, a more negative potential was used for the electrografting process (-0.6V instead of -0.45 V vs Ag/Ag^{+}) which should increase the NP growth rate but also should favor the desorption of the thiol. The NP layer on the thiol-protected substrate has a thickness of about 10-11 nm, which is only slightly higher than the 7nm observed in Fig 3.15 at -0.45V. It then suggests that even at this negative potential the electrochemical thiol desorption, if operating, is a process with kinetics comparable or slower than the NP growth process.

IV. 3. *Summary*

At this stage, we have combined surfaces patterned with given chemical moieties and in-situ light reflectivity microscopic inspection of electrografting processes. This was used to study the selective grafting of an aryl layer from reaction of an electrogenerated aryl radical on various chemical environments. The light reflectivity microscopy demonstrated at least that surface patterning should be handled with care for surface reactivity studies. The diazonium electrografting is an interesting model reaction as it allows the follow up of a multilayer build-up on a surface upon electrochemical activation. In principle, it allows inspecting the multilayer growth rate then relating it to the surface reactivity. It showed that patterned surfaces obtained by standard lithographic procedures may not behave as ideally prepared macrosurfaces. It revealed the heterogeneity of the deposition (for µCP), but also the chemical or physical restructuring upon plasma treatment (oxide formation or Au etching upon RIE) which may impart the patterned surface with odd reactivity.

The case of NBD electrografting on patterned surfaces also demonstrated that grafting may occur even on 'expected' blocking layers, evidencing the porosity of these layers to solution and solutes. This was demonstrated from the possible growth of an aryl layer on surfaces covered by different organic moieties, showing an imperfect passivating or blocking layer.

This supposed blocking layer actually presents a retarding effect for the electrografting process. At this stage it is not clear whether this retardation is due to prior desorption in the case of thiol, limiting mass transfer within the porous structure, or to a lower reactivity as radicals have first to couple to the pre-adsorbed organic layer. Even though this work has still unanswered question, it definitely provided an interesting way of examining the chemical and electrochemical reactivity of surfaces.

V. *Aryl diazonium layer – a blocking film for biological interactions*

In biomedical domains, the control of the spontaneous adsorption of proteins on hydrophilic surfaces is an important concern [3]. However, non specific adsorption of proteins can causes undesirable phenomena like altering the results of bioassays based on a specific ligand/receptor recognition interaction. These undesired effects can be minimized or even the surface can be inhibited for biofouling using various surface passivating treatments, with for example different polymers, such as poly (ethylene oxide) PEO[4], poly(ethyleneglycol) PEG[5, 6], polyvinyl pyrrolidone (PVP)[7], pluronic[8]. In the previous section, we have shown that a NP layer could be grown on or within a BSA coated Au surface by NBD electrografting.

Here, we wish to observe what was the impact of the grown NP layer on the biochemical activity of the pre-immobilized biological material. This investigation should also propose an alternative method of preparation of antifouling surfaces to prevent biofilm formation (by bioactive species) on surfaces.

In order to inspect the alteration of the biochemical activity of a surface-immobilized biomaterial, we propose to engage the biomaterial into biomolecular recognition processes. Our strategy is then based on the preparation of heterogeneous immunoassays surfaces and the observation to what extent the NBD electrografting alter the immunoassay response. First, heterogeneous immunoassays were prepared by surface-immobilization of a bioactive species. Then the immunoassay performance was quantified via the biomolecular recognition of the anti-bioactive (complementary) species present in solution.

This performance of the biological recognition step was assigned from different techniques: fluorescence microscopy when using fluorescent biochemical probes and IRRAS (Infrared Reflection Absorption Spectroscopy) for the inspection of the biomaterial integrity.

Two couples were selected: BSA/sypro and lysozyme/anti-lysozyme. The first couple concerns the indirect recognition of BSA (bovine serum albumine) by sypro, which is a fluorescent probe for lipophilic environment and is therefore a highly sensitive, and ready-to-use fluorescent stain for proteins. This probe was used to evaluate the hydrophobicity of the environment generated through the aryl layer grown by diazonium electrografting.

V. 1. *Grafting NP layer on BSA patterned surfaces*

As previously described, an Au surface was patterned by μCP with BSA, then submitted to NBD electrografting. The stamp used was made of 100μm² squares spaced by 100μm. When left in contact with a sypro solution, the BSA patterns are revealed by epifluorescence microscopy as fluorescent (bright) squares. An example is shown in the upper part (C_a) of Fig 3.18. The presence of the BSA was also confirmed by IRRAS spectroscopy. Figure 3.18 a) presents the IRRAS spectrum of a BSA coated surface. It shows two characteristic bands at 1674 and 1545 cm^{-1} that are assigned to amide (I) and amide (II) groups characteristics of proteins and here of BSA.

Then, (half of) the BSA patterned Au surface was submitted to NBD diazonium electrografting for the NP deposition. The IRRAS analysis of the electrografted part of the substrate is given in Fig.3.18 (b). T

The fingerprint of the NP layer is evidenced through the appearance of the aryl-NO2 bands at 1530 and 1350 cm^{-1} respectively. The amide (II) band at 1545 is now difficult to distinguish from $\upsilon^{as}NO2$ (1530 cm^{-1}*)*. The amide (I) band of BSA is still present but the peak appears as a doublet due to a slight shift of the band (from 1674 to 1690 cm^{-1}) which could suggest a possible denaturation or conformational change of the protein. This was already observed by Y.L. Jeyachandran et *al.* assigning the shift of the amide bands to the changes in the secondary structure of the protein molecules after their adsorption[9]. However, the IRRAS analysis confirms that upon the electrografting process, the BSA has not been desorbed from the surface, as the overall amide (I) band integration is similar to that detected before the electrografting process.

The electrografted substrate was also submitted to a sypro solution and observed by fluorescence microscopy. Fig 3.18 (C_b) shows the characteristic fluorescence image recorded for the substrate region of the interface formed by the electrografting solution meniscus. It can be clearly seen that the fluorescence response of sypro on the stamped BSA regions (C_a) is still visible on ungrafted (upper) region, while the fluorescent patterns have disappeared (in the lower region - C_b) after the NP electrografting. The sypro test actually only reveals that the grafted region has lost its hydrophobic nature. It suggests that the NP layer inhibits the hydrophobic interaction between the sypro and the BSA. Further experiments showed that sypro did not either interact with NP films, evidencing the partial hydrophilicity of the NP layer. It is quite unlikely that the possible conformational change induced by the electrografting process has altered the hydrophobicity of the BSA. It is then rather suspected that the NP layer grown around or within the BSA has changed its physico-chemical environment. The hydrophilic environment provided by the NP layer may actually alter the hydrophobic interaction between BSA and sypro. This also suggests that the NP layer may then act as an antibiofouling layer by introducing a slightly hydrophilic environment on a surface.

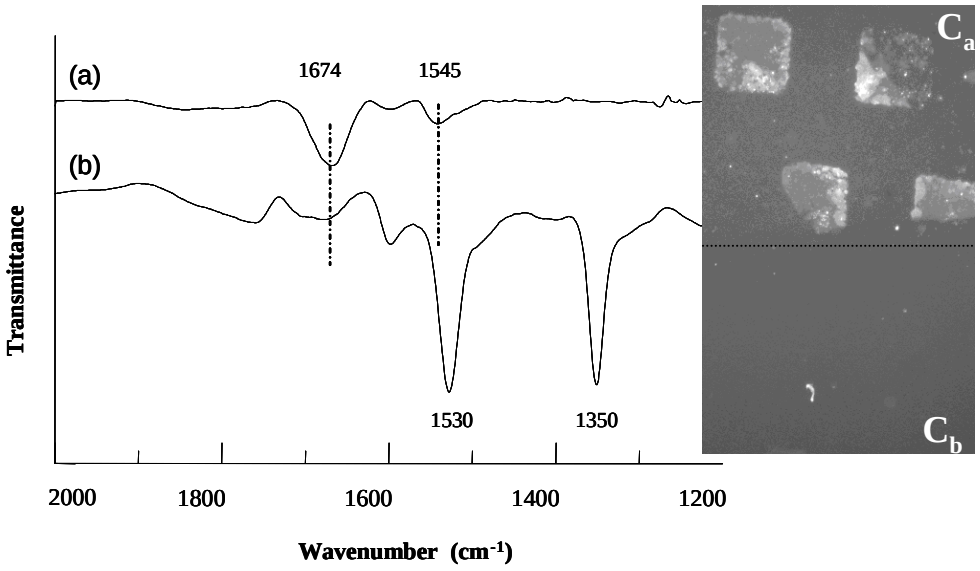

Figure 3.18 IR spectra of adsorbed BSA on Au surface before (a) and after (b) deposition of blocking NP layer. The insert (Ca, Cb) is the fluorescence response of sypro on (a) and (b) surface.

V. 2. *Grafting NP layer on lysozime patterned surfaces*

We have just shown that the NP layer changes the environment of biomolecules. In a next step, we will evaluate its impact on a specific interaction. We then tested the impact of NP layer growth on a second biochemical couple: the lysozyme and its complementary anti-lysozime (lyso/anti-lyso). Lyso is a small peptide comprising typically 129 amino acids. Its complementary anti-lyso was a fluorescent labeled aptamer, which allowed detecting the lyso/anti-lyso interaction by fluorescence microscopy. This couple was chosen because both components are commercially available.

Figure 3.19 presents the IRRAS spectra of a Lyso-immobilized Au surface before (Fig.3.19 a) and after the diazonium aryl layer deposition (Fig.3.19 b). The presence of the bands centered at 1687 and 1553 cm^{-1} corresponding to amide I and amide II, respectively, validate the successful immobilization of lyso on the Au surface. After the electrodeposition of the NP film, as observed with BSA, the amide II band is again masked by the $\upsilon^{as}NO_2$ (1530 cm^{-1}) of the aryl-NO_2 bond, even though a shoulder in the NO2 band might correspond to the amide II band.

The amide I band was also shifted to lower frequencies by roughly 10 cm^{-1}. Again, this difference is attributed to a change of conformation or orientation of the lyso structure[10]. The fluorescence response of the lyso surface incubated with a fluorescent labelled anti-lyso aptamer, after the deposition of the NP layer is presented in Fig. 3.19, C_b. It shows that, unlike for the BSA, the lyso/anti-lyso recognition is still observed after NP layer growth. Indeed, the squares of the PDMS stamp are slightly recognized. It then suggests that even though the NP layer growth induces a possible change of the peptide conformation, it has not affected much the biomolecular interaction step.

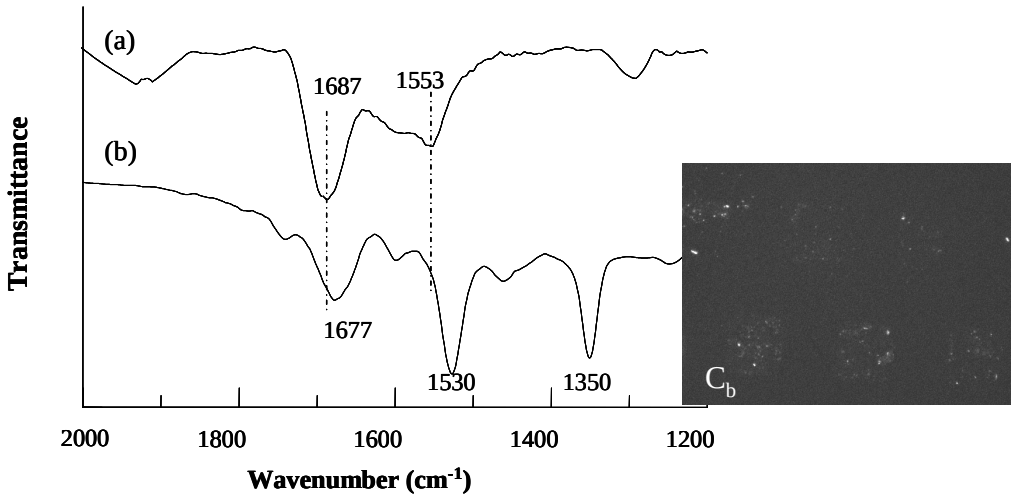

Figure 3.19 IR spectra of adsorbed lyso on Au surface before (a) and after (b) deposition of the blocking layer; C_b –the fluorescence response of lyso Au surface incubated with a fluorescent labeled anti-lyso aptamer.

This section presented a preliminary investigation on the use of NP layer and NBD diazonium electrografting as ways of preparing antifouling surfaces along with the possibility of controlling the local (bio)-chemical reactivity.

Conclusions

The applications of reflectivity measurements for imaging chemical surface structurations or local chemical reactivity were shown. The simplicity of detecting surfaces structural modifications with a high sensitivity in air using reflectivity measurements was confirmed. The heterogeneity of the chemical reactivity due to differences in current densities was shown on surfaces with different geometries and dimensions. The $Ar^{\bullet}$ reactivity was studied toward different organic (NP or thiol) and biological (BSA) species on locally modified surfaces, either by μCP or UV photolithography techniques. The principle was validated, confirming that the optical imagery can be applied to study the reactivity of different molecules towards various species. More studies should be carried out to clarify the phenomena related to the electrografting onto surfaces with preadsorbed layers of thiols.

We propose an alternative method to prepare antifouling surfaces, using the deposition of polyaryl layers on electrode surfaces by electrochemical reduction of aryl diazonium salts. It is shown that this organic layer may block the recognition between bioactive and anti-bioactive species on such decorated surfaces. Moreover, these strongly attached organic moieties can be used to improve (or change) the hydrophilic or hydrophobic nature of the biochemical surface.

References

1. Ruiz, S.A. and C.S. Chen, *Microcontact printing: A tool to pattern*. Soft Matter, 2007. **3**(2): p. 168-177.
2. Xia, Y.N. and G.M. Whitesides, *Soft lithography*. Annual Review of Materials Science, 1998. **28**: p. 153-184.
3. Cox, J.D., et al., *Surface passivation of a microfluidic device to glial cell adhesion: a comparison of hydrophobic and hydrophilic SAM coatings*. Biomaterials, 2002. **23**(3): p. 929-935.
4. Lou, X.H. and L. He, *Surface passivation using oligo(ethylene glycol) in ATRP-assisted DNA detection*. Sensors and Actuators B-Chemical, 2008. **129**(1): p. 225-230.
5. Kenausis, G.L., et al., *Poly(L-lysine)-g-poly(ethylene glycol) layers on metal oxide surfaces: Attachment mechanism and effects of polymer architecture on resistance to protein adsorption*. Journal of Physical Chemistry B, 2000. **104**(14): p. 3298-3309.
6. Bearinger, J.P., et al., *Chemisorbed poly(propylene sulphide)-based copolymers resist biomolecular interactions*. Nat Mater, 2003. **2**(4): p. 259-264.
7. Lou, X.J., et al., *Increased amplification efficiency of microchip-based PCR by dynamic surface passivation*. Biotechniques, 2004. **36**(2): p. 248-+.
8. Luk, V.N., G.C.H. Mo, and A.R. Wheeler, *Pluronic additives: A solution to sticky problems in digital microfluidics*. Langmuir, 2008. **24**(12): p. 6382-6389.
9. Jeyachandran, Y.L., et al., *Efficiency of blocking of non-specific interaction of different proteins by BSA adsorbed on hydrophobic and hydrophilic surfaces*. Journal of Colloid and Interface Science, 2010. **341**(1): p. 136-142.
10. Thakur, G. and R.M. Leblanc, *Conformation of Lysozyme Langmuir Monolayer Studied by Infrared Reflection Absorption Spectroscopy*. Langmuir, 2009. **25**(5): p. 2842-2849.

Chapter 4 :Ellispometric imagery – a tool to study in-situ and real time surface modifications

I. *Introduction*

As was demonstrated in the previous chapters of this thesis, it is important to develop analytical tools that are able to determine in situ and in real time the local chemical changes associated the chemical reactivity of surfaces and interfaces. If the principle of detecting changes in light reflectivity at a reflecting surface is used in numerous techniques, the most direct and informative one in surface science is likely ellipsometry. It is typically as a routine tool for the characterization of surface coatings and etching in the silicon-based microelectronic and related processes.

Its large interest comes from the use of a very simple operating optical setup using a light source, associated with a polarizer/analyzer couple and a detector. As described in the bibliographic review in Chapter 1, and based on the popularity of ellipsometric measurement, imaging systems based on ellipsometric measurement have been also proposed. The building of different configurations of an ellipsometer imaging setup was started, as mentioned before, with the development of the instrument in the Beaglehole ‘s group [1]. Despite of the possibility of reading the ellipsometric parameters, the obtained image using this setup was out of focus in some regions as the image plane is not perpendicular to the direction of the reflected light. This default was corrected by Hénon and Meunier[2], by mechanically shifting the object lens, and collecting light only from the focused regions, with a final reconstruction of the image. By correcting the defocusing problem, the long duration for scanning the sample and image reconstruction was still a disadvantage.

The highest lateral and thickness resolution was obtained using a different configuration from the PCSA setup (polarizer, compensator or retarder, specimen, and analyzer) developed by Neumaier *et al.*[3]. It allows focusing of the full field of view, due to the fact that light beam is focused into the back focal plane of an infinity corrected high-power microscope objective. In this case, the object placed in the front focal plane of the objective is illuminated with a parallel beam of polarized light under a shallow angle.

However, so far absolute optical measurement of a surface is still difficult with such imaging setup, explaining why imaging ellipsometry has not yet emerged as an essential surface science tool.

As already stated, the constant objective of my work is to propose alternative imaging techniques allowing the versatile, in situ and real time follow-up of chemical transformation of a wide range of surfaces and interfaces. Ellipsometry is likely a pertinent technique as it had been used to characterize a wide range of surfaces and interfaces (air/liquid, air/solid, liquid/solid). We then propose in this chapter to develop an experimental setup, allowing for the ellispometric imagery of surfaces. The chapter describes the experimental setup proposed and tests its performances as both an ellipsometric and an imaging device. Its capabilities are then validated in the in-situ and real time monitoring of surface modification. This is illustrated as already presented in the case of the follow-up of the electrografting of Au surfaces by diazonium salts.

II. *Experimental setup*

In this work, we built an imaging ellipsometric setup, based on the Neumaier *et al.*[3] configuration for applying to in situ and real time monitoring of surface modification. The experimental setup used during our measurements is illustrated in Fig. 4.1.

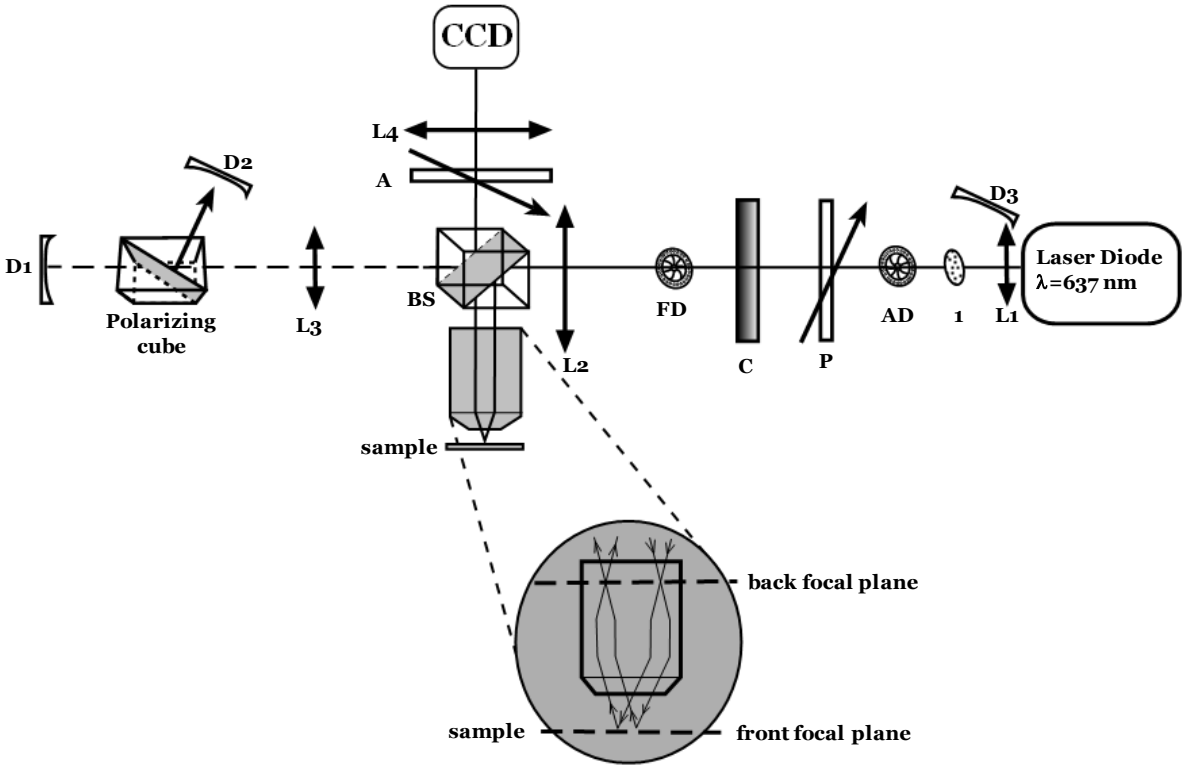

Figure 4.1 Setup of the ellipsometric microscope: AD-aperture diaphragm (iris diaphragm); P-polarizer at 45°; C – used as Babinet-Soleil compensator or liquid crystals variable retarder (Meadowlark); FD-field diaphragm; 1- spinning ground glass diffuser; BS – beam splitter; D1, D2,D3 – photodiodes; A – analyzer; L1-L4 – lenses.

Actually, previous similar optical setups were shown to give confident relative variation of Ψ and Δ but not true absolute values. We will more particularly seek quantitative information from relative variations of the ellipsometric angles Δ and Ψ. In order to perform sensitive ellipsometric measurements a laser light has to reach the sample surface with an incident angle as large as possible.

Typical ellipsometers work with incident angle in the range of 60-70° angle of incidence (vs. the normal incidence) provided by the mechanical displacement of the laser light source and of the photodetector. In an optical microscopic version of ellispometry, an infinity-corrected high-numerical aperture microscope objective is used to achieve angles of incidence large enough to perform sensitive ellipsometric measurements : - a Nikon, x50, NA=0.95, W.D=0.35 in air, - an Olympus, x 60, NA=1.1 with an index variation correction collar in liquid. When the light source beam axis is off-centered from the optic axis of the objective, maximum angles of incidence of 54° in air and 45° in a liquid, with a beam divergence of ± ~2.5° can be obtained. The light source is a laser diode at 637 nm wavelength, with 250 mW CW (continuous wave) optical output power.

A rotating diffuser is used to reduce diffraction and interference effects in the image due to the coherence of the laser source. A diaphragm – AD, located near the diffuser is conjugated with the back focal plane of the objective. The aperture and angle of incidence of the beam hitting the sample surface are controlled by the diameter and the lateral position of this diaphragm image. A polarizer P, oriented at 45°, coupled with a Meadowlark liquid crystal variable retarder (LCVR), with axis parallel to the p and s components produce the state of polarization of the incident wave. This is then analyzed on the second beam transmitted through the non polarizing beam splitter cube BS. The photodiodes D1, D2 measure the intensities of the components, parallel and perpendicular to the polarizer direction, which are separated by a polarizing beamsplitter cube. The D3 photodiode is used to measure the intensity of diffuse light from the laser diode, for normalizing the measured intensities by the photodiodes D1 and D2, in order to compensate the fluctuations of the source.

The measured signals are used for the identification of the phase shifts induced by the LC variable retarder. A calibration is first performed using a Babinet-Soleil compensator as retarder. The light collected by the objective passes through an analyzer A parallel to the polarizer P. Finally the sample surface is imaged onto a CCD array (DALSA, 256x256 pixels, 8 bits). Four images are captured with four different phase shifts of the variable retarder, distributed within [0, 360°] range (70°, 160°, 250°, 340° for instance) in order to obtain an ellipsometric image.

To improve the sensitivity of the acquisition, we have accumulated 16 images at a frequency of 80 Hz, which make a total duration of 2.6 s for recording one ellipsometric image.

III. *Image processing*

III. 1. *Calibration*

The full system is first calibrated using a fairly reflective surface (gold) and introducing N_c well defined phase shifts δ_n^c, $n \in \{1 \dots N_c\}$. Images I_n^c as well as signals $i_{\parallel}^c(n)$, $i_{\perp}^c(n)$, $i_t^c(n)$ coming from the photodiodes are acquired for these shifts as shown in fig. 4.2.

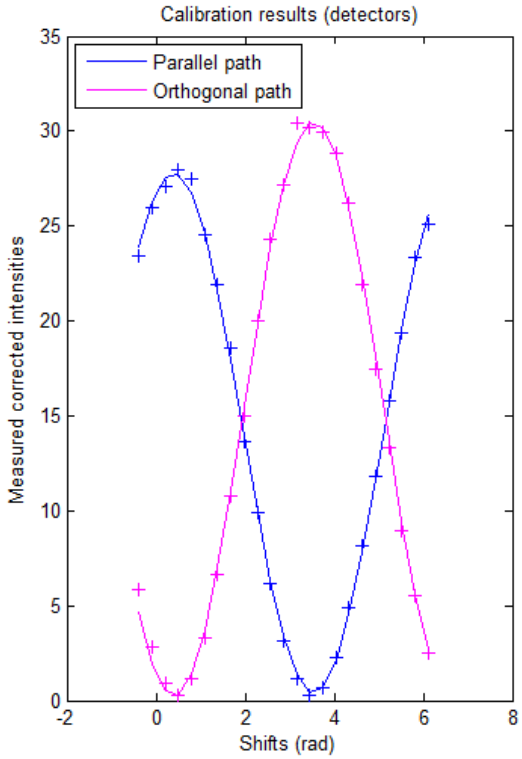

Figure 4.2 The best fit for measured and normalized intensities (+) for imposed Nc phase shifts values (23, in our case) for the parallel (blue line) and orthogonal (red line) path used to obtain $\boldsymbol{i_{\parallel}^c(n)}$, $\boldsymbol{i_{\perp}^c(n)}$ from relation (1).

The $i_t^c(n)$ - is the signal which comes from a third diode, used for the normalization of the signal for the parallel and perpendicular components to the polarizer direction, as in (1). The photodiodes signals are assumed to read

$$\begin{aligned}\frac{i_{\parallel}^{c}}{i_t^c}(n) &= i_{\parallel}^{0} + i_{\parallel}^{s}\sin\,\delta_n^c + i_{\parallel}^{c}\cos\,\delta_n^c = i_{\parallel}^{0} + i_{\parallel}^{\star}\cos\left(\gamma_{\parallel} + \delta_n^c\right)\\ \frac{i_{\perp}^{c}}{i_t^c}(n) &= i_{\perp}^{0} + i_{\perp}^{s}\sin\,\delta_n^c + i_{\perp}^{c}\cos\,\delta_n^c = i_{\perp}^{0} - i_{\perp}^{\star}\cos\left(\gamma_{\perp} + \delta_n^c\right)\end{aligned} \tag{1}$$

The signals recorded during the calibration procedure are modeled to allow for the identification of the phase shifts induced by the variable retarder. As the imposed phase shifts and the measured signals are known, each Eq. (1) features N_c relationships for only three unknowns ($i_{\parallel}^{0}$, $i_{\parallel}^{s}$, $i_{\parallel}^{c}$ for instance). Assuming $N_c > 3$, these two equations systems are thus solved in a least-square sense, to provide the set of unknowns describing the signal measured by each photodiode as a function of the imposed phase shift (Fig.4.2). The calibration quality is then assessed through the least-square residual.

III. 2. *Phase shifts identification*

The calibration procedure yields the parameters necessary to identify the actual phase shifts. The latter is computed by using the measured (normalized) photodiodes signals $\frac{i_{\parallel}}{i_t}$ and $\frac{i_{\perp}}{i_t}$. Eqs (1) now read

$$\begin{aligned}\frac{i_{\parallel}}{i_t} &= i_{\parallel}^{0} + i_{\parallel}^{\star}\cos\left(\gamma_{\parallel} + \delta\right)\\ \frac{i_{\perp}}{i_t} &= i_{\perp}^{0} - i_{\perp}^{\star}\cos\left(\gamma_{\perp} + \delta\right)\end{aligned} \tag{2}$$

$i_{\parallel}^{0}$, $i_{\perp}^{0}$, $i_{\parallel}^{\star}$, $i_{\perp}^{\star}$, $\gamma_{\parallel}$ and $\gamma_{\perp}$ are known from the calibration procedure and δ is the unknown to be determined from the measured normalized photodiodes signals. Denoting $\boldsymbol{i_m}$ the vector defined by $\boldsymbol{i_m}^{t} = \left[\frac{i_{\parallel}}{i_t}, \frac{i_{\perp}}{i_t}\right]$ and

$$\boldsymbol{i_{test}}(\delta) = \begin{bmatrix} i_{\parallel}^{0} + i_{\parallel}^{\star}\cos\left(\gamma_{\parallel} + \delta\right) \\ i_{\perp}^{0} - i_{\perp}^{\star}\cos\left(\gamma_{\perp} + \delta\right) \end{bmatrix} \tag{3}$$

δ is recovered by as the minimizer of

$$\eta(\delta) = 1 - \frac{\boldsymbol{i_m}^{t}\boldsymbol{i_{test}}(\delta)}{\|\,\boldsymbol{i_m}\,\|\,\|\,\boldsymbol{i_{test}}(\delta)\,\|} \tag{4}$$

III. 3. *Δ field computation*

Let us denote I_1, I_2, I_3 and I_4 the images obtained using the four phase shifts δ_1, δ_2, δ_3 and δ_4. The phase shifts are first recovered using the measured photodiode signals and the identification procedure detailed in 2. Assuming the polarizers defects vanish, the local intensities measured at pixel P read

$$I_i(P) = I_0(P) + I_s(P)\sin\,\delta_i + I_c(P)\cos\,\delta_i \text{ for } i \in \{1 \dots 4\} \tag{5}$$

with

$$\begin{aligned} I_0(P) &= A\left(1 + \tan^2\Psi(P)\right) \\ I_s(P) &= -2A\tan\,\Psi(P)\sin\,\Delta(P) \\ I_c(P) &= 2A\tan\,\Psi(P)\cos\,\Delta(P) \end{aligned} \tag{6}$$

For each pixel P, $I_0(P)$, $I_s(P)$ and $I_c(P)$ are first obtained by solving (in a least-square sense) the (over-determined) set of four equations (5). The map for Δ is finally obtained as

$$\Delta(P) = \tan^{-1}\left(\frac{-I_s(P)}{I_c(P)}\right) \tag{7}$$

IV. *Setup performance: thickness and lateral resolutions estimations*

We used this new configuration to characterize ex-situ modified Au surfaces along with the real-time and in-situ monitoring of surface modification by the electrografting of diazonium salts. First, one has to describe the performance of the setup in term of resolutions. As it is an optical microscope, the lateral resolution of the imaging system is estimated. The ellipsometric performances are also attested and the sensitivity and limit of detection of the setup, or resolution in Δ or equivalently in deposited thickness, have been evaluated. As discussed above, we choose to monitor Δ, as the variation of ψ with the thickness of a deposited layer is very small.

Moreover, we were not able, so far, to give an absolute value for the Δ angle, because of an additional phase difference induced by the instrument configuration. In this context, we have monitored quantitatively the variation of Δ.

IV. 1. *Sensitivity and thickness resolution of built setup*

The ellipsometric microscopy will be used to analyze surface sample in air and also in liquid medium. Therefore the sensitivities will be evaluated in both air and liquid.

IV. 1. 1. Theoretical sensitivity estimate

First, it is assumed, as in the previous chapters, that a deposited thin organic film can be optically modeled by a simple layer of an homogeneous and isotropic media of refractive index n_{film}= 1.5, bounded by planar and steep interfaces to a gold reflecting surface, of index n_{Au}, and to an isotropic ambient medium (air or liquid of n_A=1 or 1.33 respectively). The expected variation of Δ with thickness of deposited layer can then be calculated by simulation. The evaluation is based on the estimate of the polarized reflectivities r_p and r_s, in a manner analogous to that described Chapter 2, Section II.2. The reflection coefficients of the p and s components of the electric field amplitude are given respectively by relations similar to (2) from the Chapter 2, Section II.2:

$$\tilde{r}_p = \frac{\tilde{r}_p^{AF} + \tilde{r}_p^{FS} e^{iD}}{1 + \tilde{r}_p^{AF} \tilde{r}_p^{FS} e^{iD}} \qquad (8)$$

$$\tilde{r}_s = \frac{\tilde{r}_s^{AF} + \tilde{r}_s^{FS} e^{iD}}{1 + \tilde{r}_s^{AF} \tilde{r}_s^{FS} e^{iD}} \qquad (9)$$

where $\tilde{r}_p^{AF}, \tilde{r}_s^{AF}$, $\tilde{r}_p^{FS}, \tilde{r}_s^{FS}$ are the complex Fresnel reflection coefficients of ambient/film and film/substrate interfaces for p and s components.

The complex Fresnel reflection coefficients of ambient/ film (similar for film/substrate interface):

$$\tilde{r}_p^{AF} = \frac{\tilde{n}_A/\cos\phi_A - \tilde{n}_F/\cos\phi_F}{\tilde{n}_A/\cos\phi_A + \tilde{n}_F/\cos\phi_F} \qquad (10)$$

$$\tilde{r}_s^{AF} = \frac{\tilde{n}_A\cos\phi_A - \tilde{n}_F\cos\phi_F}{\tilde{n}_A\cos\phi_A + \tilde{n}_A\cos\phi_F} \qquad (11)$$

ϕ_A is the angle of incidence and ϕ_F the angle of refraction in the film.

D is the phase shift due to the travel of light in the film:

$$D = \frac{4\pi}{\lambda} n_F d\cos\phi_F \qquad (12),$$

d is the deposited film thickness.

Let us recall the basic equation of ellipsometry :

$$\rho = \frac{r_p}{r_s} = tan\Psi e^{i\Delta} \qquad (13)$$

where r_p and r_s correspond to complex reflection coefficients of light linearly polarized parallel (p) and perpendicular (s) to the plane of incidence. **Δ** and tan **ψ** are the relative phase and amplitude change respectively, between p and s polarized components due to reflection from the surface.

For reflection from a film-covered surface, the basic equation of ellipsometry (13) becomes:

$$\rho = \frac{(\tilde{r}_p^{AF} + \tilde{r}_p^{FS} e^{iD})}{(\tilde{r}_s^{AF} + \tilde{r}_s^{FS} e^{iD})} \frac{(1 + \tilde{r}_s^{AF}\tilde{r}_s^{FS} e^{iD})}{(1 + \tilde{r}_p^{AF}\tilde{r}_p^{FS} e^{iD})} = \tan\psi e^{i\Delta} \qquad (14)$$

For given values of the optical constants of the three media involved (ambient, film, substrate), the thickness of the film and the angle of incidence, the ellipsometric parameters ψ and Δ can be computed by use of equation (14).

The theoretical variations of Δ with the organic layer thickness, d, deposited on gold surface and in contact with an ambient air or liquid media are presented in Fig. 4.3 and Fig. 4.4 respectively. It can be noticed that the sensitivity in air is higher than in liquid, and similar observations were made in the case of reflectivity variation.

Clearly from the periodic variations in Δ, the sensitivity depends also on the film thickness, however, as we are interested in the early stage of thin film growth, we have estimated the sensitivities for d<30nm. Along Fig 4.2 and 4.3 are presented the calculated sensitivities of Δ obtained as the variation of Δ with film thickness in this range of thin film thickness, d, where Δ decreases linearly with d.

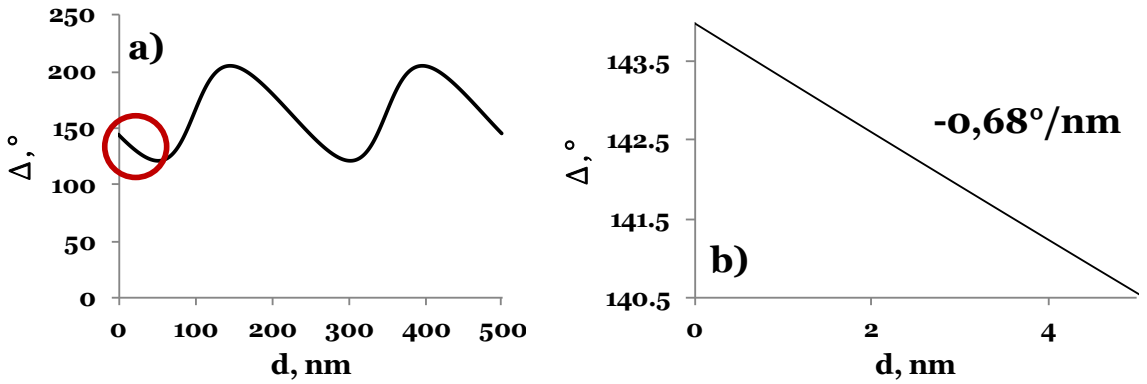

Figure 4.3 Δ in degrees as a function of deposited organic film thickness d on gold in air; a) Δ variation in degree for a deposited film of 500 nm; the black line is calculated from the one layer optical model using the parameters λ=637 nm light, 55° incidence angle, n_{Au}=0.15+3.5i, n_{film}=1.5 b) linear region of Δ periodic variation with *d* (red circle in a).

In a liquid medium the variation of Δ with d is 3.4 times lower than in air predicting a much lower sensitivity of detection in liquid during in-situ measurement.

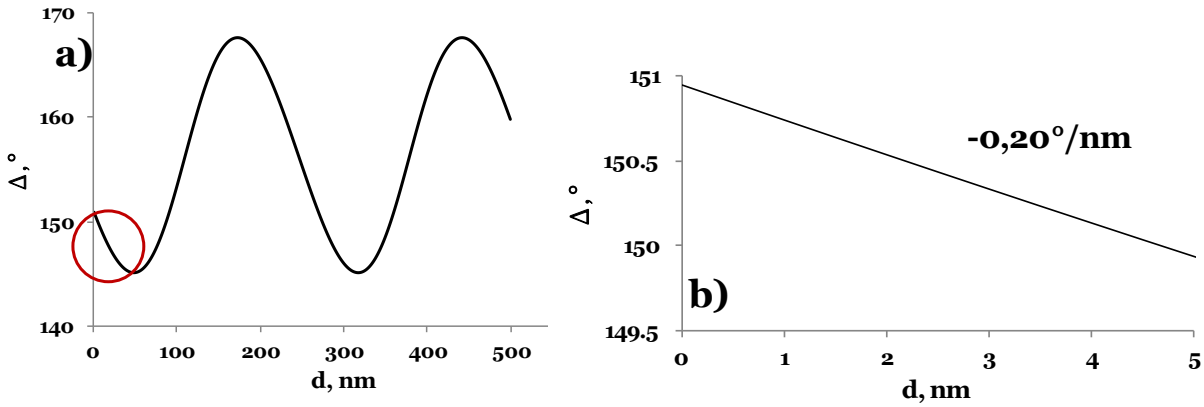

Figure 4.4 Δ in degrees as a function of deposited organic film thickness *d* on gold in liquid medium; a) Δ variation in degrees for a deposited film of 500 nm thickness; the black line is calculated from the one layer optical model using the parameters λ=637 nm light, 45° incidence angle, n_{Au}=0.15+3.5i, n_{liq}=1.33, n_{film}=1.5;b) linear region of Δ periodic variation with d (red circle in a).

IV. 1. 2. Experimental estimate of measurement trueness and limit of detection

These estimates were obtained from measurement either on a clean gold coated silicon wafer or on a gold surface coated with a thin organic layer obtained from the electrografting of a diazonium salt. The trueness of measurement is obtained through comparison of the variation in Δ upon coating of an organic layer whose thickness has been estimated independently with a conventional ellipsometer.

.

A thin layer of 5 nm thickness measured by conventional ellipsometer considering the same optical model as for our setup, induces a variation of 3.2° in Δ measured by our experimental setup in air. If this variation of Δ is converted using evaluated theoretical sensitivity in air of a 0.68°/nm, an estimate thickness of 4.7 nm of the deposited organic layer is founded. As it can be observed, the measured values for the layer thickness are in close agreement, confirming the trueness of measurement of our proposed setup.

As it can be noticed, the sensitivity in air is higher, similar phenomenon founded in the case of reflectivity variation, our experimental setup needs to detect as small variation of Δ as possible. This may be performed by increasing the signal to noise ratio, and is obtained by accumulating a sufficient number of images I_1, I_2, I_3, I_4 to generate a resulting final image in Δ. Fig 4.5 presents the standard deviation in differences of Δ measured on a bare gold surface in air between 2 final images as a function of the number of accumulations. When the number of accumulations is increased, the STD (standard deviation) in each pixel is decreased, while the total time needed for the image acquisition will be considerably increased. We then have chosen the best compromise between optimized acquisition time and STD of the Δ distribution, which is obtained for 16 accumulations. Then, as can be observed from the Fig. 4.4, red circle, the minimal variation of Δ, which can be detected using our setup, is $\delta\Delta$=0.08°. Using the optical model and therefore the predicted sensitivities, it is converted into a minimal deposited layer thickness detection of 0.12 nm in air or 0.39 nm in liquid. These LOD are largely compatible with most of the deposition of organic or bio-organic material on a surface.

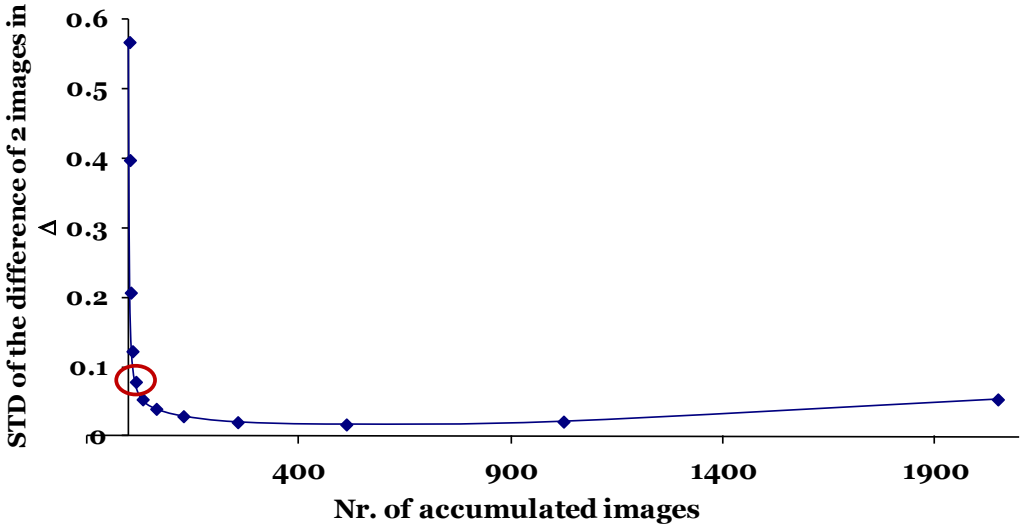

Figure 4.5 Variation of STD of difference between the 2 images in Δ in degrees with the number of accumulated images per acquisition, for an equilibrium time of retarder, T=200ms.

The repeatability of the measurement is then estimated from the calculation of the STD of mean values of a sequence of images in Δ. For a sequence of 6 images (each made from 16 accumulations), we get in liquid meadia as well as in air a STD of 0.04°. As it can be noticed, this value is smaller than that of Δ resolution, which means that, the eventual variations of the recorded signal will not affect our measurements.

IV. 2. *Lateral resolution estimation*

Next we estimate the lateral resolution of our optical microscopic technique. This is obtained through imaging of an ideal punctual object. Ideally, the imaged point is represented by its theoretical Airy diffraction pattern also known as the PSF ("Point Spread Function") [4]. The ideal PSF function for a point centered at x=0 can be expressed as:

$$f_{point}(x) = \frac{\alpha/\pi}{x^2+\alpha^2} \quad (15),$$

where 2α correspond to the lateral resolution of the imaging technique.

Experimentally, it is easier to fabricate and image structures with a knife sharp edge rather than with sharp single points. Such knife edge structures are for example obtained from diffraction gratings with known periodic structure. The theoretical spread function response by an optical microscopic setup of such knife edge is obtained by integration of the PSF (eq.1), and known as the ESF ("Edge SpreadFunction") given by:

$$\boldsymbol{f_{knife-edge}(x) = \frac{1}{\pi}\mathbf{atan}\left(\frac{x}{\alpha}\right) + \frac{1}{2}} \quad (16)$$

The theoretical plot of this function is presented in Fig. 4.5 (b), black line, while that of the point PSF is represented in Fig 4.5(c).

To estimate the lateral resolution of our ellipsometric microscope a diffraction grating defined by Al bands 7 μm large with interband of 3 μm has been imaged (Fig. 4.6, red rectangle). The entire imaged zone with the given magnification objective is 90 x 90 μm (corresponding to 256 x 256 pixel). The knife edge plot is extracted from this image by pixel by pixel decomposition of the normalized light intensity along the axis normal to the edge structure as presented in Fig 4.6 b) (experimental dots and dashed line). By fitting the edge knife plot with the ESF function (Cauchy fit), we find α=1.62 which gives a resolution of 2α=3.25 pixels. It corresponds with the known magnification to a resolution of 1.16 μm in air. Fig.4.6 c) illustrates the theoretical PSF expected for the detection of 2 points with the estimated resolution of our setup. A similar measurement was achieved in a liquid medium, a resolution of about 1 μm was also obtained.

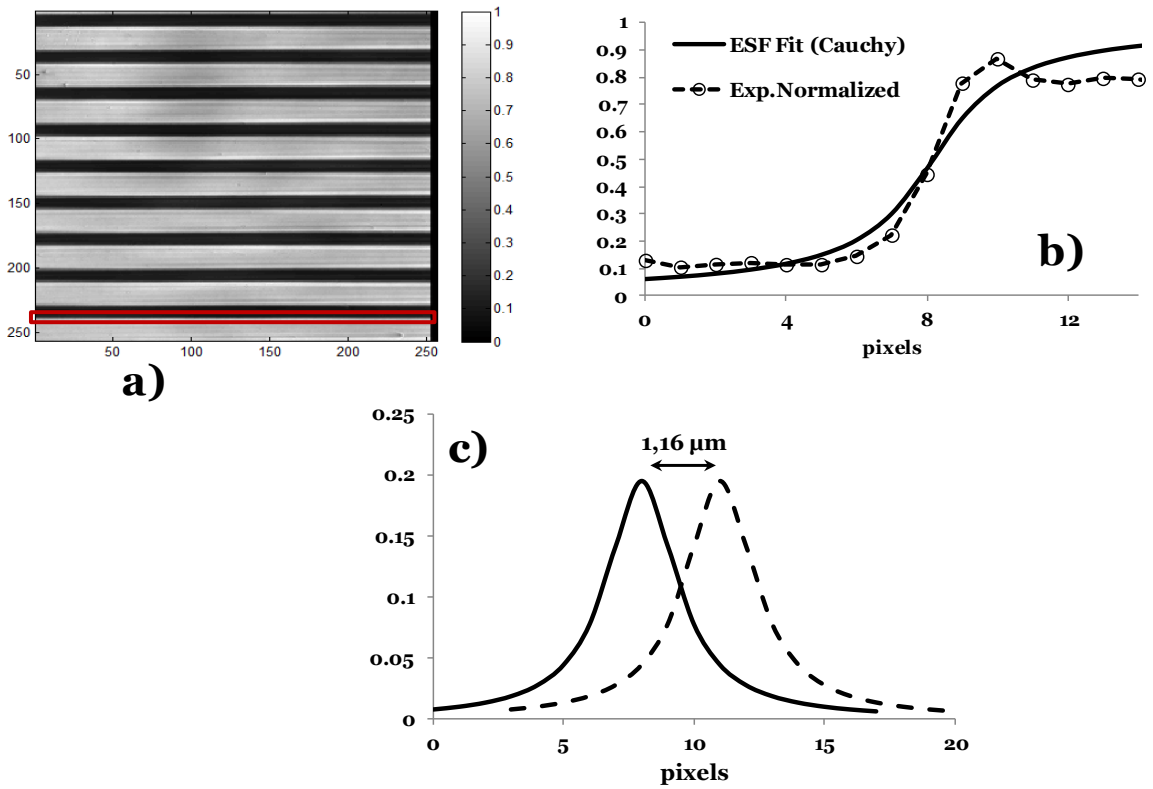

Figure 4.6 a) Image of a diffraction grating structure; b) ESF function of a knife edge , from diffraction grating (dashed line with open circles), Cauchy fitted (black line); c) PSF plot of 2 nearest resolved points.

V. *Illustration of ellipsometric imagery of ex-situ modified surfaces*

Once the performances of our ellipsometric microscope have been estimated, we propose to test its capacities to image and quantify chemical transformation of surfaces. We follow the strategy developed in the case of light reflectivity and illustrated in the case of the electrografting of diazonium salts. In this section the microscope is used to image and characterize gold electrode surfaces grafted ex-situ by the NP as described in Chapter 2, Sect. I.1.

We take benefit of the imaging capability by resolving local micrometric domains of nanometer thick organic layers within the electrodes. Ellipsometric images 70 µm x 70 µm of a large (2cm x 0.5cm) gold surface electrografted ex-situ with a thin NP film, allows reading the homogeneity of the coated layer with micrometric lateral resolution.

The layer actually presents defects in the micrometer range (see the 2-5 µm diameter disks in Fig 4.7 a) most likely reproducing defects from the gold sub-surface. The ellipsometric microscope is particularly adapted to image interfacial regions as that presented in Fig. 4.7 a) for the border between an electrografted domain (region III) and bare ungrafted gold surface (region I). The image a) has been taken in air and is typically obtained as the δΔ distribution over the surface. As the border between domains is barely distinguished, four sequential intensity images are taken in the area of the border, with a following image processing which consider also the difference with Δ distribution of a bare Au region, prior to obtain the δΔ distribution in each pixel. The duration of an image acquisition is about 2.6 s.

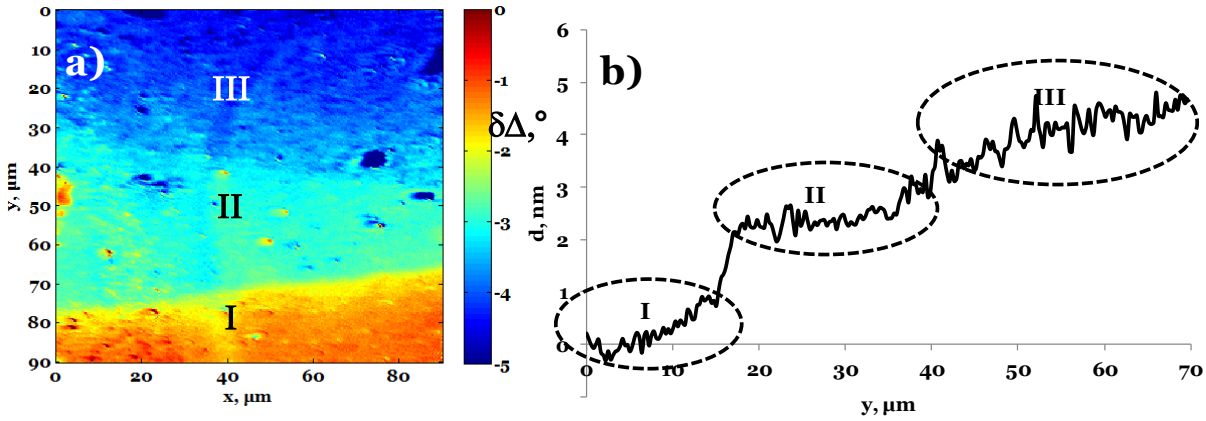

Figure 4.7 a) Image border of an ex-situ grafted nitrophenyl film on a gold substrate with a thickness of about 5 nm in air; b) The structure of film border (profile on 'y' direction).

The deposited film thickness was of ~5 nm as measured by conventional ellipsometer. This thickness was confirmed by our setup measures, as δΔ between bare gold (bottom red region, I) and grafted region (top dark blue region, III) is of about 3.2°. Converting δΔ variation in film thickness with the theoretically estimated sensitivity allowed transforming the δΔ distribution image into thickness distribution image, or similarly as plotted in Fig 4.7 b) as a profile of the thickness variation along a line in the y-axis direction. The advantage of the imaging capability of our setup can be revealed in this case, by obtaining the structure of an eletrografted film border.

The image clearly presents 3 regions: the bottom, I, red – corresponding to the bare gold; the top, III, dark blue – corresponding to the region grafted with the organic layer; and a middle region, II, light blue – corresponding to a 20 to 40 µm wide region grafted with a thinner layer. This intermediate region corresponds to the grafting which occurred at the solution meniscus, formed by capillarity, during the vertical holding of the fold electrode surface in the electrografting solution.

The frontiers between the different regions are sharp, they are of about 2 µm large for the frontier between regions I and II and of about 26 µm for the frontier between regions II and III in the air. The large border of the latter can be explained by the evaporation of the solution during the grafting. Within a phenomenological approach, they could be fitted by ESF functions with apparent α values of 3.05 and 36.9 corresponding to 2.1 and 26 µm respectively for the frontier from I to II and II to III regions.

These values higher than the setup lateral resolution indicate that the extension of the grafted border is wider than the resolution of the optical device. It means that electrografting processes provides diffuse-edge rather than knife-edge as can be obtained by standard lithographic techniques

Similar observations were made for a 4 nm grafted nitrophenyl film observed in a liquid medium (Fig 4.8). Again, the limit between grafted and bare gold (I, red-yellow – bare Au; II, blue – grafted region), can be easily distinguished in the image a) or on the profile b) of the deposited film thickness along the 'y' direction.

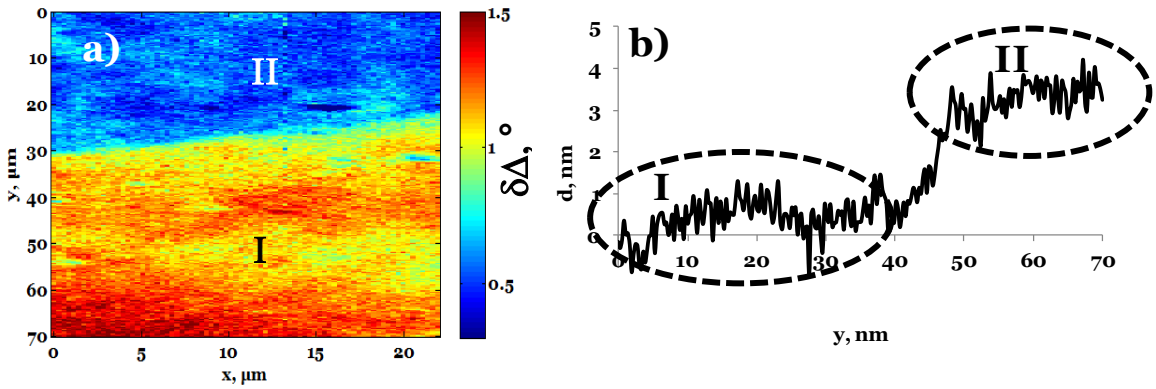

Figure 4.8 a) Image border of an ex-situ grafted nitrophenyl film on gold with a thickness of about 4 nm in liquid; b) The structure of film border (profile on 'y' direction).

The conversion of the δΔ variations into layer thickness with the estimated sensitivity in liquid (-0.2° /nm of deposited organic layer, n=1.5) is also consistent with a 4 nm thick layer obtained with a conventional ellipsometer, proving the trueness of the measurement provided by our instrument in liquid meadia. The border between the two regions was again analyzed and fitted to ESF function. The ~2µm value obtained, larger than the 1µm setup resolution in liquid, confirms the diffuse-edge of the border.

The imagery mode is particularly interesting for imaging microstructures. It is used to analyze Δ variation induced by the electrografting of gold microelectrodes arrays. This is illustrated in Fig. 4.9 for an array of Au band microelectrodes (7µm large, interband 3µm) where three microbands of the array (in blue) were electrically connected and electrografted ex-situ under high reductive potential, to enforce the deposition of a thick layer.

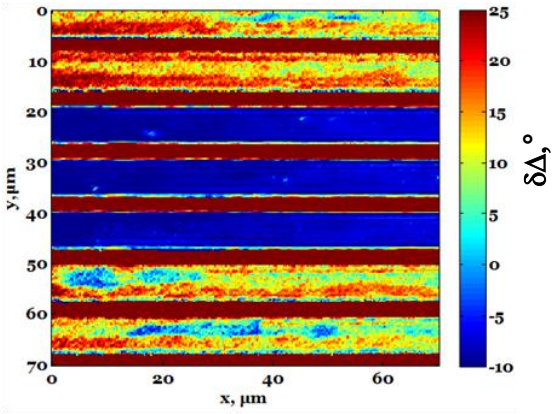

Figure 4.9 Au micro-electrode array ex-situ electrografted with NBD

The grafted bands are blue in the Fig. 4.9. As the difference for δΔ between grafted and non-grafted bands is about 25°, this large value exceeds the highest theoretical δΔ in the case of a modeled transparent organic layer. A similar conclusion was drawn during the fast grafting of thick layers under highly negative potential followed by light reflectivity (Chapter 2) and was attributed to absorbing or diffusing properties of the grown layer. All this examples illustrate the possibility to characterize in depth the structure of deposited film, or the homogeneity of grafting for a local film deposition.

VI. *In-situ and real-time surface modification monitoring using ellispometric imagery*

VI. 1. *Real-time surface modification monitoring of large surfaces*

The innovative application of our setup is related to the relative fast (<2.6s) image acquisition which should allow to follow in-situ and in real-time the process of film deposition by monitoring the variation of Δ. The film deposition is accomplished using already described simple reaction of surfaces electro-grafting by reduction of diazonium salts [5, 6]. The first example of this kind of application relates to the electrografting of diazonium salt of a bare gold covered Si-wafer surface with an area of about 2 cm^2. The electro-grafting film deposition was done in a 5 x 10^{-3} mol L^{-1} of NBD and 1 x 10 mol L^{-1} of NBu_4BF_4 in acetonitrile.

The variation of Δ averaged on a 10μm x 10μm region obtained from the continuously recorded images was correlated to the total charge during the electrografting process, as in Fig. 4.10, a). By detailed image treatment, it can be plotted for example, – the **z** number of transferred electrons during grafting in each pixel. Thereby the local efficiency of reaction can be apprehended (Fig. 4.10, b). In this image we correlate a local surface information (the deposited thickness) to a global variable (the charge passed over the whole electrode). It is interesting noting that both variables fit nicely, at least up to 225 s, which indicates that at a local micrometric scale, the process is governed by an electrochemical or charge transfer process. At longer times, the deviation indicates the decrease of the grafting efficiency as the layer thickness is likely too thick to ensure sufficient trapping of radical species by the film.

The efficiency of radical grafting can be characterized by '**z**' – the number of transferred electrons per diazonium molecule during the grafting of the radical moieties. The δΔ distribution along the observed surface can then be converted into a thickness distribution and then into a distribution image of '**z**' as presented in Fig 4.10 b). This figure shows a detailed image in which the local efficiency of the grafting reaction can be apprehended at the level of individual 3 pixels (the setup resolution). One can then distinguish local phenomena on regions of about 1x1 $μm^2$. Movies can also be obtained showing the local and global evolution of the grafting process.

On the individual image obtained at the end of the grafting presented in Fig 4.10 b) – '**z**' varies between 4.2 and 4.4 transferred electrons indicating that the grafting is mostly homogenous. Systematic higher '**z**' values are observed on the right part of the image, darker regions (dark blue), which actually correspond to uncorrected lower δΔ variation. A small tilt in δΔ is observed on all images performed in liquid media and is actually due residual aberrations of the imaging configuration.

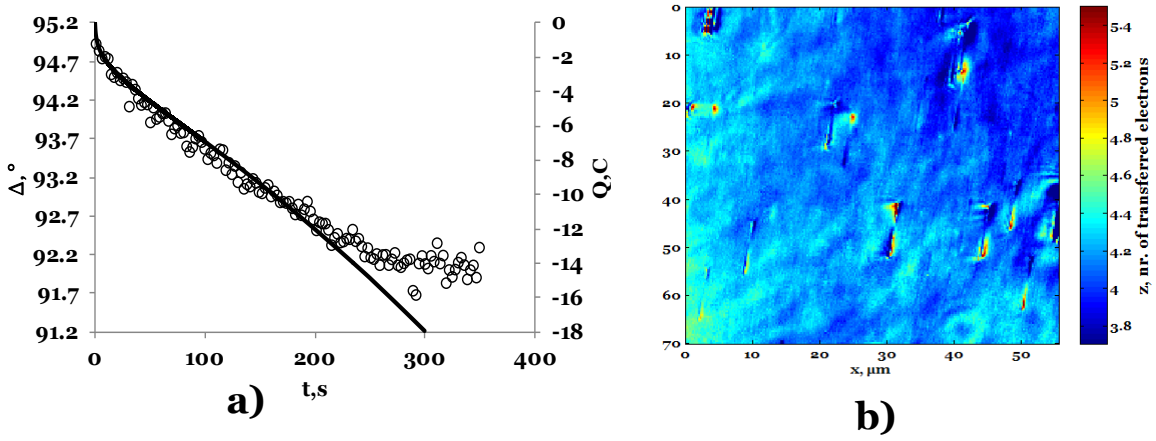

Figure 4.10 a) Variation of Δ in degrees, averaged on a 10µm x 10µm during NBD electrograting (black open circles) correlated with consumed charge (black dashed line), for a chronoamperometric potential step between 0.2 and -0.6 V vs Ag/ AgCl for 300 s; b) the distribution of **z**, number of transferred electrons during electrografting of diazonium salt in each pixel.

VI. 1. 1. Validation of deposited organic layer using FT-IRRAS on large surfaces

The second evidence for diazonium deposited film was obtained by FT-IRRAS spectra of the grafted sample. Through this approach we took advantage of using large substrate to validate the proposed concept for the in-situ and real-time follow-up of surface modifications. The FT-IRRAS measurements allowed to verify again the trueness of the technique in liquid media.

The presence of nitrophenyl group is easily confirmed trough the observed two strong bands corresponding to the nitro groups at about 1350 and 1530 cm^{-1} (symmetric and

asymmetric stretching), and by ring stretching C-C vibrations band at 1600 cm^{-1}.(Fig. 4.11)

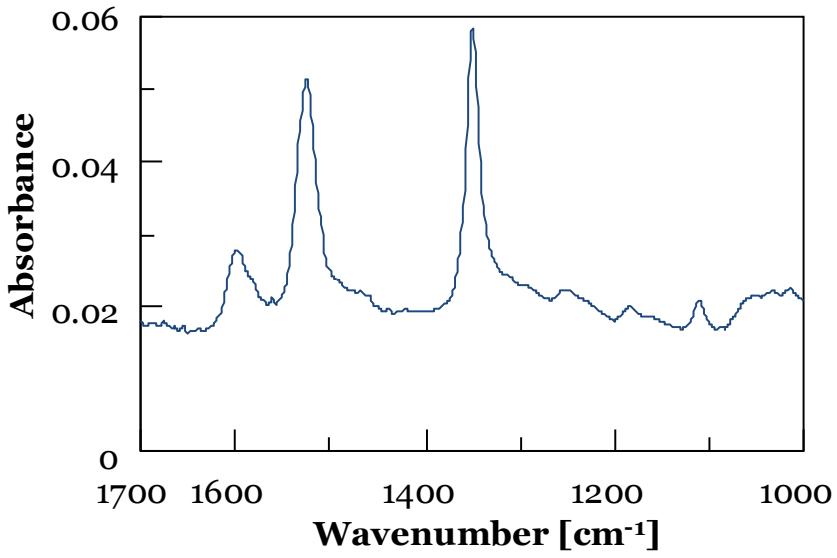

Figure 4.11 FT-IRRAS spectra of Au electrode modified by electroreduction of NBD salt

As Δ varies with about 3 degrees at the end of electrografting process, the thickness of the deposited film was evaluated at about 15 nm, knowing the theoretical sensitivity for Δ variation of 0.2°/ nm of deposited organic film in liquid media.

By analyzing peak heights corresponding for IRRAS nitro groups bands at 1351 and 1526 cm^{-1}, in our case having the intensities of 0.033 and 0.029 respectively, and using the correlation between the deposited film thickness and the absorbance presented in [7], the thickness of about 15 nm founded by imaging ellipsometry is confirmed.

Thus, on a large surface, (i) the good correlation between local ellipsometric indication and global charge transfer and (ii) the homogeneous local thickness distribution, suggest that the electrografting process is homogeneous and proceed at the same rate on the whole sample surface, at least at the micrometer scale.

VI. 2. *Surface modification monitoring of micropatterned surfaces – study of local reactivity*

As a further advantage of the imaging ellipsometric microscope, we could monitor the same type of surface modification, on micropatterned electrode surface. We have presented earlier the grafting of microelectrode arrays. Here we examine the grafting on gold surface patterned with a self-assembled monolayer of thiol. The surface patterning was obtained through standard UV-VIS photolithographic techniques, the process depicted already in Chapter 3, Fig. 3.2. It should be mentioned that in this case the pattern of the used mask consisted of open orifices of 6μm in diameter spaced by 15 μm.

The final patterned thiolated Au surface have been imaged by the ellipsometric microscope. Figure 4.12 presents the image in liquid media (ACN) of δΔ distribution of the patterned surface before diazonium electrografting. Clearly the setup allows detecting the patterns formed on the Au surface during the photolithographic procedure. The patterns are characterized as holes, of negative δΔ values (Figure 4.12,**a)**. The shape of the holes is not perfectly circular resulting likely from either some heterogeneous resin transformation during the UV irradiation or heterogeneous RIE etching. Moreover, the δΔ difference between the regions inside the holes and outside the holes is as high as ~2° corresponding to an apparent higher thickness of 10nm, in terms of organic layer thickness, inside the patterns, phenomena better observed in (Fig.4.12, **b**).

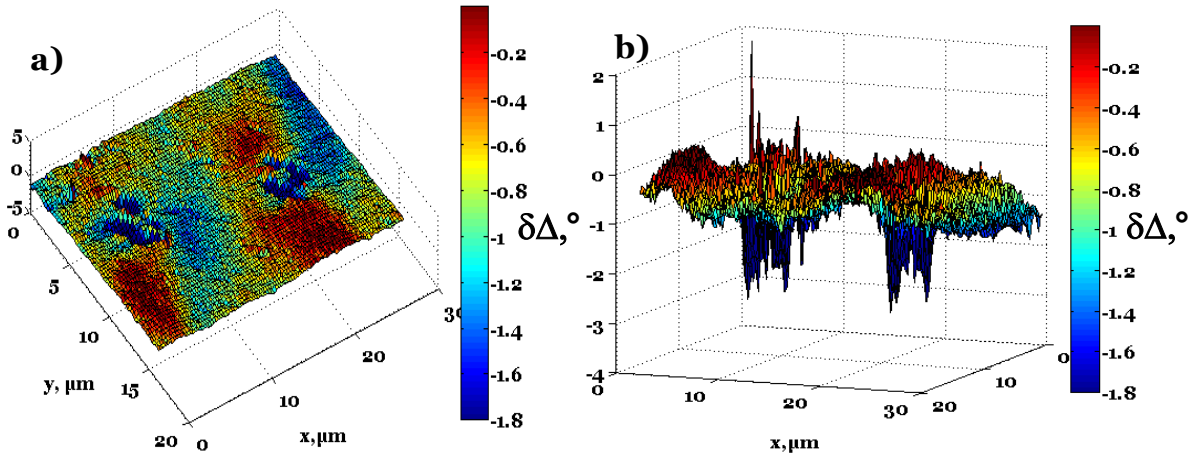

Figure 4.12 δΔ in degrees distribution of the modified sample before diazonium electrografting: a) and b) show different views of the modified surface before the grafting.

This may seem strange if one consider that the photolithographic procedure was expected to desorb locally the thiol within the patterns and one would have expected a decrease of thickness of approx 1 nm (an increase of δΔ of about 0.2°) within the patterns. The opposite and higher than expected difference in δΔ can be explained by the modification of Au surface structure during the RIE process. The chemical structure introduced modification of a surface layer of the gold film introduced during this vigorous etching process produces an altered optical response compared to Au. If one consider that RIE is performed in the presence of oxygen and highly reactive gaseous species, it is likely that gold oxides are formed during the RIE process. It is also shown in Fig 4.12 that if the ellipsometric difference detected within the pattern is due to gold oxide formation, the layer of this oxide is not homogeneous. It is then anticipated that the patterned surface could present different reactivity towards the process of diazonium electrografting within the pattern. The ellipsometric microscope is then a dedicated tool to inspect this local surface reactivity.

We next evaluate and follow *in situ* and real time the electrografting of the patterned surface by a NBD. Figure 4.13 presents the variation in δΔ distribution measured between the images recorded at the end and before the diazonium electrografting process. This way of data analysis actually allows 'erasing' the heterogeneity of the initial optical response detected within the patterned surface (as those observed in Figure 4.12). In this way, the modifications appearing on the substrate reveals the heterogeneity in electrografting reactivity of the surface. The first striking point which can be denoted is the heterogeneous nature of the electrografting of diazonium.

From this image, it can be easily noticed, that the regions where a thicker layer was deposited (more negative δΔ values), correspond to the patterned thiol structures (holes), where the gold was supposed to be recovered and the surface is likely more reactive. The transformation of the δΔ image into distribution of thickness of the deposited layer on the substrate (Fig. 4.14), indicates that almost 6nm of a nitrophenyl layer has been grafted within the holes, the regions within black circles.

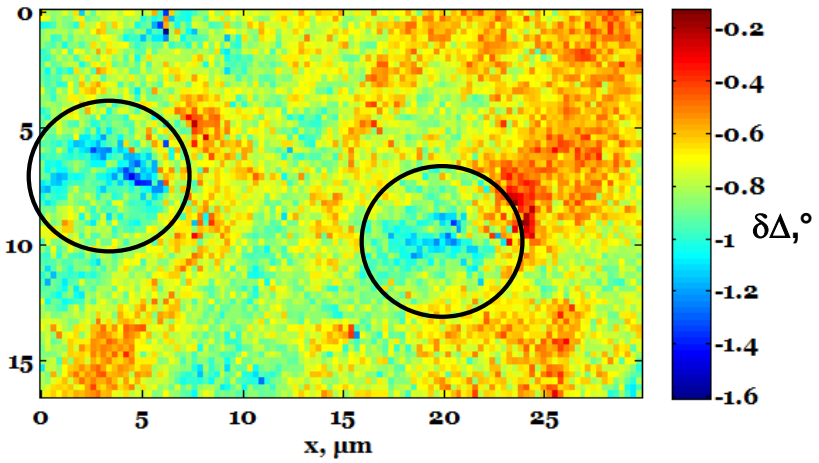

Figure 4.13 δΔ variation in degrees after the diazonium electrografting, difference between last and first image

Moreover, outside these holes where the thiol has been removed, a lower deposition of the organic nitrophenyl layer is observed. This can be explained either by attachment of the diazonium layer directly to the adsorbed thiols, or by (partial) desorption of the thiol layer with simultaneous grafting of the diazonium salt. The desorption step could explain the lower apparent efficiency of the grafting suggested by the lower thickness deposited in this region compared to what was observed on the patterns corresponding to the areas of totally desorbed thiols.

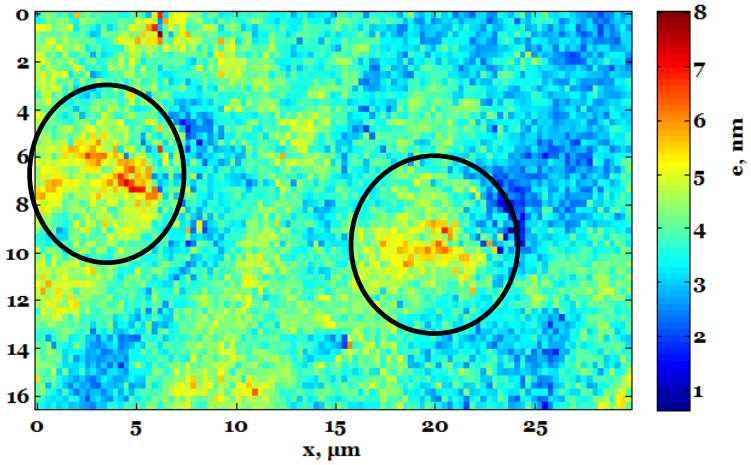

Figure 4.14 The thickness in nm of the deposited organic layer at the end of diazonium electro-grafting (difference between last and first image)

Conclusions

A new configuration of ellispometry imagery microscope was presented. The imaging performances of the setup have been determined and validated for the ex-situ characterization in air of the local heterogeneity developed during the deposition of organic films on gold surfaces. The presented setup showed about 1 μm in lateral resolution, along with a thickness resolution of about 0.1 nm. The originality of the proposed setup was illustrated through the real time and in-situ quantitative monitoring of the local modification of a Au substrate during its coating with a thin organic layer. The coating was obtained through the electrografting of the electrode surface by a diazonium salt. It allows us to evidence the heterogeneity of the electrografting process on patterned surfaces revealing the local chemical and electrochemical reactivity of surfaces.

References

1. Beaglehole, D., *PERFORMANCE OF A MICROSCOPIC IMAGING ELLIPSOMETER*. Review of Scientific Instruments, 1988. **59**(12): p. 2557-2559.
2. S. Hénon, J.M., *Microscope at the Brewster angle: Direct observation of first-order phase transitions in monolayers*. Review of Scientific Instruments, 1990. **62**(4): p. 936.
3. K. R. Neumaier, G.E., E. Sackmann, R. Merkel *Ellipsometric microscopy*. Europhysics Letters, 2000. **49**(1): p. 14.
4. Smith, E.H.B., *PSF estimation by gradient descent fit to the ESF - art. no. 60590E*, in *Image Quality and System Performance III*, L.C. Cui and Y. Miyake, Editors. 2006, Spie-Int Soc Optical Engineering: Bellingham. p. E590-E590.
5. Pinson, J. and F. Podvorica, *Attachment of organic layers to conductive or semiconductive surfaces by reduction of diazonium salts*. Chemical Society Reviews, 2005. **34**(5): p. 429-439.
6. Belanger, D. and J. Pinson, *Electrografting: a powerful method for surface modification*. Chemical Society Reviews, 2011. **40**(7): p. 3995-4048.
7. Busson, M., et al., *Photochemical grafting of diazonium salts on metals*. Chemical Communications, 2011. **47**(47): p. 12631-12633.

Chapter 5 : Electrochemical characterization of mechanical processes at microcantilevers

I. *Introduction:*

The context of this part of research is not related directly to the main topic of the thesis, which considers the coupling of electrochemical techniques to optical imagery in order to study in situ and real time the surface transformation at the micrometer scale. Nevertheless some related aspects can be still found. First Au microcantilever platforms were among the electrode studied by opto-electrochemical microscopy and the long-term objective of this project is to apply such microscopy to such analytical platforms. Second, investigating by SECM microcantilevers also provide an approach that combined electrochemical and mechanical characterization.

The electrogafting of NBD at Au microcantilevers was inspected by light reflectivity imaging. As the cantilevers are known for their special mechanical properties, we were interested in the characterization of the mechanical phenomenon associated with the deposition of organic material at these structures under electrochemical activation. The cantilever deflections due to surface stress changes are mainly revealed optically, by focusing a laser beam at the cantilever end, measuring the displacement of the reflected spot with a PSD (position sensitive detector). For light reflectivity microscopy inspection we proposed to detect cantilever movements associated to electrochemical activation using a surface lighting by 2 wavelengths (using LEDs). This should allow decoupling the optical contributions related to the deformation of the cantilever and to the electrochemical reaction on the platform surface, by identifying the dependent and independent contributions of the wavelength. As the developed optical method to detect cantilever mechanical movements is still laborious, due to heavy initial calibration steps, I have decided not to present these preliminary results. Instead, I present in this chapter an alternative method of movement detection based on the electrochemical detection of cantilever deflection using scanning electrochemical microscopy (SECM). The following results of this work are presented through an article recently published in Analytical Chemistry.

Article

Scanning Electrochemical Microscopy Monitoring in Microcantilever Platforms.

Sorin Munteanu,[a] Sarra Gam-Derouich,[a] Cécile Flammier,[b] Yasmina Fedala,[a] Catherine Combellas,[a] Fabien Amiot,[b] Frédéric Kanoufi[a,]*

[a] PECSA UMR 7195, ESPCI ParisTech, 10 rue Vauquelin, 75231 Paris cedex 05, France.

[b] FEMTO-ST Institute, CNRS-UMR 6174/UFC/ENSMM/UTBM, 24 chemin de l'Épitaphe, 25030 Besançon, France.

*Correspondance to: Frederic Kanoufi – Email: frederic.kanoufi@espci.fr

ABSTRACT : The deflection of cantilever systems may be performed by an indirect electrochemical method that consists of measuring the local cantilever activity and deflection in a feedback generation-collection configuration of the SECM. This is illustrated during the electrochemically-assisted adsorption of Br onto a gold coated cantilever, either in its pristine state or previously coated with a thin organic barrier. It is further extended to the adsorption of an antibody in a heterogeneous immunoassay at an allergen-coated microcantilever platform. In both reactions, the

cantilever deflection is qualitatively detected from the SECM tip current measurement and a quantitative estimate is obtained through modeling.

This electroanalytical strategy provides an alternative approach to standard optical detection. It can overcome some limitations of the optical method by allowing electrochemical characterization of non-conductive cantilevers and appropriate use for closed systems.

1. INTRODUCTION

The objective is to detect in-situ mechanical displacements of various platforms such as arrays of gold coated (Au) microcantilevers. The latter are promising mechanical objects, that were classically developed for the AFM and used as point-end tips to measure ultrasmall forces on particles with size of one atom[1]. Considering their specific mechanical properties characterized by their horizontal deflection or shift in resonance frequency as a result of different local changes in mass, temperature, charge or intermolecular interactions, their largest application is accepted as sensing micro-devices. Their ability to be used as physical, chemical and biological sensors is described in several review articles [2-4]. When operated in a quasi-static mode, microcantilever platforms are used for antibody-antigen assays [5, 6], DNA hybridization [7, 8], detection of toxic heavy metal ions [9, 10] or of any electrochemically-induced surface charge accumulation [11, 12]. Then, the cantilever deflection is measured as the result of the interaction of an analyte with the sensing coating deposited onto one of the cantilever faces. The cantilever mechanical deformations are revealed optically by focusing a laser beam at the cantilever end, and measuring the displacement of a reflected spot thanks to a position sensitive detector.

This type of detection is well adapted for cantilever arrays, as it allows detecting specifically target species in a mixture [13]. The cantilever bending measured in this way can reach a sub-nm resolution.

When microcantilever platforms are coated with a conductive gold layer, as presented in Figure 5.1 a, the optical detection can be combined with the electrochemical actuation and/or detection. On one hand, an electrochemical detection allows an increased robustness of the sensing platform and submonolayer redox state changes can be addressed [14]. On the other hand, an electrochemical actuation may be used to enforce a mechanical deflection of the cantilever driven by its charge [15-17] or by the molecular reorganization of the moieties assembled on its surface [14, 18]. This strategy is particularly appealing to decipher heterogeneous surface effects[15], especially when combined with full-field optical detection, to get insight into the mechanical behavior of microcantilevers [15, 17].

Actually, special care must be taken when optical detection is performed in the course of the electrochemical solicitation of the cantilever. Indeed, ions concentration gradients in the double layer induced by the electrochemical actuation may affect the optical response, for example by mirage effects through the local change in refractive index [19, 20]. The objective of this contribution is to propose an alternative detection mode of cantilever deflection based on deported electrochemical measurements. It consists of replacing the local optical probe of the cantilever movement by a local electrochemical probe. Different strategies may be proposed based on dual-electrode systems working in the generation/collection (GC) mode. Such configuration based on redox cycling between a generator and a collector is a widely used electroanalytical technique [21]. It is the basic principle of the scanning electrochemical microscope (SECM),[22, 23] which allows handling microelectrodes

within micro- or sub-micrometer separation distances [24, 25]. This principle has also been more recently miniaturized in microfluidic systems as electrochemical detection tools [26] or in electrochemical nanogaps to produce powerful mechanistic [27] and biosensing [28] platforms with single molecule detection capabilities. The transposition of the feedback GC mode with microcantilever platforms can be achieved by holding a small electrochemical probe (Generator) in the vicinity of a cantilever electrode (Collector). This is easily achieved in the SECM configuration (Fig. 5.1 c). To our knowledge, the combination of microcantilevers and SECM has only been described when microcantilevers are used as SECM tips for simultaneous topographical and electrochemical imaging of a sample surface with enhanced spatial resolution [29-31]. Here, we propose to use a standard microelectrode (a tip) to interrogate the microcantilever electrochemical and mechanical activity. The SECM is used to image and quantify the electrochemical reactivity of gold coated micro-cantilever platforms. Such micromechanical cantilevers have been used as chemo-sensors or electrochemo-sensors once an appropriate sensing target has been anchored on their surfaces[3]. Usually, the coating of an organic layer on an electrode alters the electron transfer properties and results in the lowering of the Au electrochemical properties. Here, two types of cantilever platforms are considered: i) a pristine Au-coated cantilever, $CANT_{cond}$, which will mimic an electrochemical actuating platform (Fig. 5.1 a) and, ii) an Au-cantilever coated with a thin organic layer which will mimic a sensing layer coated cantilever (Fig. 5.1 b).

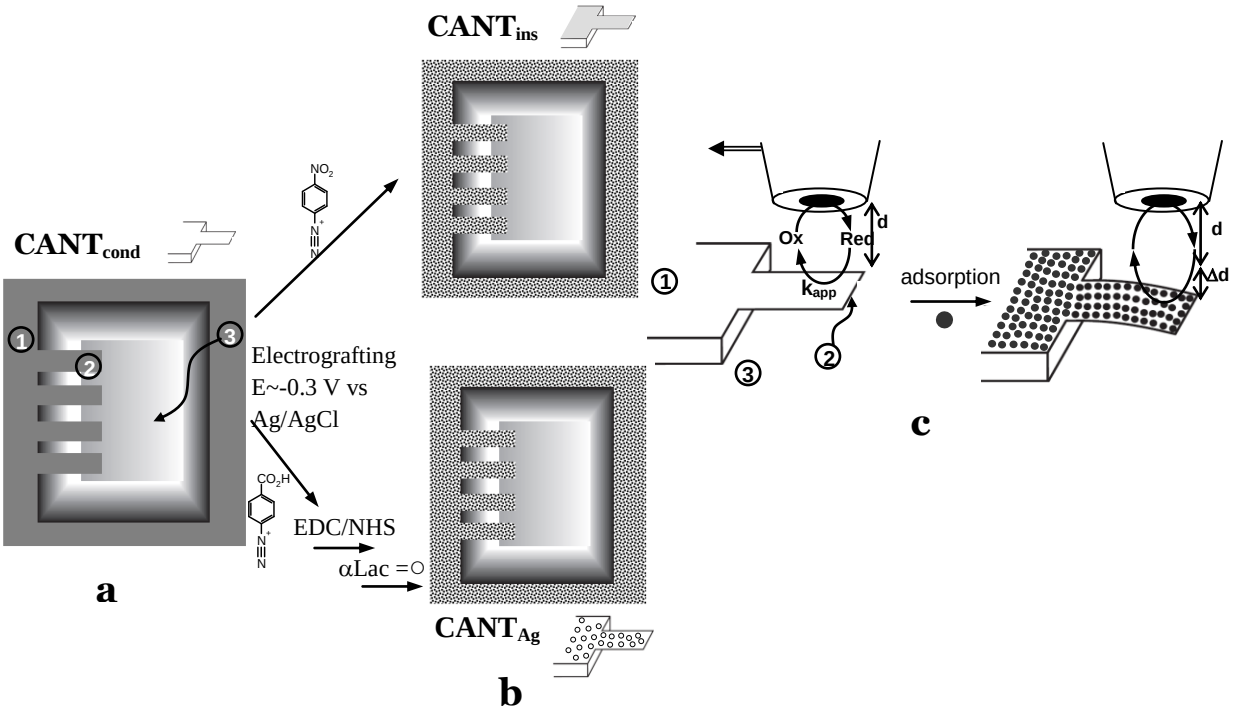

Figure 5.1 Schematic representation of the platform : a) bare Au cantilever array, CANTcond; b) cantilever array grafted with: a thin organic film, CANTins, or a biochemical layer of an antigen (Ag: α-lactalbumin: α-Lac), CANTAg; c) SECM inspection of a species (● = Br^- or anti-αLac) adsorption on the cantilever platform based on electrochemical measurement in the feedback mode. 1) plain substrate, 2) cantilever free end, and 3) carved pool (90 μm deep).

An example of the latter platform is illustrated by the case of a thin nanometer film obtained through the electrografting of a diazonium salt ($CANT_{ins}$, upper part of Fig. 5.1 b); this is a promising, fast and efficient strategy for the coating of conducting surfaces with functional organic layers [32]. Indeed, a -COOH terminated thin film obtained via diazonium chemistry can be used to covalently bind a biochemical entity, an α-lactalbumin antigen (lower part of Fig. 5.1 b). This sensing platform, $CANT_{Ag}$, is capable of sensing in a heterogeneous immunoassay the corresponding antibody present in solution via a receptor-ligand interaction.

2. EXPERIMENTAL SECTION

2.1. Materials. The microcantilever platforms were fabricated by LAAS (Toulouse, France). They were obtained by i) etching the thermally grown oxide layer on top of a silicon (100) wafer to define arrays of 8 microcantilevers (70 μm long, 20 μm wide, 770 nm thick), ii) release by etching the exposed silicon with KOH and iii) coating the whole wafer forming the cantilever platform with a 50 nm Au layer on top of a 20 nm Ti adhesion layer. Chemicals: $Ru(NH_3)_6Cl_3$, $K_4Fe(CN)_6$, 4-nitrobenzenediazonium, 4-carboxybenzenediazonium, KCl, pH 7.5 phosphate buffer saline (PBS) made from (137mM NaCl, 8mM (KH_2PO_4 + Na_2HPO_4)), 1-ethyl-3-[3-dimethylaminopropyl]carbodiimide hydrochloride (EDC), ester of N-hydroxysuccinimide NHS, α-lactalbumin, glycine, were used as received from Aldrich, anti-α-lactalbumine was used as received from Genetex.

2.2. Cantilever platform surface derivatizations. The coating of the microcantilever platform with an organic layer was achieved by the reduction at an Au-coated microcantilever platform, $CANT_{cond}$, of a 0.1 M NBu_4BF_4 acetonitrile solution containing 5 mM of either 4-nitrobenzenediazonium ($CANT_{ins}$) or 4-carboxybenzenediazonium ($CANT_{Ag}$). The reduction was achieved under potentiostatic conditions by applying a potential 0.3 V more negative than the diazonium reduction potential for 300 s. This procedures leads to the immobilization of a 8 nm thick nitrophenyl multilayer on Au, $CANT_{ins}$. The sensing layer in $CANT_{Ag}$ was obtained by electrografting $CANT_{cond}$ in a 5 mM 4-carboxybenzenediazonium + 0.1 M NBu_4BF_4 acetonitrile solution. The –COOH terminated functionalities were then coupled to α-lactalbumin antigen (Ag, 20 μM in PBS) through peptidic coupling via EDC/NHS: the substrates were treated with a solution of NHS (60 mM) and EDC (30 mM) in ultrapure water for 90 min, then rinsed in Milli-Q water and dried under

a flow of dry nitrogen. The Ag was then immobilized by reacting the substrates with an Ag solution (20 µM in PBS) for 2 h. After this step, the excess of non immobilized Ag was removed by three repeated washings with PBS. In order to block binding sites not occupied by bioactive species, the Ag derivatized substrates were then immersed for 15 min in a 1-aminoethanol solution (1 M), then washed with PBS and Milli-Q water. To prevent non-specific interaction, the substrates were further immersed for 15 min in 2 % polyvinyl-pyrrolidone solutions, and then vigorously rinsed three times with PBS and Milli-Q water. The bioactive surfaces prepared were abbreviated as $CANT_{Ag}$.

2.3. SECM procedures. The SECM experiments were performed with either a homemade or a CH910B SECM (CH Instruments, Austin, Tx, USA) station equipped with video observation (Navitar long range lenses). Images and approach curves were obtained after tilt adjustment of the Au plain platform versus the SECM probe displacement. The positioning of the tip above the plain substrate or the free end of a microcantilever was assigned from the SECM image, the tip was positioned respectively 100 µm away from the plain substrate/pool border or 5-10 µm from the cantilever end. For both the plain substrate and the cantilever free end, distances from the tip, d, are measured above the plain substrate, this means that if the cantilever is tilted, the true distance between the tip and the cantilever free end is either larger (downward deflection) or smaller (upward deflection) than d. Linescans are drawn at tip scan rate of 5µm/s to minimize convection influence on the tip current. Images are made as 10µm/s linescans every 2µm.

The SECM experiments were conducted in a 20 µL droplet of electrolytic solution covering the whole 6x6 mm^2 substrate area. The tip was made from a 25 µm diameter Pt wire embedded into a glass insulating sheath of radius 7 times larger than the tip

radius (RG=7). A 250 µm diameter Pt wire was used as the auxiliary and a 250 µm diameter Ag/AgCl wire was used as a pseudo-reference electrode. The tip positioning, imaging and substrate characterization was obtained in an electrolytic solution containing a redox probe ($Ru(NH_3)_6Cl_3$ for $CANT_{cond}$ and $CANT_{ins}$; $K_4Fe(CN)_6$ for $CANT_{Ag}$). The tip was biased at a potential where the redox probe is transformed under mass transfer control: E_{tip} = - 0.3 V vs Ag/AgCl for $Ru(NH_3)_6^{3+}$ reduction or E_{tip} = 0.4 V vs Ag/AgCl for $Fe(CN)_6^{4-}$ oxidation.

2.4. **Immunoassays**. The immunoassay experiments in the SECM configuration were performed in solutions containing the same 2 mM concentration of $Fe(CN)_6^{4-}$ redox probe in order to avoid the redox probe dilution. A stock solution of 50 nM antibody + 2 mM $K_4Fe(CN)_6$ solution was prepared and stored at 4°C. The 2.5 nM antibody measurement was performed by recording the $Fe(CN)_6^{4-}$ oxidation while adding a 2 µL drop of the Ab stock solution into a 40 µL drop of 2 mM $Fe(CN)_6^{4-}$ already in contact with the cantilever platform and the SECM tip. The 25 nM experiments were performed by the direct deposition of a 40 µL drop of required solution between the substrate and tip. Ag-Ab dissociation was achieved after successive rinsings of the substrate/tip assembly previously exposed to the Ab solution with 4x40 µL of MilliQ water, then with 2x40 µL of $Fe(CN)_6^{4-}$ solution, followed by removal of the latter and deposition of a 40 µL of a 0.1 M glycine + 2 mM $K_4Fe(CN)_6$ solution.

2.5. Simulations. Simulated approach curves above the cantilever free end were obtained by the finite elements method with COMSOL 3.4 package. The simulations were computed in 3D geometry for different tip positions above the substrate and different finite electron transfer kinetics at the substrate corresponding to the experimental situations.

The simulation consisted, as described elsewhere [33, 34], of the numerical solution of the diffusion equation under the appropriate boundary conditions and electrode position. The probe current was evaluated using a weak constraint procedure. To generate SECM approach curves, a steady-state simulation was obtained for a given probe-substrate distance, d. L=d/a is the dimensionless probe-substrate distance, it is taken as L = 20 (infinite distance) at the beginning of the simulation. This simulation procedure was repeated from a simple MATLAB routine, which iteratively decreases L down to 0.01. The optimized 3D modeling conditions (meshing) were obtained for the tip held above the plain substrate; they correspond to tip responses that reproduce the standard 2D axisymmetric responses. These conditions were used for the simulation of the tip response above the whole cantilever platform.

3. RESULTS AND DISCUSSION

3.1. Electrochemical Inspection of Conducting and Coated Cantilever Platforms. As sketched in Figure 5.1 c, the SECM was used to address and image the electrochemical reactivity of both types (conductive and insulating) of cantilever platforms held in a solution of a redox probe (2 mM $Ru(NH_3)_6^{3+}$ in 0.1 M KBr) with a 12.5 µm radius Pt electrode (RG = 7) used as the tip. The SECM also allows positioning the tip above either i) the plain substrate or ii) the free end of one cantilever standing over a carved pool (Fig. 5.1). These SECM procedures were achieved in the feedback mode by reducing $Ru(NH_3)_6^{3+}$ at the tip. The SECM approach curves of the unbiased plain, $CANT_{cond}$, and grafted, $CANT_{ins}$, substrates are presented in Figure 5.2 as red and black curves respectively. The experimental (open symbols) curves are compared to theoretical ones (lines). The $CANT_{cond}$ substrate

behaves as a conducting surface as its SECM approach curve shows a positive feedback response, while $CANT_{ins}$ presents a negative feedback (lowest curve in Fig. 5.2).

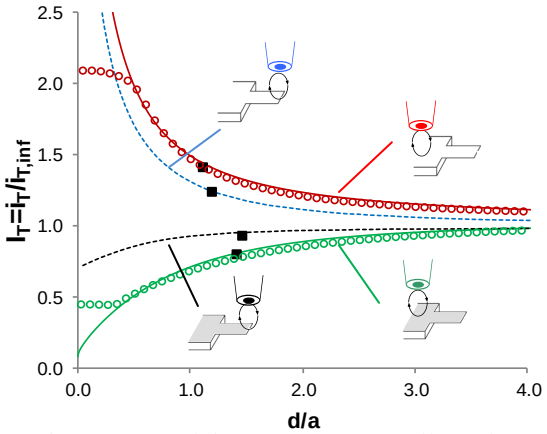

Figure 5.2 SECM approach curves with a 12.5 µm radius tip of unbiased bare cantilever substrate CANTcond (red, **o**: experimental curve; line: theory) and grafted cantilever substrate covered with nitrophenyl film, CANTins, (green, **o**: experimental curve; line: theory); redox probe: 2 mM $Ru(NH3)_6^{3+}$ in 0.1 M KBr, E_{tip} = - 0.3 V vs Ag/AgCl. Dashed lines: theoretical approach curves of the cantilever free end (same reactivity as the plain substrate, bare: dashed blue, grafted: dashed black); ■ : currents measured above plain substrate and cantilever free end during SECM images capture in **Figure 5.3**

This shows that the conducting behavior of Au is partially blocked by the presence of the organic layer. However, the layer is not completely blocking and allows some charge transfer occurring at an heterogeneous rate constant, $k_{app,ins}$ = 3.4 x 10^{-4} cm/s, estimated from fitting to theory. Conversely, the electron transfer (ET) rate for the same reaction of the tip electrogenerated $Ru(NH_3)_6^{2+}$ at the $CANT_{cond}$ substrate is $k_{app,cond}$ > 0.02 cm/s.

3.2. SECM Imaging of Cantilever Platforms. The contrast in the electrochemical reactivity of both substrates is further confirmed by SECM imaging of a 70 µm long and 20 µm wide microcantilever by a SECM tip rastered at a constant 13 µm distance above the same pristine and grafted substrates.

Figure 5.3 a, b presents the SECM image of a bare Au cantilever, $CANT_{cond}$. The currents recorded at the lowest corners of the image are representative of the infinite distance current, $|i_{T,,inf}|$, as the tip is held above the deep reservoir of solution; the substrate and cantilever are then detected as regions of tip current, $|i_T|$, higher than $|i_{T,inf}|$.

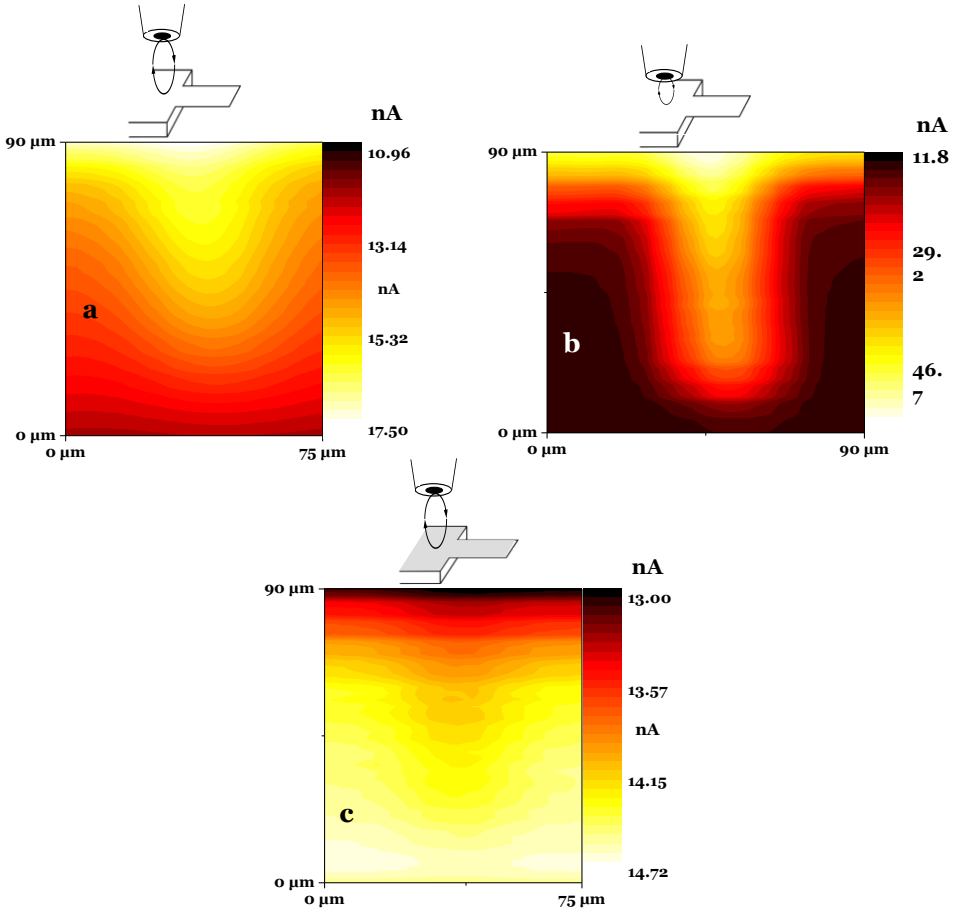

Figure 5.3 SECM feedback images acquired with a 12.5 µm radius Pt UME in a 2 mM $Ru(NH_3)_6^{3+}$ + 0.1 M KBr solution at constant height d (measured above the plain substrate) of (a, b) a bare Au cantilever $CANT_{cond}$ with d = 13.5 and 1.5 µm respectively, (c) a nitrophenyl grafted cantilever, $CANT_{ins}$, d=16.5µm. d measured above the plain substrate. E_{tip}= -0.3 V vs Ag/AgCl. Tip currents are presented in their absolute values (for $Ru(NH3)_6^{3+}$ reduction, a negative cathodic current is detected experimentally)

The tip current at the cantilever edge is lower than that above the substrate due to a lesser contribution in the regeneration process from the small microcantilever object. Conversely, Figure 5.3 c presents the image of the coated $CANT_{ins}$.

Then, the substrate and cantilever are detected as regions of tip current, $|i_T|$, lower than $|i_{T,inf}|$, as a result of diffusion hindrance by the partly blocking substrate. The tip current at the cantilever edge is higher than that above the substrate, due to lesser diffusion hindrance by the small object in regard to the tip.

The 3D modeling of the SECM tip current – distance curve (approach curve) above the free end of a cantilever for both platforms is presented as dashed lines, in Figure 5.2, using the electrochemical reactivities, k_{app}, estimated on the plain substrates (see above). Such modeling confirms that the cantilever is described by less contrasted current than the plain substrate. It also shows that the tip current values recorded at the cantilever end correspond to slightly higher tip-substrate separation distances, indicating that the cantilever is tilted down (by < 1 μm). Finally, it suggests that images with higher contrast are obtained when decreasing the tip-substrate separation distance, as observed experimentally in Figure 5.3 b for $CANT_{cond}$ imaged at a constant 1.5 μm height.

3.3. SECM Sensing of Mechanical/Chemical Transformation at Microcantilever. The SECM tip was used as a local sensor of mechanical and/or (electro-)chemical changes in microcantilever platforms. The SECM tip positioned either over one cantilever free end or over the plain substrate is then used as an amperometric sensor of the local substrate activity. The same electrolytic solution is used, the tip is now immobile at a close distance, d, from the substrate and biased at a constant potential E_T = -0.3 V vs Ag/AgCl for mass-transfer limited reduction of $Ru(NH_3)_6^{3+}$. Meanwhile, the substrate potential, E_S, is scanned at 10 mV/s toward anodic potentials (0.1 < E_S < 0.6 V vs Ag/AgCl). Under these conditions, the substrate does not allow the transformation of the $Ru(NH_3)_6^{3+}$ redox probe present in solution but may regenerate it from its reduced form ($Ru(NH_3)_6^{2+}$) generated at the tip (Fig.

5.1 c). The variations of the feedback current collected at the immobile tip for this regeneration at the substrate during the variations of E_S are presented in Figure 5.4. The tip position was fixed at, respectively, 3 and 5 µm height over the $CANT_{cond}$ (Fig 5.4 a) and $CANT_{ins}$ (Fig. 5.4 c) substrates. The tip current is recorded simultaneously with the substrate response (dashed line in Fig. 5.4 a), whether the tip is positioned over the substrate (red line) or over a cantilever free end (blue line); it allows the description of the tip/substrate coupling in the (TG/SC) feedback mode of the SECM.

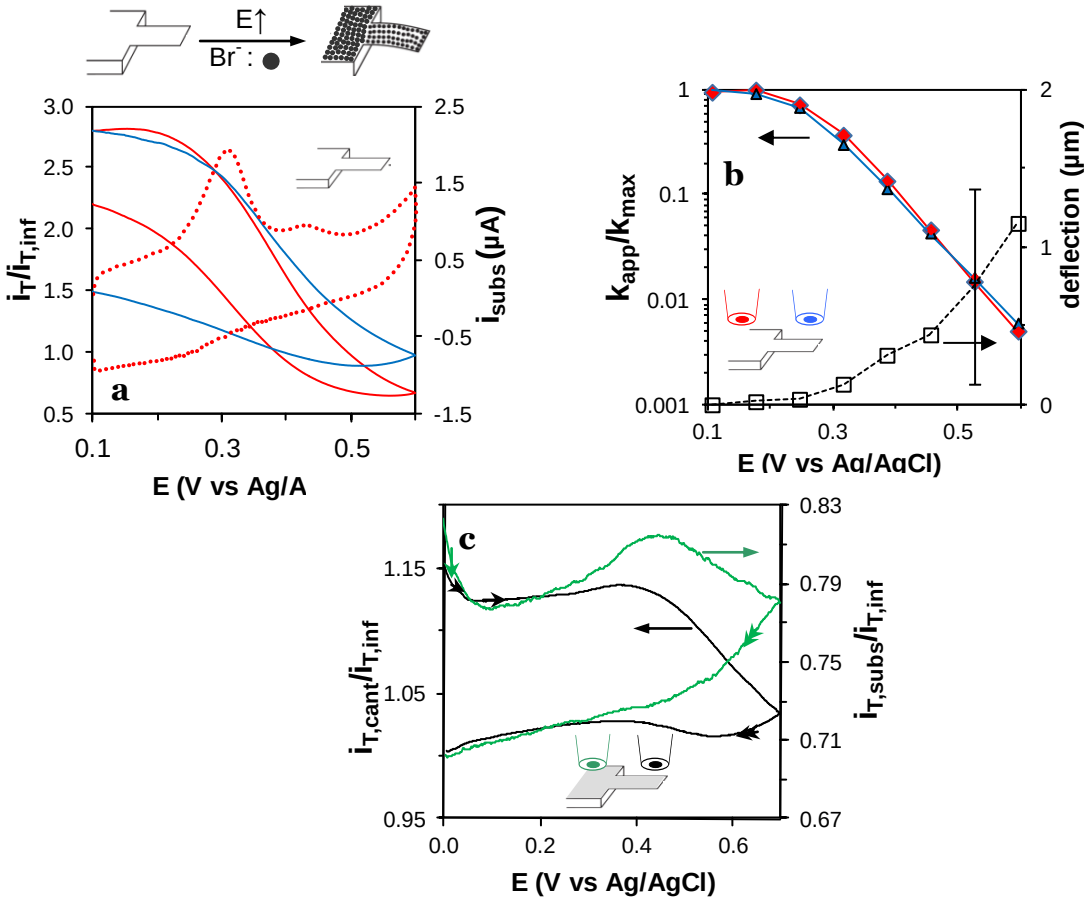

Figure 5.4 Tip current, i_T, responses normalized to current at infinite distance, $i_{T,inf}$ in an aqueous 2 mM $Ru(NH3)_6^{3+}$ + 0.1 M KBr solution. Currents measured before (**a**) and after (**c**) grafting (respectively $CANT_{cond}$ and $CANT_{ins}$) above plain substrate (red in **a**, green in **c**) or cantilever free end (blue in **a**, black in **c**) assorted with substrate response for $CANT_{cond}$ (i_{subs} for a 0.36 cm^2 substrate, dashed red in **a**). (**b**) ET rate for redox probe regeneration at the substrate estimated from tip current response above (◆) plain substrate or (▲) cantilever free end ; deflection (□) estimated from tip response, assuming the cantilever reactivity is the same as that of the substrate (◆)

We have tested the methodology in the case of an electrochemically-assisted adsorption on the substrate since this situation mimics what is encountered in chemosensor microcantilever platforms. The adsorption of Br^- was chosen to be tested as it has been extensively characterized [35-38] and should be compatible with independent SECM interrogation without excessive Au dissolution. Figure 5.4 a illustrates the cyclic voltammetric response of the $CANT_{cond}$ substrate in 0.1 M KBr.

It presents a main peak at 0.29 V vs Ag/AgCl assigned to the oxidative adsorption of Br^- on Au. It is followed by a smaller peak at 0.45 V representative of the Br adlayer reconstruction [36] and then by the onset of Br_2 formation and/or Au dissolution. Reports by Lipkowski's group [35-37, 39] depict the Br^- adsorption process as a potential dependent coverage of the Au surface with Br. This process starts at the peak onset until a closely-packed monolayer is attained at anodic potentials (E > 0.5 V vs Ag/AgCl) [35, 39]. The process, depicted by (1), yields to the formation of a chemisorption bond with partial covalent character between the adsorbed Br^- and the metal surface, as evidenced by thermodynamic analysis of charge density data [35-37], second harmonic generation spectroscopy[35] and X-ray diffraction studies [38]:

$$Br^- - e^- \rightarrow Au{-}Br \qquad (1)$$

During this process, the Br surface coverage is proportional to the electrode surface charge density. The integration of the forward CV scan indicates that on $CANT_{cond}$, the Br^-adsorption is associated to a flow toward $CANT_{cond}$ of a positive charge of 90 $\mu C/cm^2$, a value in agreement with full electrode coverage.

This oxidative process associated to Br adsorption is recorded simultaneously by the interrogating SECM tip. At potentials more positive than the onset of the electrochemical substrate transformation, the tip current decreases, indicating a decrease of the $Ru(NH_3)_6^{3+}$ regeneration at the Au surface during its coverage by the

Br layer. The extent of the Au coverage on the ET properties may be seen on the forward and backward potential scan, from both local SECM observation above the plain substrate and the cantilever end. However, a hysteresis is observed and the original surface is not totally recovered (desorption not completed) at the end of the cyclic voltammetry. Desorption is completed during longer polarization times or polarization at more cathodic potentials, but is difficult to quantify in the presence of $Ru(NH_3)_6^{3+}$ in the solution. Then, only the forward potential scan is used to analyze the local potential dependency of the adsorption process. This is obtained through the estimate of the local electron transfer rate from the substrate to the tip-generated $Ru(NH_3)_6^{2+}$. The ET rate constant, k_{app} in cm s^{-1}, is obtained from available theoretical analytical expressions relating the tip current to finite ET kinetics at the plain substrate [40], or, for the cantilever free end, from 3D modeling. For both locations, k_{app} values, normalized by their maximal value, k_{max}, are plotted in Figure 5.4 b. They decrease exponentially with the substrate potential with a Tafel coefficient of the order of $\alpha = RTd\ln k_{app}/FdE$ = 0.39 and 0.33, respectively for the plain substrate and the cantilever end. This shows that the Br surface coverage alters the ET kinetics. Moreover, this electrochemically-induced deposition on the cantilever should induce a stress accompanied by the cantilever deflection and therefore by a change in the tip-cantilever separation distance. Indeed, the Br adsorption has a compressive effect on Au(111), associated to a decrease of the interfacial energy of 0.85 N/m/V, estimated from electrocapillary curves[37]. The extrapolation of these electrocapillary data obtained in a diluted KBr solution yields a considerable compressive surface stress of $\Delta\gamma \sim -0.5$ N/m for the Br adsorption at E = 0.6 V on Au(111). This suggests an important deflection of the cantilever that may be appreciated by a new interpretation of the $k_{app} = f(E)$ relationship observed at the

cantilever end. Assuming that the electrochemical activity, $k_{app} = f(E)$, of the cantilever follows that of the substrate, the smoother potential variations of the tip current above the cantilever end can be interpreted as a variation of the tip-cantilever separation distance, Δd in Figure 5.1 c.

Qualitatively, the variation of the tip-cantilever separation distance can be discussed from a general inspection of approach curves (variations of I_T with d/a). Reactive substrates are characterized by positive feedback behaviors ($I_T > 1.2$) and a decrease of the tip current is associated with an increase of the tip-substrate separation distance d/a. Conversely, at low substrate reactivity, negative feedback is observed ($I_T < 1$) and an increase of d/a is associated with an increase of the tip current. Finally, in a limited range of $k_{app} \sim D/a$ (D is the diffusion coefficient of the redox probe), the approach curve is almost independent of d/a and $I_T \sim 1$; therefore, no information may be obtained on the tip-substrate separation distance.

These three distinct behaviors qualitatively fit with the potential-dependent behaviors observed experimentally in Figure 5.4 a, b. For $0.3 < E < 0.5$ V, the reactivity of the substrate is high ($I_T > 1.3$ in Fig. 5.4 a), and the cantilever response shows lower k_{app}/k_{max} values than the plain substrate, indicating a larger d above the cantilever than above the plain substrate (downward cantilever deflection). For $E > 0.52$ V, the substrate reactivity is in the negative feedback region ($I_T < 1$ for the plain substrate in Fig. 5.4 a) and k_{app}/k_{max} is higher on the cantilever than on the plain substrate, also indicating a larger d above the cantilever (downward deflection). The identical reactivity and $I_T \sim 1$ correspond to the region with no distance effect and no information can be obtained on the cantilever deflection.

A quantitative description of the cantilever deflection (□ in Fig. 5.4 b) is obtained from 3D modeling, knowing the experimental tip current values (provided in Fig. 5.4

a) and the k_{app} extrapolated from the plain substrate values (◆ in Fig. 5.4 b). It confirms that the cantilever bends down during the positive charge accumulation and Br adsorption, in agreement with a compressive surface stress. The electrochemically-induced electrode coverage induces a bending of the cantilever by ~ 1.2 µm at E = 0.6V while sub-micrometric deflections can be detected at lower potentials. The values of the deflection may vary by less than 20% because of uncertainties on the position (x,y,z) of the tip above the cantilever end. The approximate µm deflection is supported by the mechanical properties of the microcantilever. Indeed, it is typically the magnitude of deflection detected by independent interferometric measurement in air upon a 10°C temperature change.

The response of the $CANT_{ins}$ platform is then addressed in Figure 5.4 c when it is covered by a thin diazonium-derived organic layer. First, the substrate coated with the organic layer does not present any more the adsorptive feature related to Br adsorption. Moreover, the tip response shows contrasted behavior, depending on its location above the platform. Above the plain substrate, the regeneration process at the substrate slightly increases with the substrate potential, then it decreases as E > 0.5 V. However, along the whole potential range, $k_{app,subs}$ = 5.3 ± 0.6 x 10^{-4} cm s^{-1}. On the contrary, the tip response above the cantilever free end is also constant for E < 0.47 V, but decreases down by 20% as E > 0.5 V.

This contrasted reactivity qualitatively suggests the mechanical contribution of the cantilever. For E < 0.47 V, the ET rate at the cantilever free end corresponds to $k_{app,lev}$ = 2.3 x 10^{-3} cm s^{-1}, an activity four times higher than on the plain substrate. Such heterogeneity of surface reactivity at the grafted platform indicates that the cantilever region has been less efficiently covered by the aryl layer than the plain substrate. It is then difficult to deconvolute properly from the tip responses, obtained at a single tip

height, the contributions of reactivity and cantilever deflection. However, assuming the cantilever is not significantly deflected during the cyclic voltammetry, the decrease of the reactivity for E > 0.5 V likely also corresponds to Br adsorption. On the organic-coated cantilever, it is retarded by an ~ 0.35 V overpotential as the organic layer is an efficient barrier to inner-sphere charge transfer [41].

3.4. SECM sensing of receptor-ligand reaction. Once the potentiality of the SECM sensing of cantilever activity has been demonstrated on electrochemically actuated systems, it was tested for heterogeneous immunoassays. We have followed the same electrochemical approach to describe the formation of an immune complex at a microcantilever platform surface. Here, the SECM tip is used to follow, in the feedback mode, a model immunological reaction occurring heterogeneously between the cantilever platform, $CANT_{Ag}$, on which an antigen (Ag: α-lactalbumin) has been immobilized and its corresponding antibody (Ab) present in the solution. The Ag-Ab interaction is probed upon Ab injection from the current variations detected at the tip for the oxidation of a redox probe (2 mM $Fe(CN)_6^{4-}$ in PBS), with the tip held at 5-6 μm from the $CANT_{Ag}$ surface.

Except from the initial current transients spikes due to solution injection, the Ab adsorption on the plain substrate (Fig. 5.5 a, green lines) results in a decrease of the tip response. The current decrease indicates that upon the Ag-Ab complex formation, the ET from the Au surface to the redox probe is attenuated. Here, it results from the ET attenuation upon the surface immobilization associated to the coverage of the $CANT_{Ag}$ platform surface with a more compact biomolecular layer. This is corroborated by the current increase detected upon desorption of the Ab during glycine injection (not shown), which causes the dissociation of the immune complex from the surface.

These observations are in line with the decrease of the efficiency of cycling of redox probes detected during the specific capture of biochemical targets [28, 42-45].

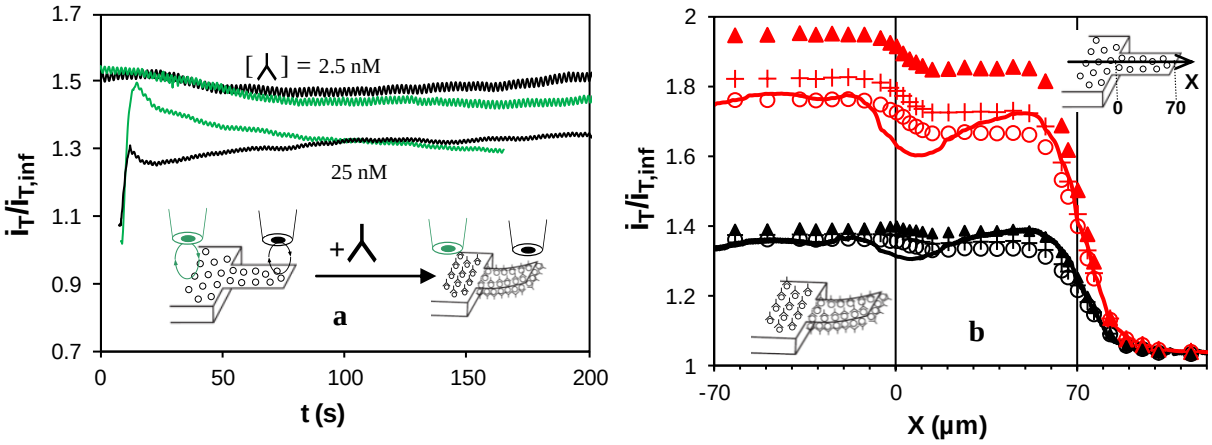

Figure 5.5 Interaction of Ab with Ag (α-lac) immobilized on an Au microcantilever platform, $CANT_{Ag}$. (a) Transient tip responses recorded during Ab adsorption on the $CANT_{Ag}$ platform, d = 5 µm, above (green) plain substrate or (black) cantilever free end; injection t = 10 s of 2.5 or 25 nM of Ab; (b) Experimental (lines) and theoretical (symbols) linescans tip response while rastered above, X < 0, the plain substrate and, 0 < X < 70 µm, the cantilever free end, after (black) Ab adsorption followed by (red) Ab desorption in the presence of glycine; theoretical responses for tip-object separation distances from top to bottom d = 4, 4.9, 5.6 µm; red symbols: $k_{app,Ag}$ = 0.02, black symbols: $k_{app,AgAb}$ = 0.008 cm/s. redox probe: 2 mM $Fe(CN)_6^{4-}$ in PBS. E_{tip} = 0.4 V vs Ag/AgCl, substrate unbiased.

A similar indirect electrochemical strategy for label-free detection of biochemical capture has been originally proposed for DNA hybridization [42, 43] and applied more recently for Ab detection, either through Ag-Ab interaction at screen-printed electrodes[44] or for the detection of coumarin-antibody on a coumarin-derivatized microelectrode in molecular addressable libraries[45]. Figure 5.5 a also suggests that the sensitivity of such electrochemical method based on ET attenuation upon Ag-Ab association is ~ nM, a value ~10 times higher than that attained for α-lac in a magnetic nanoparticles-based immunoassay[46] or in surface plasmon resonance biosensing[47].

Conversely, above the cantilever free end (Fig. 5.5 a, black lines), the Ab immobilization is associated to a first current decrease followed by a current increase, in favor of both ET attenuation and tip-cantilever distance change. Such opposite current variations then indicate that during the Ab association, the cantilever is approaching the tip.

The upward (or downward) deflection associated to the biomolecular adsorption (or desorption) on the cantilever is also confirmed from linescans of the tip current recorded while it is rastered at 5 µm/s along the cantilever symmetry axis after the adsorption and desorption processes (Fig. 5.5 b). It can be seen from Figure 5.5 b that the substrate response ($x < 0$), or the cantilever one ($0 < x < 70$ µm) is heterogeneous and varies locally by ~15%. However, the value of the tip current above the end of the cantilever ($X \sim 70$ µm) is slightly lower (by ~5%) than that recorded above the substrate when the Ab has been adsorbed (black line in Fig. 5.5 b). Conversely, after desorption of the immune complex, the linescan recorded in a solution of the redox probe in the presence of 0.1 M glycine (red line in Fig. 5.5 b), the tip response above the cantilever end is lower by 20% compared to that on the substrate. Within the condition of positive feedback ($I_T > 1.2$), such difference qualitatively indicates the relative downward deflection of the cantilever associated to the desorption process. These linescans can be compared to theoretical tip responses obtained from 3D modeling. They are presented in Figure 5.5 b as symbols for respectively tip-object separation distances d = 4, 4.9 and 5.6 µm and for apparent ET rate constants, $k_{app,Ag}$ and $k_{app,AgAb}$ = 0.02 and 0.008 cm/s respectively. If a good fit is observed above the plain substrate with the same d = 5.6 µm (circles) before or after Ag-Ab formation, above the cantilever end ($50 < x < 70$ µm), the best fit is obtained for d = 4.9 µm or d

= 4 µm respectively. This difference indicates that the Ag-Ab interaction is associated with a 0.9 µm upward deflection of the cantilever free end.

Even though the magnitude of the deflection is comparable, the upward deflection during Ab adsorption is at odd with the downward deflection observed during Br adsorption. However, both systems may behave differently. Indeed, the Br adsorption is actuated electrochemically and then only occurs on the gold coated face of the cantilever, while the Ab adsorption may occur on both faces of the cantilever. The upward deflection of the cantilever during Ab immobilization then indicates that the upper gold side of the cantilever is less coated by Ag than the lower silica side. It is not surprising, owing to the Ag immobilization procedure on the Au surface: the seeding of the Au surface with the -COOH anchoring group was obtained by diazonium electrografting and the resulting layer does not completely cover the Au surface as it still shows positive SECM feedback ($I_T > 1.3$).

4. CONCLUSION

The deflection of cantilever systems may be addressed by an indirect electrochemical method such as redox cycling between a SECM tip and a microcantilever. Such alternative to the classical optical detection consists of measuring the local cantilever activity and deflection in a feedback generation-collection configuration of the SECM. This is illustrated in different sensing systems. We first use the electrode nature of the cantilever platform to induce the electrochemically-assisted adsorption of Br on an Au cantilever, either in its pristine state or previously coated with a thin organic barrier. The Br adsorption is accompanied by the attenuation of the ET to a redox probe and is associated to the

measurable bending of the cantilever. When a thin organic layer coats the Au surface, because of the heterogeneity of the coating layer on the whole platform, the deflection cannot be extracted from the SECM measurements, even though contrasted behaviors qualitatively suggest a mechanical effect at the cantilever. Then, a microcantilever platform is used to sense an immunological reaction between a surface immobilized antigen and its solubilized antibody. The Ab-Ag interaction is associated with a feedback decrease due to the ET attenuation during the recognition event associated to the coverage of the electrode surface by a passivating biomolecular layer. It is also associated to a deflection of the cantilever detected by a local tip current measurement.

The resolution of the electrochemical technique cannot be compared yet to the standard optical one, but some advantages of this approach may be pointed out. First of all, the simplicity of the setup and the possibility of simultaneously measuring the cantilever deflection and characterizing the surface reactivity by SECM can be mentioned. Although the optical detection of cantilever mechanical movements is the most sensitive detection technique, some limitations have been expressed. Indeed, the optical technique is not suited for samples absorbing or scattering light, and also for fluids with suspended particles. The proposed electrochemical technique can overcome some of these limitations, by allowing electrochemical characterization of non-conductive cantilevers and appropriate use for closed systems, where the optical detection is not possible. Moreover, it is obvious that the resolution for the detection of the cantilever mechanical displacement depends on the tip radius. Then, owing to the current possibilities to fabricate sub-micrometric UMEs, imaging resolution down to the nanometer scale is expected.

Funding Sources

The “Agence Nationale de la Recherche”, ANR, is gratefully acknowledged for its financial support via the ANR-08-JCJC-0088 µECOLIERS project.

References

1. Binnig, G., C.F. Quate, and C. Gerber, *Atomic Force Microscope*. Physical Review Letters, 1986. **56**(9): p. 930-933.
2. Hansen, K.M. and T. Thundat, *Microcantilever biosensors*. Methods, 2005. **37**(1): p. 57-64.
3. Goeders, K.M., J.S. Colton, and L.A. Bottomley, *Microcantilevers: Sensing chemical interactions via mechanical motion*. Chemical Reviews, 2008. **108**(2): p. 522-542.
4. Raiteri, R., et al., *Micromechanical cantilever-based biosensors*. Sensors and Actuators B-Chemical, 2001. **79**(2-3): p. 115-126.
5. Wu, G.H., et al., *Bioassay of prostate-specific antigen (PSA) using microcantilevers*. Nature Biotechnology, 2001. **19**(9): p. 856-860.
6. Bache, M., et al., *Investigations on antibody binding to a microcantilever coated with a BAM pesticide residue*. Nanoscale Research Letters, 2011. **6**.
7. Zheng, S., et al., *Analysis of DNA hybridization regarding the conformation of molecular layer with piezoelectric microcantilevers*. Lab on a Chip, 2011. **11**(1): p. 63-69.
8. Eom, K., et al., *Nanomechanical actuation driven by light-induced DNA fuel*. Chemical Communications, 2012. **48**(7): p. 955-957.
9. Bange, A.F., et al., *Stripping voltammetry of Pb and Cu using a microcantilever electrode*. Surface Science, 2009. **603**(21): p. L125-L127.
10. Chen, X., et al., *Application of displacement principle for detecting heavy metal ions and EDTA using microcantilevers*. Sensors and Actuators B-Chemical, 2012. **161**(1): p. 203-208.
11. Godin, M., et al., *Cantilever-based sensing: the origin of surface stress and optimization strategies*. Nanotechnology, 2010. **21**(7).
12. Tian, F., et al., *Observation of the surface stress induced in microcantilevers by electrochemical redox processes*. Ultramicroscopy, 2004. **100**(3-4): p. 217-223.
13. Chapman, P.J., et al., *Differentially ligand-functionalized microcantilever Arrays for metal ion identification and sensing*. Analytical Chemistry, 2007. **79**(18): p. 7062-7068.
14. Norman, L.L. and A. Badia, *Redox Actuation of a Microcantilever Driven by a Self-Assembled Ferrocenylundecanethiolate Monolayer: An Investigation of the Origin of the Micromechanical Motion and Surface Stress*. Journal of the American Chemical Society, 2009. **131**(6): p. 2328-2337.
15. Tabard-Cossa, V., et al., *Microcantilever-based sensors: Effect of morphology, adhesion, and cleanliness of the sensing surface on surface stress*. Analytical Chemistry, 2007. **79**(21): p. 8136-8143.
16. Amiot, F., et al., *Charge redistribution in electrochemically actuated mechanical sensors*. Sensors and Actuators a-Physical, 2009. **152**(1): p. 88-95.
17. Garraud, N., et al., *Multiple wavelength reflectance microscopy to study the multiphysical behavior of microelectromechanical systems*. Optics Letters, 2011. **36**(4): p. 594-596.
18. Juluri, B.K., et al., *A Mechanical Actuator Driven Electrochemically by Artificial Molecular Muscles*. Acs Nano, 2009. **3**(2): p. 291-300.
19. Dohn, S., et al., *The influence of refractive index change and initial bending of cantilevers on the optical lever readout method*. Review of Scientific Instruments, 2010. **81**(6).
20. Huber, F., et al., *Analyzing refractive index changes and differential bending in microcantilever arrays*. Review of Scientific Instruments, 2008. **79**(8).
21. Barnes, E.O., et al., *Generator-collector double electrode systems: A review*. Analyst, 2012. **137**(5): p. 1068-1081.

22. Wittstock, G., et al., *Scanning electrochemical microscopy for direct imaging of reaction rates*. Angewandte Chemie-International Edition, 2007. **46**(10): p. 1584-1617.
23. Amemiya, S., et al., *Scanning Electrochemical Microscopy*. Annual Review of Analytical Chemistry, 2008. **1**: p. 95-131.
24. Rodriguez-Lopez, J., M.A. Alpuche-Aviles, and A.J. Bard, *Interrogation of Surfaces for the Quantification of Adsorbed Species on Electrodes: Oxygen on Gold and Platinum in Neutral Media*. Journal of the American Chemical Society, 2008. **130**(50): p. 16985-16995.
25. Rodriguez-Lopez, J. and A.J. Bard, *Scanning Electrochemical Microscopy: Surface Interrogation of Adsorbed Hydrogen and the Open Circuit Catalytic Decomposition of Formic Acid at Platinum*. Journal of the American Chemical Society, 2010. **132**(14): p. 5121-5129.
26. Amatore, C., et al., *Theory and Experiments of Transport at Channel Microband Electrodes under Laminar Flows. 2. Electrochemical Regimes at Double Microband Assemblies under Steady State*. Analytical Chemistry, 2008. **80**(24): p. 9483-9490.
27. Zevenbergen, M.A.G., et al., *Electrochemical Correlation Spectroscopy in Nanofluidic Cavities*. Analytical Chemistry, 2009. **81**(19): p. 8203-8212.
28. Singh, P.S., et al., *Stochastic Amperometric Fluctuations as a Probe for Dynamic Adsorption in Nanofluidic Electrochemical Systems*. Journal of the American Chemical Society, 2011. **133**(45): p. 18289-18295.
29. Macpherson, J.V. and P.R. Unwin, *Combined scanning electrochemical-atomic force microscopy*. Analytical Chemistry, 2000. **72**(2): p. 276-285.
30. Kueng, A., et al., *Combined scanning electrochemical atomic force microscopy for tapping mode imaging*. Applied Physics Letters, 2003. **82**(10): p. 1592-1594.
31. Fasching, R.J., Y. Tao, and F.B. Prinz, *Cantilever tip probe arrays for simultaneous SECM and AFM analysis*. Sensors and Actuators B-Chemical, 2005. **108**(1-2): p. 964-972.
32. Belanger, D. and J. Pinson, *Electrografting: a powerful method for surface modification*. Chemical Society Reviews, 2011. **40**(7): p. 3995-4048.
33. Combellas, C., et al., *Scanning electrochemical microscopy. Hydrodynamics generated by the motion of a scanning tip and its consequences on the tip current*. Analytical Chemistry, 2005. **77**(24): p. 7966-7975.
34. Cornut, R., et al., *Accurate and Simplified Consideration of the Probe Geometrical Defaults in Scanning Electrochemical Microscopy: Theoretical and Experimental Investigations*. Analytical Chemistry, 2011. **83**(24): p. 9669-9675.
35. Shi, Z.C., et al., *Electrochemical and second harmonic generation study of bromide adsorption at the Au(111) electrode surface*. Journal of the Chemical Society-Faraday Transactions, 1996. **92**(20): p. 3737-3746.
36. Ocko, B.M., et al., *A Critical Comparison of Electrochemical and Surface X-Ray-Scattering Results at the Au(111) Electrode in Kbr Solutions*. Journal of Electroanalytical Chemistry, 1994. **376**(1-2): p. 35-39.
37. Shi, Z. and J. Lipkowski, *Investigations of So42- Adsorption at the Au(111) Electrode in the Presence of Underpotentially Deposited Copper Adatoms*. Journal of Electroanalytical Chemistry, 1994. **364**(1-2): p. 289-294.
38. Magnussen, O.M., et al., *X-Ray-Diffraction Studies of Ordered Chloride and Bromide Monolayers at the Au(111)-Solution Interface*. Physical Review B, 1995. **51**(8): p. 5510-5513.
39. Chen, A.C., et al., *Iodide adsorption at the Au(111) electrode surface*. Journal of Electroanalytical Chemistry, 1999. **467**(1-2): p. 342-353.
40. Cornut, R. and C. Lefrou, *New analytical approximation of feedback approach curves with a microdisk SECM tip and irreversible kinetic reaction at the substrate*. Journal of Electroanalytical Chemistry, 2008. **621**(2): p. 178-184.

41. McCreery, R.L., *Advanced carbon electrode materials for molecular electrochemistry*. Chemical Reviews, 2008. **108**(7): p. 2646-2687.
42. Turcu, F., et al., *Imaging immobilised ssDNA and detecting DNA hybridisation by means of the repelling mode of scanning electrochemical microscopy (SECM)*. Biosensors & Bioelectronics, 2004. **20**(5): p. 925-932.
43. Zhu, X., et al., *Amperometric detection of DNA hybridization using a multi-point, addressable electrochemical device*. Sensors and Actuators B-Chemical, 2011. **160**(1): p. 923-928.
44. Holmes, J.L., et al., *A new application of scanning electrochemical microscopy for the label-free interrogation of antibody-antigen interactions*. Analytica Chimica Acta, 2011. **689**(2): p. 206-211.
45. Tesfu, E., et al., *Buillding addressable libraries: Site selective coumarin synthesis and the "Real-Time" signaling of antiibody-coumarin binding*. Organic Letters, 2006. **8**(4): p. 709-712.
46. Teste, B., et al., *Kinetic analyses and performance of a colloidal magnetic nanoparticle based immunoassay dedicated to allergy diagnosis*. Analytical and Bioanalytical Chemistry, 2011. **400**(10): p. 3395-3407.
47. Indyk, H.E., *Development and application of an optical biosensor immunoassay for alpha-lactalbumin in bovine milk*. International Dairy Journal, 2009. **19**(1): p. 36-42.

General conclusions and perspectives

In the course of the work presented in this thesis, I have been interested in the development of new analytical methods combining electrochemical and optical inspection of surface processes. I have investigated and characterized the *in situ* and real-time local electrochemical and chemical reactivities of different surfaces. For this purpose, I have set up two experimental devices for coupling imaging optical microscopy with electrochemical activation methods. In particular, I have examined the possibility of coupling electrochemical techniques to visible light reflectivity microscopy and to ellipsometric microscopy. I have validated these imaging techniques through the investigation of surfaces reactivities. I have specifically focused on a model system: the electrochemical grafting of thin organic films on surfaces by reduction of diazonium salts**.** I have highlighted the potential of these two optical imaging techniques on a wide variety of gold electrode surfaces.

The light reflectivity microscope has been used to depict *in situ* and in real time the efficiency of the electrografting of different diazonium salts onto gold surfaces. The yield of the coating reactions obtained with our setup is comparable with that obtained using other techniques such as QCM, validating our approach. We have then used our opto-electrochemical microscope to analyze the coating kinetics at different substrates and under different electrogenerated flux regimes. I have evidenced the deposition of very thick layers with a thickness higher than 500 nm during the electrografting of 4-nitrobenzenediazonium under highly negative potentials. Under these conditions, a very high level of light is absorbed. If light-absorbing species are generated, as I have confirmed on ITO electrodes by UV-vis absorption spectrometry, most of the light is likely lost in the oligomeric nanostructured architecture, which is probably light diffusing, providing a coating with interesting optical properties.

The study of local (bio) chemical reactivity has also been examined *ex situ* and *in situ* on different surfaces micropatterned either by μCP (micro contact printing) or UV photolithography. Using our setup, I have investigated the reactivity of an *in situ* generated radical (Ar•) toward different species deposited on a surface. The opto-electrochemical microscope has allowed imaging the local fluxes of generated or reacting radicals. It then provides an interesting route to the inspection the chemical reactivity of various immobilized molecules towards electrogenerated radicals. So far,

it is difficult to know if the radical reacts with the pre-immobilized molecules or grows mainly in defects regions. However, a surface with mixed chemical properties (that of the pre-immobilized species and that of the radical) was obtained. Moreover, when the pre-immobilized molecules are biomolecules, this strategy allows the preparation of antifouling surfaces. Indeed, in some cases, the grown diazonium layer may block the recognition between bioactive and anti-bioactive species. It is possible in this way to prevent the formation (by bioactive species) of biofilms on surfaces.

As concerns the ellipsometric imagery technique, we were able with our developed setup, to monitor *in situ* and in real-time the ellipsometric parameter Δ with about 1 µm lateral resolution and sub-nanometer resolution in thickness. This was illustrated again in the case of the electrografting of a surface by diazonium salts and in the observation of such reactions at micropatterned surfaces. Our work shows unambiguously that microlithography alters the reactivity of surfaces and should be handled with care when surface chemistry reaction is sought. The future improvements envisaged for this setup should solve some present issues, such as the compensation of the tilt presented for measurements in liquid media, along with finding a solution to obtain absolute values for ellipsometric parameters for analyzed surfaces, increasing in this manner the reliability of the proposed setup.

These studies are encouraging and permit to consider these methods as a cheap and very simple alternative to the use of surface plasmon resonance (SPR). Therefore, one perspective concerns the extension of this method for the development of simple portable and cheap label-free immunoassays. On a reflective surface of either micrometer-size or larger (> 10 cm^2), it should be possible to image real-time interaction kinetics between biochemical reagents, one of which is grafted onto the reflecting surface. The advantage of this method is that it is not constrained by the shape of the sensor, it can be microfabricated -as cantilevers- and it can also be lithographed on different surfaces. We can anticipate its very simple use for the preparation of biosensors in heterogeneous label-free miniaturized format such as those used in microfluidics. As the immunoassay platforms presented in this thesis use Au as a reflecting surface, we have looked for cheaper reflecting surfaces with reflective properties close to that of Au. Copper is one of the promising candidates. The idea of finding cheaper substrates aims at the development of low cost immunoassay platforms. As only the imaging of the reflecting surface is necessary

during the reaction with the biological target, it could be performed with the camera technologies already present in mobile phones. At the end of this thesis, the challenge of building a simple, low-cost and portable device having biosensor properties seems more realistic.

The electrochemical detection of the mechanical displacements of microcantilevers platforms using SECM is an alternative to the optical detection. Even though the qualitative detection of the cantilever deflection was demonstrated, a quantitative description was obtained mainly from modelization of the tip current evolution with the beam deflection. This has been illustrated in the case of large (> 200nm) deflection during Br coverage of Au surface and through the antibody coverage of the cantilever. It should however be ameliorated through the study of other surface adsorbed species (as thiols or spontaneous or locally grafted nitrophenyl layers) using smaller local probes (few hundreds of nm in diameter) in order to observe cantilever movements in the 10 nm range. By modifying a cantilever with different coatings, it should be possible to detect a specific target species in mixtures, as with optical detection. To avoid the theoretical modeling, the direct comparison of the results with those obtained by optical detection should be considered.

All the results presented in this thesis confirm the advantages of coupling several techniques; it permits an easier and more efficient characterization of surface properties than when using a single technique. In particular, the coupling of optical imaging techniques with micro-electrochemical techniques appears very efficient and should be envisaged when in-situ and real-time investigation of surface processes are sought for.

Annexes

1. Light reflectivity image acquisition procedure using opto-electrochemical microscope

The proposed configuration for the light reflectivity measurements

1. CMOS camera; **2.** Light source (Halogen); **3.** Interference filter (with a spectral bandwidth of 20 nm); **4.** Microscope objective; **5.** Cell (sample holder); **6.** PC ; **7.** Motion Controller ; **8.** Potentiostat

The used microscopes objectives for in air or liquid light reflectivity measurements:

I) Air:

- **<u>Mirau 10X: Nikon CF IC Epi Plan DI Interferometry Objective</u>**
  Magnification: 10X
  Numerical aperture: NA 0.3
  Working Distance : WD (mm) 7.4

- **<u>OLYMPUS UPlanFLN10X/0.30</u>**
  Magnification: 10X
  Numerical aperture: NA 0.3
  Working Distance: WD (mm) 10

***II) Liquid Immersion Olympus objectives**:*

- **<u>UMPLFL10XW/0.30 U M Plan Fluorite</u>**
  Magnification: 10x,
  Numerical Aperture: NA 0.3
  Working Distance: WD=3.3 mm (water)

- **<u>UMPLFL20XW/0.50 U M Plan Fluorite 20x,</u>**
  Magnification: 20x
  Numerical Aperture : NA 0.5
  Working Distance: WD (mm) 3.3 (water)

- **<u>LUMPLFL40XW/0.80 Long WD U M Plan Fluorite 40x</u>**
  Magnification: 40x
  Numerical Aperture: NA 0.8
  Working Distance: WD=3.3 mm (water)

Light reflectivity measurement steps :

1. Initial positioning of the interference filter (3) at λ=490 nm using an fiber optic spectrometer;

2. A previously cleaned reflected substrate is fixed within a cell placed on the holder (5);

3. In order to reach the planarity of the analyzed sample, we are using the interference Mirau objective. The components inside this type of objective are

arranged that an interference pattern will appear if the system is focused upon the analyzed surface. If the surface is inclined, localized interference fringes will appear. The planarity of the surface is obtained when only one interference fringe is observed, by rotating the sample in x and y direction, using the motion controller (7).

4. After the surface is arranged in planar position, the light reflectivity measurements can start, by choosing the appropriated microscope objective. Depending on the needed information *ex-situ* and *in-situ* measurements are realized.

Ex-situ: Already modified surfaces (micropatterned, or grafted) are analyzed. The confirmation of the surface modification is obtained by analyzing the recorded images in air. The reflected light intensities are compared on the non-modified part of the sample, if a large surface is analyzed (for example, a non-modified band of a microarray structure) and the locally modified part. Using theoretical calculated sensitivity (0.43 % of reflected light intensity decrease / nm of deposited organic film of n_F=1.5) the local surface changes can be identified;

In-situ: The in-situ measurements are preferred for real-time monitoring of surface modification, in our case the electrografting of diazonium salts, by observing the coating of an organic layer on the reflecting surface.

5. Again, after the surface planarity check, the cell containing the surface to analyze, is filled with solution, containing the solute which will be deposited on the analyzed surface (by grafting of diazonium salts- resulting from the electrochemical activation of the surface, or by spontaneous grafting, or through physical adsorption on the surface). The immersion microscope objectives are selected for this type of experiments.

Before starting local modification, images of the reflecting light intensity of the surface initial state are acquired, which will be used as reference images *(recorded at t=0)*.

6. Next step consist of the continuous images recording of the surface reflected light intensity, at constant time *t* during a time interval (under an electrochemical activation in our case)

7. At the end, surface modification is confirmed after the analysis of recorded images, following the light intensity decrease for a region on the image containing **'n' x 'n'** pixels from the full image, if a local modification is analyzed, or comparing the light intensity on the entire image between the reference image (*recorded at t=0*) and the image recorded at the end of the modification process**.**

2. Image processing procedure

i) The image processing is realized using a Matlab algorithm. The used camera allow to record images having dimensions of 853x853 μm^2, containing 1024 x 1024 pixels for the x10 magnification in liquid;

ii) An area for example of 10 x 10 pixels is chosen on the first image (*recorded at t=0*), corresponding to the red square.

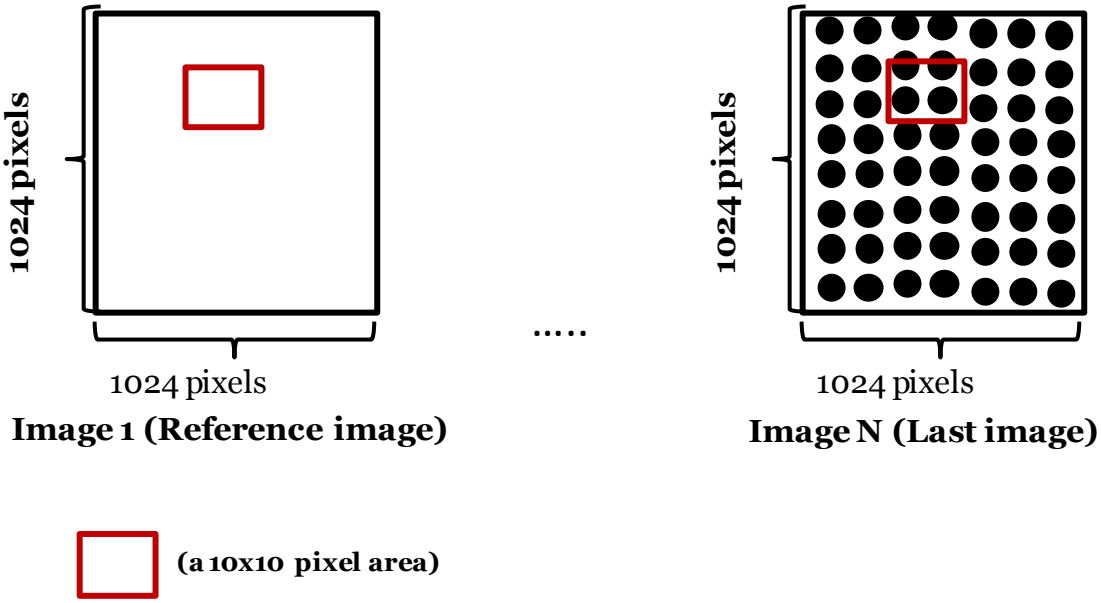

iii) The variation of mean intensity from pixels covering the red square is monitored for all recorded images (from Image 1 to Image N). In this way, the variation of light intensity is obtained for entire duration of the modification process applied to the surface;

If we are dividing the measured mean intensity in the red square during the modification process at each instant (*recorded at time t*) to the measured mean intensity in the red square from the first image (Image 1, *recorded at t=0*), we are obtaining the continuous evolution of the reflected beam light intensity in the initially chosen region (red square):

$$\textbf{Reflectivity } (1+\Delta R/R) = I_{reflected}(t)/I_{reflected}(0)$$

iv) The full field images of the evolution of the reflected beam light intensity can be obtained if the entire image recorded at instant (*t)* is divided with the image recorded at *t=0*.

In this way some defects from the analyzed surface can be erased, allowing measuring in this way small intensity variations.

3. The procedure for monitoring of antigen-antibody (Ag-Ab) interaction using optical microscope

i) Reflecting surface treatment before modification step

Gold-coated silicon wafers are ultrasonically rinsed with ethanol and acetone, dried in a stream of argon, then cleaned in a UV cleaner for 20 min, to remove the organic residues.

ii) Surface modification using diazonium salts electrografting

Electrochemical reduction of dBA – diazonium benzoic acid (**dBA**, BF_4^- , $^+N_2$- C_6H_5-COOH) was carried out in ACN solution containing 5 mM and 0.1 M $NaBu_4BF_4$, which was degassed with argon for 15 min, by cycling between +0.2mV and - 0.6m V vs SCE (three cycles) at a scan rate of 100 mV/s. After the electrochemical modification, the gold electrode was rinsed by sonication in ACN, and then cleaned in ethanol and acetone. Finally, the surfaces are subsequently dried in a stream of argon.

iii) Surface activation by NHS/EDC (peptidic coupling)

The substrates Au-dBA were treated with a solution of NHS (60 mM) and EDC (30 mM) in ultra pure water for 90 min, thoroughly washed with in Milli-Q water, and then the ester functionalised slides were dried and stored under argon.

iv) The covalent immobilization of the protein

The covalent attachment of bioactive species was carried by incubation of these slides over night at 4°C with the desired species (antigen-Ag) (X mg/L in PBS). After this step, the excess of non immobilized species was removed by three repeated washings with PBS.

v) Surface pasivation for avoiding non-specific interactions

In order to block binding sites not occupied by bioactive species, the bioactive gold surfaces were immersed for 15min in 1-aminoethanol solution then washed with PBS and Milli-Q water. To saturate the remaining actives sites, the bioactive slides were further immersed in PVP2% Tween 20 0.1% PBS1x solutions, and after 15min were vigorously rinsed three times with PBS and Milli-Q water.

vi) The optical recognition of the Ag-Ab interaction observing using light reflectivity measurements

The last step consists in the immersion of the antigen functionalized surface in a solution of its corresponding antibody (Ab) (in PBS solution), with a simultaneous recording of reflected light intensity images for a time interval. The confirmation of the Ag-Ab interaction is again obtained by reflected beam intensity comparison between the recorded image at t=0 and the image recorded at time *t*.